3D Printing of Sub-Micrometer Accurate Ultra-Compact Free-Form Optics

Timo Gissibl

2016

Timo Gissibl

3D Printing of Sub-Micrometer Accurate Ultra-Compact Free-Form Optics

An application of femtosecond three-dimensional dip-in laser lithography

3D PRINTING OF SUB-MICROMETER ACCURATE ULTRA-COMPACT FREE-FORM OPTICS

Von der Fakultät Mathematik und Physik der Universität Stuttgart
zur Erlangung der Würde eines Doktors der
Naturwissenschaften (Dr. rer. nat.) genehmigte Abhandlung

vorgelegt von

TIMO GISSIBL

aus Stuttgart

Hauptberichter: Prof. Dr. Harald Giessen
Mitberichter: Prof. Dr. Alois M. Herkommer

Tag der mündlichen Prüfung: 16.12.2015

4. Physikalisches Institut der Universität Stuttgart
2016

ABSTRACT

Additive manufacturing enables novel and unprecedented engineering and production possibilities, which are predicted to have an enormous impact in the 21st century. The technology allows for the straightforward three-dimensional printing of volumetric objects as designed.

In this thesis, we present a novel concept in optics, which overcomes many difficulties in the fabrication of micro-optics and opens the new field of *3D printed micro- and nano-optics* with complex lens designs. Our work is just at the interface between micro- and nano-optics and represents a *paradigm shift for micro-optics*. It takes only a few hours from lens design, to production, testing, and the final working optical device. Using dip-in femtosecond two-photon direct laser writing, our method goes far beyond state-of-the art attempts to manufacture simple micro-lenses by lithography.

We prove the versatility of this method by writing different optics. Collimation optics, toric lenses, free-form surfaces with polynomials of up to 10th order for intensity beam shaping, as well as chiral photonic crystals for circular polarization filtering, all aligned onto the core of single mode fibers are shown. In addition, we show that three-dimensional direct laser writing is a suitable tool for the fabrication of complex multi-lens optical systems that show high quality optical imaging, beam shaping performance, and tremendous compactness with sizes below 300 µm.

We determine the accuracy of our optics by analyzing the imaging and beam shaping quality as well as characterizing the surfaces by atomic force microscope measurements and interferometric measurements. The method yields high fabrication accuracy and allows to manufacture of lenses with a rms (root mean square) surface roughness of less than 15 nm. The surfaces deviate from their designs by less than ±1 µm. Our 3D printed compound lenses feature resolving powers of up to 500 line pairs per millimeter. Our printed micro-optical elements can thus achieve

sufficient performance in order to enable compound lenses for high quality imaging.

In addition, we show the performance of diffractive optical elements with diameters of just 4.4 µm, which enable beam shaping at the end facet of an optical fiber. The intensity is shaped into a uniform or into a donut-shaped intensity distribution. For this purpose, the diffractive optics are directly fabricated onto the end facet of the optical fiber and show unprecedented performance for optical beam shaping.

Our method allows for a plethora of novel applications with tremendous impact on optical trapping of atoms and in-vivo imaging in the human body. In addition, applications for imaging and illumination in endoscopy, multiple sensors, and eyes for micro-robots can be realized.

ZUSAMMENFASSUNG

Additive Fertigung ermöglicht neuartige und noch nie dagewesene Herstellungs- und Konstruktionsmöglichkeiten, von denen vorhergesagt wird, dass sie einen massiven Einfluss im 21. Jahrhundert haben werden. Die Technologie erlaubt den einfachen dreidimensionalen Druck von massiven Objekten anhand einer Designvorgabe.

In dieser Arbeit stellen wir ein innovatives Konzept vor, welches viele Probleme und Schwierigkeiten in der gegenwärtigen Herstellung von Mikrooptiken umgeht und das Feld der 3D gedruckten Mikro- und Nanooptiken eröffnet. Die Optiken können dabei komplexe Linsendesigns aufweisen. Unsere Arbeit ist direkt an der Schnittstelle zwischen Mikro- und Nanooptik und stellt einen Wandel in der Denkweise in der Mikrooptikfabrikation dar. Unsere Herstellungsmethode erlaubt die Fabrikation von Mikrooptiken – vom optischen Designen bis zur Fabrikation - in nur wenigen Stunden. Mit Hilfe von direktem Laserschreiben geht unsere Methode weit über gegenwärtige Herangehensweisen zur Herstellung von einfachen Mikrooptiken hinaus. Wir nutzen dabei Femtosekundenlaserpulse, die mittels nichtlinearem Zwei-Photonen-Absorptionsprozess ein fotosensitives Material gezielt partiell polymerisieren.

Anhand der Fabrikation verschiedener Optiken demonstrieren wir die Vielseitigkeit unserer Methode. Insbesondere zeigen wir refraktive optische Elemente, wie Kollimationsoptiken, Zylinderlinsen, torische Linsen und Freiformflächen zur Strahlformung, sowie chirale photonische Kristalle zur Festlegung der Polarisation. Alle optischen Elemente werden dabei auf die Endflächen optischer Glasfasern hergestellt und submikrometergenau relativ zum Faserkern ausgerichtet. Damit wird eine Strahlformung in Intensität und Polarisation direkt an der Endfläche einer Glasfaser erreicht.

Zusätzlich zeigen wir, dass das drei-dimensionale, direkte Laserschreiben ebenfalls eine bewährte Möglichkeit zur Herstellung von komplexen Systemen mit mehreren Freiformlinsen ist. Die optischen Systeme weisen dabei eine hohe optische Abbildungsqualität, gute Strahlformungsperformance und eine überlegene Kompaktheit mit Größen unter 300 µm auf.

Wir bestimmen die Oberflächengüte und die Fabrikationstoleranzen unserer Optiken durch Analyse der Strahlformungs- und Abbildungsqualität sowie der Charakterisierung anhand von interferometrischen und Rasterkraftmikroskopmessungen. Durch die Verwendung von hochauflösenden Mikroskopobjektiven zur Fokusierung des Schreibstrahls bietet die Herstellungsmethode eine Genauigkeit im Sub-Mikrometerbereich. Dies ermöglicht die Herstellung von Linsensystemen mit Oberflächenrauheiten von weniger als 15 nm (quadratische Rauheit; englisch: root-mean-squared (rms) roughness). Die Oberfläche weicht dabei um weniger als ±1 µm vom Design ab. Unsere 3D gedruckten Linsensysteme weisen Auflösungsvermögen von bis zu 500 Linienpaaren pro Millimeter auf und erreichen damit eine ausreichende Leistungsfähigkeit um mehrlinsige Systeme für hochqualitative Abbildungen zu realisieren.

Ferner zeigen wir die Leistungsfähigkeit von diffraktiven optischen Elementen mit einem Durchmesser von nur 4,4 µm, die es ermöglichen den Lichtstrahl am Ende einer Glasfaser räumlich in eine gleichmäßige oder eine donutförmige Intensitätsverteilung umzuwandeln. Die diffraktiven Optiken werden dazu direkt auf die Endfläche der Glasfaser fabriziert.

Unsere Methode erlaubt eine Vielzahl von neuartigen Anwendungen für optische Pinzetten und die in-vivo Bildgebung im menschlichen Körper. Zusätzlich können Anwendungen in der Bildgebung und Beleuchtung für zahlreiche Sensoren, Mikroroboter und die Endoskopie realisiert werden.

CONTENTS

Abstract ix
Zusammenfassung xi
Publications 1
1 INTRODUCTION 7
  1.1 Outline 12
2 FABRICATION TECHNIQUES 15
  2.1 Direct laser writing 15
  2.2 Sample fabrication 18
3 SIMULATION TECHNIQUES 25
  3.1 Gaussian beam propagation - ABCD matrix formalism 26
  3.2 Huygens-Fresnel diffraction approach 32
  3.3 Optical design software 35
4 DIFFRACTIVE OPTICAL ELEMENTS 37
  4.1 Donut and top hat shaper 39
  4.2 Special beam shaping elements 50
5 PHOTONIC CRYSTALS 57
6 REFRACTIVE OPTICAL ELEMENTS 63
  6.1 Spherical lens - Beam collimator 64
  6.2 Cylindrical lens 73
  6.3 Toric lens 75
  6.4 Donut intensity shaper 81
  6.5 Circular top hat intensity shaper 88
  6.6 Square top hat intensity shaper 99
7 MULTI-LENS SYSTEMS 105
  7.1 Multi-lens systems for imaging 105
  7.2 Multi-lens systems for beam shaping 125
8 FABRICATION ISSUES 131
  8.1 Adaptation of the multi-lens surface shape 131
  8.2 Variation of the writing parameters 134
  8.3 Variation of the lens material 136
  8.4 Variation of the writing modes 138

8.5 Iterative method for improvement of the shape fidelity 142
Conclusion 147
Outlook 151
A REFRACTIVE INDEX MEASUREMENT 157
B RESOLUTION TARGETS 165
C SINGLE MODE FIBER SM 780HP 169
D FABRICATION PARAMETERS 173
E IMAGES 181
Bibliography 197
Acknowledgments 213
Curriculum Vitae 215

PUBLICATIONS

The following papers have been published in the context of this thesis.

SCIENTIFIC JOURNALS

[1] Marius Vieweg, Timo Gissibl, Sebastian Pricking, Boris T. Kuhlmey, Darran K. C. Wu, Benjamin J. Eggleton, and Harald Giessen. Ultrafast nonlinear optofluidics in selectively liquid-filled photonic crystal fibers. *Optics Express*, 18(24):25232, 2010.

[2] André Radke, Timo Gissibl, Thomas Klotzbücher, Paul V. Braun, and Harald Giessen. Three-Dimensional Bichiral Plasmonic Crystals Fabricated by Direct Laser Writing and Electroless Silver Plating. *Advanced Materials*, 23(27):3018–3021, 2011.

[3] Marius Vieweg, Timo Gissibl, and Harald Giessen. Photonic-crystal fibers are selectively filled with nonlinear liquids. *Laser Focus World*, 47(53), 2011.

[4] Timo Gissibl, Marius Vieweg, Moritz M. Vogel, Marwan Aboud Ahmed, Thomas Graf, and Harald Giessen. Preparation and characterization of a large mode area liquid-filled photonic crystal fiber: Transition from isolated to coupled spatial modes. *Applied Physics B: Lasers and Optics*, 106(3):521–527, 2012.

[5] Stefan Kedenburg, Marius Vieweg, Timo Gissibl, and Harald Giessen. Linear refractive index and absorption measurements of nonlinear optical liquids in the visible and near-infrared spectral region. *Optical Materials Express*, 2(11):1588, 2012.

[6] Marius Vieweg, Timo Gissibl, Yaroslav V. Kartashov, Lluis Torner, and Harald Giessen. Spatial solitons in optofluidic

waveguide arrays with focusing ultrafast Kerr nonlinearity. *Optics Letters*, 37(13):2454, 2012.

[7] Marius Vieweg, Sebastian Pricking, Timo Gissibl, Yaroslav Kartashov, Lluis Torner, and Harald Giessen. Tunable ultrafast nonlinear optofluidic coupler. *Optics Letters*, 37(6):1058, 2012.

[8] Shahin Bagheri, Ksenia Weber, Timo Gissibl, Thomas Weiss, Frank Neubrech, and Harald Giessen. Fabrication of Square-Centimeter Plasmonic Nanoantenna Arrays by Femtosecond Direct Laser Writing Lithography: Effects of Collective Excitations on SEIRA Enhancement. *ACS Photonics*, 2(6):779–786, 2015.

[9] Shahin Bagheri, Christine M. Zgrabik, Timo Gissibl, Andreas Tittl, Florian Sterl, Ramon Walter, Stefano De Zuani, Audrey Berrier, Thomas Stauden, Gunther Richter, Evelyn L. Hu, and Harald Giessen. Large-area fabrication of TiN nanoantenna arrays for refractory plasmonics in the mid-infrared by femtosecond direct laser writing and interference lithography. *Optical Materials Express*, 5(11):2625, 2015.

[10] Stefan Kedenburg, Timo Gissibl, Tobias Steinle, Andy Steinmann, and Harald Giessen. Towards integration of a liquid-filled fiber capillary for supercontinuum generation in the 12–24 μm range. *Optics Express*, 23(7):8281, 2015.

[11] Simon Thiele, Timo Gissibl, Harald Giessen, and Alois M. Herkommer. Ultra-compact on-chip LED collimation optics by 3D-printing. *In preparation*, 2015.

[12] Timo Gissibl, Michael Schmid, and Harald Giessen. Spatial beam intensity shaping using phase masks on single mode optical fibers fabricated by femtosecond direct laser writing. *Accepted for publication in Optica*, 2016.

[13] Timo Gissibl, Simon Thiele, Alois M. Herkommer, and Harald Giessen. 3D printing of ultra-compact multi-lens objectives. *Submitted*, 2016.

[14] Timo Gissibl, Simon Thiele, Alois M. Herkommer, and Harald Giessen. Sub-micrometer accurate free-form optics by 3D printing. *Accepted for publication in Nature Communications*, 2016.

PATENTS

[1] Harald Giessen and Timo Gissibl. Verfahren zur Herstellung von mikrooptischen Bauelementen mit Auflösungen unter einem Mikrometer auf optischen Glasfasern, DE 10 2015 012 980.5, 2015.

[2] Harald Giessen, Stefan Kedenburg, Timo Gissibl, and Andy Steinmann. Verfahren zur Verbindung einer optischen Festkernfaser mit einer Hohlkernfaser, DE 10 2015 003 652.1, 2015.

[3] Simon Thiele, Timo Gissibl, Harald Giessen, and Alois M. Herkommer. Verfahren zur Erzeugung von funktionalen Bereichen in gedruckten mikrooptischen Elementen, EP 15 003 086, 2015.

CONFERENCE PROCEEDINGS

[1] Timo Gissibl, Marius Vieweg, and Harald Giessen. Applications of selectively liquid-filled photonic crystal fibers. In *Photonics I, DPG Spring Meeting (Deutsche Physikalische Gesellschaft)*, page Q 43.3, Dresden, Germany, 2011.

[2] Timo Gissibl and Harald Giessen. Direct laser writing of complex photonic structures. In *Photonics West*, page 9374.11, San Francisco, USA, 2015.

[3] Timo Gissibl, Michael Schmid, Simon Thiele, Michael Thiel, Alois Herkommer, and Harald Giessen. 3D printing of submicrometer free-form optics on fiber tips. In *DPG Spring Meeting (Deutsche Physikalische Gesellschaft)*, page Q 66.3, Heidelberg, Germany, 2015.

POSTERS

[1] Timo Gissibl, Marius Vieweg, and Harald Giessen. Selectively closed liquid-filled photonic crystal fibers. In *DPG Spring Meeting (Deutsche Physikalische Gesellschaft)*, Hannover, Germany, 2010.

[2] Timo Gissibl, Marius Vieweg, Moritz M. Vogel, Marwan Abdou-Ahmed, Thomas Graf, and Harald Giessen. Preparation and characterization of a large mode area liquid-filled photonic crystal fiber: transition from isolated to coupled spatial modes. In *Workshop on Optical nanoantennas and hybrid quantum systems*, Bad Honnef, Germany, 2011.

[3] Timo Gissibl, Marius Vieweg, Stefan Kedenburg, Marwan Abdou-Ahmed, Moritz M. Vogel, Andreas Voß, Thomas Graf, Alois Herkommer, and Harald Giessen. Microstructured optical fibers. In *1st SCoPE Workshop*, Stuttgart, Germany, 2012.

[4] Timo Gissibl. The cake is a lie. In *Statusworkshop - Kompetenznetz Funktionelle Nanostrukturen*, Bad Herrenalb, Germany, 2013.

[5] Timo Gissibl. TV-Tower of Stuttgart. In *Statusworkshop - Kompetenznetz Funktionelle Nanostrukturen*, Bad Herrenalb, Germany, 2013.

OTHER CONFERENCE PROCEEDINGS

[1] Marius Vieweg, Timo Gissibl, and Harald Giessen. Application of Selectively Filled Photonic Crystal Fibers. In *DPG Spring Meeting (Deutsche Physikalische Gesellschaft)*, page Q60.2, Hannover, Germany, 2010.

[2] Marius Vieweg, Timo Gissibl, and Harald Giessen. Selectively Filled Photonic Crystal Fibers. In *Conference on Lasers and Electro-Optics, OSA Technical Digest (CD) (Optical Society of America)*, page CThB2, San Jose, USA, 2010.

[3] Marius Vieweg, Timo Gissibl, and Harald Giessen. Selectively Filled Photonic Crystal Fibers. In *Nonlinear Photonics, OSA*

Technical Digest (CD) (Optical Society of America), page NThA2, Karlsruhe, Germany, 2010.

[4] Yevgen Grynko, Jens Förstner, Torsten Meier, André Radke, Timo Gissibl, Paul V. Braun, Harald Giessen, and Dmitry N. Chigrin. Application of the Discontinuous Galerkin Time Domain Method to the Optics of Bi-Chiral Plasmonic Crystals. In *4th International Workshop on Theoretical and Computational Nanophotonics, TaCoNa-Photonics*, pages 76–78, Bad Honnef, Germany, 2011.

[5] Marius Vieweg, Timo Gissibl, Sebastian Pricking, Yaroslav V. Kartashov, Lluis Torner, and Harald Giessen. Selectively Fluid-filled Photonic Crystal Fibers. In *Conference on "Nonlinear optics and complexity in photonic crystal fibers and nanostructures"*, Erice, Italy, 2011.

[6] Marius Vieweg, Timo Gissibl, Sebastian Pricking, Yaroslav V. Kartashov, Lluis Torner, and Harald Giessen. Tuneable ultrafast nonlinear optofluidic coupler. In *XVIII International Conference on Ultrafast Phenomena*, Lausanne, Switzerland, 2012.

[7] Simon Thiele, Timo Gissibl, Harald Giessen, and Alois M. Herkommer. Wave optical optimization of a high NA fiber tip TIR lens. In *Classical Optics, OSA Technical Digest (CD) (Optical Society of America)*, page JTu5A.14, Kohala Coast, Hawaii, United States, 2014.

[8] Stefan Kedenburg, Timo Gissibl, Tobias Steinle, Andy Steinmann, and Harald Giessen. Towards integration of a liquid-filled fiber capillary for mid-IR supercontinuum generation. In *Photonics I, DPG Spring Meeting (Deutsche Physikalische Gesellschaft)*, page Q 66.2, Heidelberg, Germany, 2015.

[9] Frank Neubrech, Shahin Bagheri, Ksenia Weber, Timo Gissibl, and Harald Giessen. Fabrication of plasmonic nanoantennas by femtosecond direct laser writing lithography - effects of near field coupling on SEIRA enhancement. In *Sensing, Active Structures and other Applications, DPG Spring Meeting (Deutsche Physikalische Gesellschaft)*, page O 90.13, Berlin, Germany, 2015.

1

INTRODUCTION

Additive manufacturing enables novel and unprecedented engineering and production possibilities, which are predicted to have an enormous impact in the 21st century. The technology allows for the simple three-dimensional printing of volumetric objects as designed [1]. Multiphoton lithography is one of various 3D printing technologies, which realizes the fabrication of three-dimensional objects [2, 3, 4, 5]. By using femtosecond laser pulses and two-photon absorption, this manufacturing method takes 3D printing down to sub-micrometer feature sizes and thus follows the on-going trend of further miniaturization.

So far, additive manufactured objects are made out of metals, ceramics, and opaque plastics. However, femtosecond direct laser writing with highly transparent photoresists enables 3D printing in the nano- and micrometer region. Therefore, the precise fabrication of complex optical elements on demand becomes possible [6, 7, 8, 9].

Micro-optical elements of high quality are used in a large variety of applications such as telecommunication, sensing technology, and industrial inspection. These elements are usually integrated into systems that additionally contain electrical, mechanical, or other optical components. For this purpose, it is important to further miniaturize these optical elements to extend the field of applications to biotechnology and medical engineering. Integrated fiber-optical or complex lab-on-a-chip devices would also become possible.

In order to manufacture small and well performing micro-optical systems, a number of different fabrication methods exists so far [10, 11, 12, 13, 14, 15, 16, 17]. However, these technologies suffer from drawbacks such as limited miniaturization, lack of possibility to combine multiple elements, restriction in designing the surfaces [10, 11, 12, 18], and difficulties with the alignment [19].

In this thesis we lay out a route to overcome all aforementioned issues. We demonstrate that three-dimensional direct laser writing is a suitable tool in order to fabricate complex optical systems that show high optical performance and tremendous compactness. Complex elements for beam shaping, endoscopy, illumination, high-performance imaging, inspection, and microscopy on the micrometer scale are demonstrated. Micro-optical systems and even imaging systems with dimensions as small as a grain of salt can be realized. This leads to a plethora of applications in various fields such as biotechnology, medical engineering and safety monitoring. Endoscopic applications will allow for non-invasive and non-destructive examination of smallest objects in the medical and industrial sector.

As an example, Fig. 1.1 depicts an optical fiber equipped with a multi-lens system for imaging the interior of a hollow organ or cavity of the body. Using an injection cannula with an outer diameter of only 412 μm (27 Gauge) together with a fiber-coupled 3D printed multi-lens system, the insertion can be easily accomplished.

In this thesis we demonstrate the capabilities of femtosecond dip-in laser lithography for the manufacture of high quality optical elements with outstanding performance. We realize a variety of optical elements with different features for numerous applications.

Using direct laser writing we show micro-optical systems containing one or more complex free-form surfaces. Up to now multi-lens optics which show comparable performance are considerably larger [19, 20] and at the same time do not show the manifold compound structures and possibilities presented here.

The optical performance is quantified and analyzed by measuring the optical modulation transfer function and the longitudinal chromatic aberration. Additionally, we characterize the roughness and quality of the surfaces by atomic force microscope and interferometric measurements. As examples for applications, we show the performance of multi-lens systems manufactured on optical imaging fibers with 1600 pixels as well as on CMOS image sensors with pixel sizes of $1.4 \times 1.4\ \mu m^2$, while our lenses have

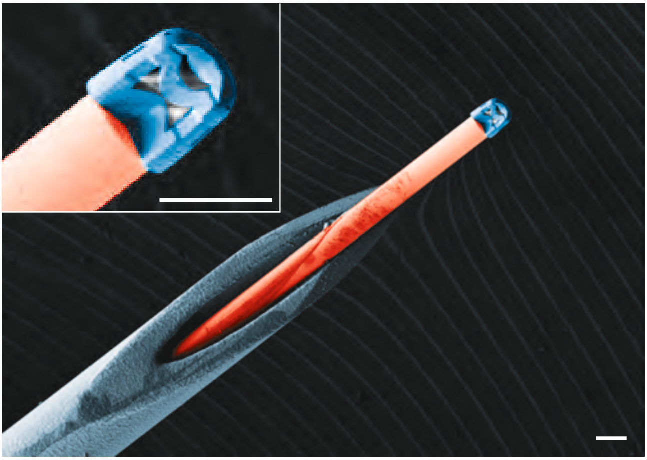

Figure 1.1. Colored scanning electron microscope image of a triplet lens attached to an optical fiber coming out of a cannula. The multi-lens system (blue) consists of five refractive surfaces for imaging applications directly fabricated on an optical fiber (red). The fiber is coming out of a hollow needle (gauge 27, outer diameter 412 µm, inner diameter 210 µm) in order to demonstrate the possibility of an endoscopic application. Scale bar, 150 µm.

diameters of not more than 120 µm and heights between 100 µm and 200 µm.

Additionally, we show the connection of free-form optics with fiber optics and realize a variety of optical elements for beam collimation, creation or correction of astigmatism, beam shaping, and polarization control at the end facet of single mode fibers.

Recently different approaches for combining micro-optical elements with fiber optics have been proposed. These have been using fabrication techniques such as focused ion-beam milling [21, 22], interference lithography [23, 24, 25], nano imprint technology [26, 27], photolithography [28], polishing techniques [29], through-fiber patterning [30, 31], UV curing of surface-tension shaped droplets in combination with coreless silica fibers [32, 33], inject printing of photocurable polymers [13, 34, 35], laser micromachining [36, 37], and two-photon polymerization [38, 39, 7, 8, 40, 41, 42, 43] to directly fabricate dielectric elements onto the end facet of an optical fiber. However, they all suffer from drawbacks such as low resolution, small fabrication volumes, the difficulty to achieve large heights, or complex fabrication setups. The additional restrictions imposed by the design of optical elements result in the fact that, to our knowledge, until now no combination of the specific design, fabrication, and verification of sub-micrometer free-form optics has been reported. In addition, free-form optics on single mode fibers with specific design targets cannot be fabricated by most of the mentioned methods.

As the miniaturization of lenses is fundamentally limited, diffractive elements such as phase plates provide tremendous advantages. Due to their surface profile phase plates generate a spatial phase shift and can be used as focusing or beam shaping elements [44]. We introduce for the first time 3D printed phase plates directly attached to optical single mode fibers. The emerged intensity profile is spatially redistributed into top hat and donut shaped intensity profiles. The surface patterns of the phase plates are calculated using Fresnel-Huygens diffraction theory. We demonstrate the viability of the fabrication technique for producing compact integrated optical elements by analyzing the optical performance of the diffractive optical elements.

Combining different optical materials for 3D printing and different optical elements will further enhance the possibilities of this fabrication method. Fig. 1.2 shows a free-form optical surface with a saddle-type shape aligned on a single-mode fiber. Below the micro-lens element a chiral three-dimensional photonic crystal structure for polarization filtering is fabricated and on top a diffractive polymer structure for beam shaping is imprinted. The working principle of the individual elements we be discussed below. However, the image already demonstrates the versatility of our method. In a two-step process we first fabricate the chiral photonic crystal structure as circular polarization filter on the end facet of an optical fiber using IP-Dip (Nanoscribe GmbH, Germany), in a second step we use the photoresist IP-S (Nanoscribe GmbH, Germany) to create the saddle-shaped free-form lens with a Fresnel zone plate on top. The different photoresists are chosen according to their writing characteristics.

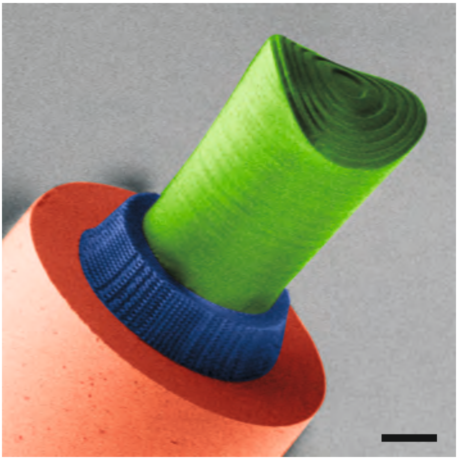

Figure 1.2. Polarization, diffractive, refractive and imaging optical elements in a sub-micrometer optical device directly attached to the end facet of an optical fiber. Colored scanning electron microscope image of a model device manufactured by three-dimensional direct laser writing. On top of the end facet of an optical fiber (red) a chiral photonic crystal structure (blue) for polarization control and a free-form lens with Fresnel zone plate (green) for beam shaping are placed. The optical components are fabricated using two different photoresists. Scale bar, 25 µm.

Our results proof that femtosecond three-dimensional direct laser writing is well suited for the manufacturing of high quality diffractive elements, refractive free-form surfaces, multi-lens systems, and photonic crystal structures with sub-micrometer feature sizes. Therefore, a plethora of applications with tremendous impact on imaging, illumination, beam shaping, and particularly on the microscale microscopy, endoscopy and inspection, will consequently be enabled. Optical trapping of atoms in vacuum, directly behind an optical fiber, will be possible using a high-NA printed compound lens on a single mode fiber. As imaging fibers are much smaller than 1 mm in diameter, in-vivo imaging, e.g., in the human brain without damage will become possible. If directly printed onto nitrogen-vacancy centers (NV centers) in diamond or on single quantum dots in their host material, our high-NA compound lenses can directly go into a cryostat and make the need for complex optics obsolete.

1.1 OUTLINE

In this thesis, we demonstrate for the first time controlled optical intensity and polarization shaping of light emerging from single mode fibers. We use diffractive and refractive optical elements fabricated by three-dimensional dip-in direct laser writing with sub-micrometer precision. In addition, we present for the first time multi-lens imaging systems with diameters well below 200 µm. Our approach differs from others by higher fabrication quality, more flexibility, and smaller sizes. For the first time, the specific design, fabrication, and performance measurements of optical elements is demonstrated, with an excellent agreement between design, simulation, and measurement.

In Chapter 2 we will introduce femtosecond dip-in direct laser writing, which enables three-dimensional structures with submicrometer feature sizes.

Chapter 3 will give a basic introduction into the simulation techniques. In particular, we will introduce Gaussian beam propagation using the ABCD matrix formalism, a Huygens-Fresnel diffraction approach, and optical design software for the simulation of refractive and diffractive optical elements.

In Chapter 4 we will discuss diffractive optical elements with diameters of 4.4 µm. The diffractive elements are directly fabricated on the core of a single mode fibers and shape the emerging intensity, creating top hat and donut shaped intensity distributions.

Chapter 5 focuses on the influence of the polarization state of light in the optical wavelength regime. We fabricate three-dimensional chiral photonic crystals on the end facet of optical single mode fibers by three-dimensional direct laser writing and demonstrate full control of the circular polarization state in the telecomunication wavelength region.

In Chapter 6 we will introduce refractive free-form optics with sub-micrometer resolution to shape the intensity of light emerging from an optical fiber. We show different surface shapes for creating numerous intensity distributions such as donut shaped, circular or quadratic shaped top hat intensity distributions and line focuses.

Chapter 7 will give an introduction to multi-lens imaging systems. We manufacture compound lenses with different numbers of surfaces starting from one to five refractive interfaces. In order to demonstrate the variety of our approach we fabricate the lens on substrates, imaging fibers, and image sensors.

In Chapter 8 we will discuss different fabrication influences on the optical performance. In particular, we study influences such as laser power, writing mode, lens material, and surface shape.

2

FABRICATION TECHNIQUES

Additive manufacturing or 3D printing is one of the most important trends in engineering and production and will have a major impact in the 21st century. Direct laser writing, and in particular, multiphoton manufacturing with femtosecond laser pulses has taken additive manufacturing all the way down to the 100 nm length scale and even below [45, 46, 47]. Using optical transparent materials this technique opens the door for the fabrication of complex and at the same time high quality optical elements - nearly impossible for other fabrication methods.

The ultra-compact optics presented in this work are fabricated by direct laser writing utilizing a commercially available femtosecond laser lithography system (Photonic Professional GT, Nanoscribe GmbH, Germany).

2.1 DIRECT LASER WRITING

Direct laser writing is a versatile fabrication technique in order to manufacture one- to three-dimensional structures with sizes in the range from 100 nm to a few millimeters [3, 4, 5, 45]. Multiphoton polymerization in a photoresist is used in order to create dielectric structures. The method allows for the flexible fabrication of complex structures by exposing either negative-tone or positive-tone photoresists.

By using direct laser writing resists are illuminated by light with energies below the single-photon polymerization threshold. Two-photon absorption enables the exposure and thus the polymerization of the resist. Therefore, the photoresist has to be highly transparent for the incident laser beam, but absorbing at $\lambda/2$, where λ is the wavelength of the laser beam. Usually, infrared laser beams and thus UV-sensitive photoresists are used.

As two-photon absorption is a nonlinear process it is highly sensitive to the intensities of the incident radiation field. The transition rate p for a single-beam two-photon absorption process can be written as

$$p \propto \mathrm{Im}\left(\chi^{(3)}\right) I^2, \tag{2.1}$$

i.e., the transition rate is proportional to the imaginary part of the third-order nonlinear susceptibility $\chi^{(3)}$ and proportional to the square of the incident light intensity I [48].

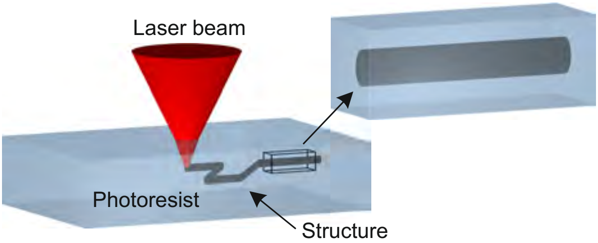

Figure 2.1. Schematic illustration of the function principle of direct laser writing. A laser beam is tightly focused into a photoresist. Due to two-photon absorption the resist is only exposed in a small volume around the focus.

In order to obtain two-photon absorption in photoresists pulsed lasers and tight focusing are usually used. Due to a threshold only in a small volume element around the focus the exposure process can take place. This volume element, the so called *voxel*, is the smallest building block for creating direct laser written structures. Since objectives with a high numerical aperture (high-NA objectives) are used to focus the laser beam, the intensity distribution of the focal region has to be calculated by vector diffraction theory [49, 50, 51]. This method allows for the prediction of optical aberration, which causes a non-spherical voxel shape. For two-photon absorption the shape of the voxel is dependent on the iso-intensity surface of the objective and the exposure threshold of the photoresist.

Calculations as well as experiments show, that the volume element can be seen as a prolate spheroid with the long axis in axial direction and a circular cross section in radial direction. Theory predicts an aspect ratio of 2.7 for an oil immersion objective with a numerical aperture of 1.4. In experiments aspect ratios between 3 and 10 are obtained.

Figure 2.1 shows a schematic illustration of the two-photon exposure process in a photoresist. During the fabrication the two-photon voxel can be seen as a writing tip that can be moved through the photoresist in three dimensions. Thus, this technique is called three-dimensional direct laser writing. Arbitrary structures can be created by moving the small volume element through the photosensitive medium.

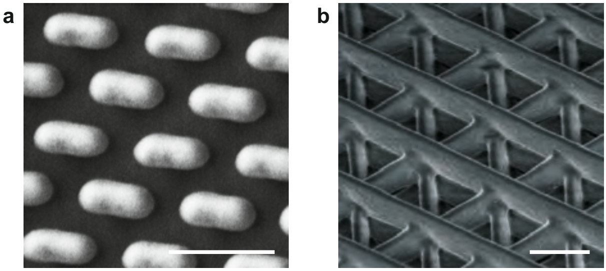

Figure 2.2. Examples of structures fabricated by direct laser writing. Direct laser writing allows for the fabrication of one to three-dimensional dielectric structures. **a,** One-dimensional structure: Dielectric nano-antenna array fabricated on a gold covered substrate. **b,** Three-dimensional structure: Periodic dielectric structure consisting of rotated nano-wire layers. Scale bars, 1 µm.

As dielectric structures can be directly fabricated in one to three dimensions, this technique leads to a plethora of applications in various fields such as biotechnology [52, 53, 54], photonics [55, 56, 57, 58], and micro engineering [59, 60, 61]. Fig. 2.2a depicts an example of one-dimensional structures. Nanoantennas are fabricated on a gold covered substrate in order to create plasmonic metal structures for sensing applications [58, 62]. In Fig. 2.2b a periodic dielectric structure in three dimensions is shown. The structure consists of parallel rods arranged in layers, where the layers are rotated by an angle of 120°. More details of this structure can be found in Chapter 5.

2.2 SAMPLE FABRICATION

The ultra-compact lenses are fabricated by direct laser writing utilizing a commercially available femtosecond laser lithography system. The optics are created by two-photon absorption in ultraviolet sensitive photoresists exposed at a wavelength of 780 nm. Every sub-micrometer accurate optical element consists of commercially available photoresist that exhibit high optical quality (Nanoscribe IP-S, Nanoscribe IP-Dip, microresist Ormocomp).

2.2.1 *Structure definition*

Before writing the structures are programmed either manually or by a computer-aided design software (CAD software).

In case of manually programmed structures each written line is defined by hand using Matlab. The structures are directly defined in trajectories, along which the laser focus moves and exposes the structure.

Complex structures with multiple lenses are designed by an optical design software, exported into a CAD-file format and subsequently transferred into a stereo lithographic file format (stl-format). The stl-file is again transferred into trajectories by means of slicing and hatching distance as well as hatching angle.

The definitions of these parameters and more details can be found in the Chapter D in the appendix.

In order to fabricate the three-dimensional structures different configurations and fabrication methods can be used.

2.2.2 *Fabrication in conventional configuration*

Fig. 2.3a shows the conventional configuration, which has been used since the early days of direct laser writing. As high-NA objectives are used to tightly focus the laser beam into the photoresist, immersion oils are necessary. Therefore, the oil is separated by the substrate from the photoresist in order to avoid mixing. The refractive index of substrate and immersion medium

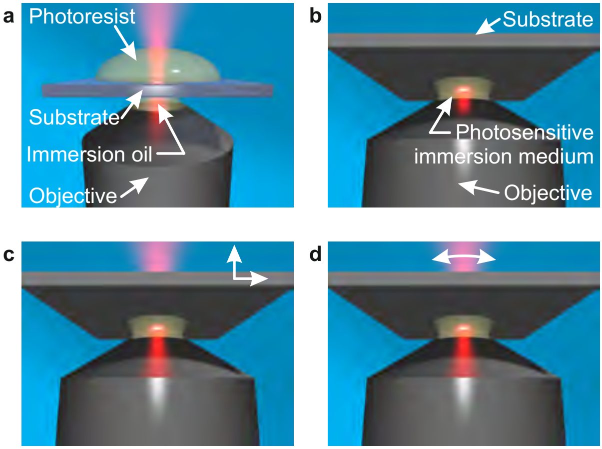

Figure 2.3. Direct laser writing configurations and fabrication methods. a, Conventional configuration: photoresist and immersion oil are separated by a substrate or cover glass. **b,** DiLL configuration: The photosensitive medium is directly placed onto the objective lens. **c,** Piezo scan mode: The substrate is moved in three dimensions by ultra-precise piezo actuators with respect to the laser focus. **d,** Galvo scan mode: In lateral direction the laser beam is guided by galvanometric mirrors parallel to the substrate.

are matching in order to get the ideal focus at the position of the substrate/photoresist interface. The maximum structure height is limited by the working distance of the microscope objective as well as the thickness of the substrate. The higher the fabricated structures, the worse the quality of the focus becomes due to spherical aberration which occur because of the refractive index mismatch between photoresist and substrate. An additional reason is that the structures have to be exposed through the already existing structure parts [63].

2.2.3 *Fabrication in dip-in configuration*

In order to fabricate the structures, which are presented in this thesis, dip-in laser lithography (DiLL) configuration is used [64, 57, 65]. Fig. 2.3b depicts the configuration. The photosensitive medium is directly placed onto the objective lens. The photoresist acts simultaneously as immersion medium, and the hosting substrate can be directly dipped into the photosensitive immersion material, which is necessary for high-NA objectives. As this lithography method is not limited to small element volumes and limited fabrication heights caused by the working distance limitation of the objective lens, this technique is well suited for an application as presented here. Additionally, this method is not limited to a specific substrate, and no complex holding and container system for the fiber and/or the photoresist is required [8]. Due to the index matching of the photoresists there is a constant perfect focus over the whole writing range. No additional spherical aberration occur due to additional interfaces [63].

Due to the use of a high-NA immersion objective, feature sizes below 200 nm can easily be achieved (Fig. 2.2). Additionally, the direct fabrication of up to cubic millimeter free-form optics with a sub-micrometer resolution on nearly any kind of hosting element or substrate can be realized.

The designed refractive and compound optics are written layer-by-layer with distances ranging from 50 to 800 nm between the individual layers. In order to write single layers piezo actuators as well as galvanometric mirrors are used, as discussed below.

2.2.4 *Fabrication by piezo actuators*

Figure 2.3c depicts the piezo scan mode in dip-in laser lithography configuration. The voxel stays at a fixed position, while the substrate is moved in three-dimensions by ultra-precise piezo actuators. During the exposure process the substrate can be moved along trajectories in all three dimensions. Therefore, structures with complex shapes can be easily manufactured.

2.2.5 *Fabrication by galvanometric mirrors*

In Fig. 2.3d the galvo scan mode is depicted. In lateral direction the laser beam is guided by galvanometric mirrors parallel to the substrate. Ultra-precise piezo actuators move the sample in axial direction after fabricating one layer in x- and y-direction.

As mentioned, dip-in laser lithography is not limited to specific substrates, small optical element volumes or fabrication heights. The direct fabrication of up to cubic millimeter free-form optics with a sub-micrometer resolution on nearly any kind of hosting element or substrate can be realized. We demonstrate imaging with micro-optics manufactured on glass substrates, on CMOS sensors, and on end facets of fibers.

2.2.6 *Fabrication on substrates*

As substrates cover glasses with a thickness of 170 µm are used. The direct laser writing system is equipped with an interface finder algorithm, based on Zeiss Definite Focus. Refractive index differences are detected and the interface between substrate and photoresist can be adjusted automatically. Of course, this is only possible, if the refractive index difference between substrate and photoresist is large enough.

2.2.7 *Fabrication on CMOS sensors*

As CMOS sensors Omnivision 5647 CMOS image sensors are used. Before manufacture on the sensor, we scrape off the microlens layer by using a wooden spatula. The interface can be automatically found and adjusted by the interface finder. As the sensor chip exhibit a high reflection the laser power is reduced in order to avoid overexposure.

2.2.8 *Fabrication on optical fibers*

As optical fibers we use single mode (SMF-28, Newport and SM 780HP, Thorlabs) and imaging fibers (FTIFHR160S-1600, F&T Fibers and Technology GmbH, Germany). The fibers are mounted using a standard fiber holder with V-groove (Elliot Martock MDE 710) directly attached to a holder of the direct laser writing system. The fiber pieces are not limited in length, but typically lengths of 15 to 20 cm are used. The fibers are directly cleaved before the direct laser writing process.

Backside illumination of the fiber is used to accurately center the fiber core with respect to the writing beam by observing the end facet of the fiber with a CCD camera. Only a power of a few percent of the writing power is used in order to see the laser on the fiber end facet and align the fiber core, accordingly. This method can also be used for hybrid systems consisting of two different photoresists, as shown in Fig. 1.2.

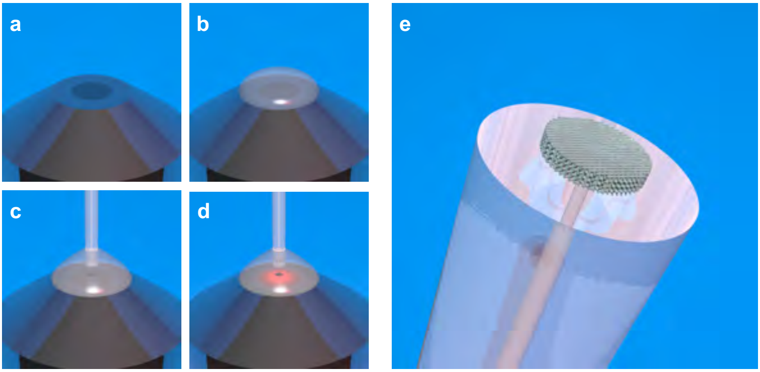

Figure 2.4. Illustration of the fabrication process on optical fibers using femtosecond direct laser writing. On the objective lens **(a)** a droplet of photoresist is put **(b)**. Subsequently, the fiber is dipped into the photosensitive medium **(c)** and accurately aligned by observing the end facet of the fiber with a CCD camera. In a following step the structure is exposed by two-photon absorption **(d)**. After the development process the direct laser written structure is perfectly centered on the core of the optical fiber **(e)**.

Figure 2.4 shows an illustration of the direct laser writing process on optical fibers. A droplet of the photoresist is put on the objective lens and subsequently, the fiber is dipped into the photoresist. After aligning the fiber, the two-photon direct laser writing process is executed. In order to develop the structure the unexposed photoresist is removed in a development bath. Using this method the structure is perfectly centered on the core of the optical fiber.

The photoresists are chosen according to their writing characteristics. Namely, we use a photoresist with a high resolution for the photonic crystal structures and diffractive optical elements, whereas refractive optics are fabricated by photoresists with lower resolution, such that smoother surfaces are achieved.

IP-Dip is a liquid, high resolution photoresist for the fabrication of detailed structures and perfectly suited for diffractive optics, nanoantenna arrays, and photonic crystals. IP-S and Ormocomp are liquid resists with high proximity effects and can be excellently utilized for the fabrication of refractive optical elements. All resist can be used for direct laser writing in dip-in configuration.

2.2.9 *Development*

After the writing process, the lenses are developed in a bath of developer (microresist mr-dev 600 for IP-photoresists, microresist OrmoDev for Ormocomp) for 20 min and a subsequent rinsing bath of isopropanol for 2 min.

After development the larger samples are dried by a constant air flow. Since the surface of fiber end facets and the structure is very small, in this case, no drying is necessary.
It should also be noted that all these photoresists do not need baking steps nor other treatments.

The described fabrication methods allow for optical elements with unprecedented high optical quality.

3

SIMULATION TECHNIQUES

Optical elements influence the propagation of light by interference, reflection, refraction, or diffraction [66]. The influence of refractive optical elements, such as lenses can be described by using Snell's law of refraction, which is given by

$$n_1 \sin \alpha = n_2 sin\beta. \tag{3.1}$$

In this formula n_1 and n_2 are the refractive indices of the two materials. α is the angle of incidence and β is the angle of refraction. Snell's law can be derived from Fermat's principle of the shortest optical path [67] and constitutes the bases of geometrical optics.

Based on geometrical optics simple reflective and refractive optical elements can be calculated. Light is assumed to propagate in rays, which are represented by straight lines. Diffraction and interference are not considered in geometrical optics. In order to simplify geometrical optics even more, often only paraxial rays are considered. Paraxial optics describes the first order properties of optical systems. In first-order optics, the trigonometric functions are replaced by their first order Taylor expansion. Due to this approximation the optical components can be described by linear mathematical operations, which can be represented by matrices [68].

In order to describe our ultra-compact optical elements we use different simulation methods.

The refraction of Gaussian beams at simple structures like spherical surfaces can be described by Gaussian beam propagation with the use of the ABCD matrix formalism. In order to describe complex surfaces like free-form optics or diffractive optics this ansatz is not sufficient anymore. In this cases, we numerically solve the Huygens-Fresnel diffraction integral in order to describe complex surfaces. For simulation and theoretical characterization of multi-

lens systems an optical ray tracing software is used.
The approaches are described in detail below.

3.1 GAUSSIAN BEAM PROPAGATION - ABCD MATRIX FORMALISM

In fiber optics single mode fibers guide light in the fundamental mode by using refractive index steps between core and cladding material and small core diameters. This results in the suppression of higher order modes for the designed wavelength and only the fundamental mode is guided. Thereby, the core refractive index is slightly higher than the one of the cladding for nearly all commercially available fibers. The field distribution of the fundamental transverse mode of a single mode fiber with a core radius a can be obtained by mode theory [69, 70, 71]. By solving the wave equation the electric field distribution of the LP_{01} mode can be written as

$$E_x = E_0 \begin{cases} \frac{J_0(p\rho)}{J_0(pa)} \exp(i\beta z) & \text{for } \rho \leqslant a \quad \text{core} \\ \frac{K_0(q\rho)}{K_0(qa)} \exp(i\beta z) & \text{for } \rho > a \quad \text{cladding,} \end{cases} \tag{3.2}$$

where LP means linearly polarized. J_0 and K_0 are the Bessel functions and the modified Bessel function of 1. order, respectively. ρ and z represent the polar coordinate system and stand thus for the radial distance and the propagation distance. a is the radius of the fiber core, which typically is between 2 and 5 µm for single mode fibers. i represents the imaginary unit ($i^2 = -1$). E_0 is a constant related to the power of the guided mode.
The parameters p and q are defined as

$$p = \sqrt{(n_1^2 k_0^2) - \beta^2} \tag{3.3}$$

and

$$q = \sqrt{\beta^2 - (n_2^2 k_0^2)} \tag{3.4}$$

and can be seen as modified normalized transverse wave numbers. n_1 and n_2 are the refractive indexes of core and cladding material, respectively. k_0 represents the wave vector with

$k_0 = \frac{2\pi}{\lambda}$, where λ is the wavelength of the propagating light. β is the propagation constant, which can be determined by numerically solving the eigenvalue equation of cylindrical wave guides. The eigenvalue equation describes the cross section of the fiber and can be derived from Maxwell's equations.

The radial intensity profile of the LP_{01} mode derived from the electric field distribution of Equation 3.2 can be well approximated by a Gaussian profile. Therefore, the fundamental mode emerging from an optical single mode fiber is well described by a Gaussian beam with the beam waist directly at the end facet of the fiber.

In optics, Gaussian beams play a crucial role, as lasers operate in the fundamental transverse mode and emit beams with Gaussian beam profiles. This means that the intensity as well as the electric field distribution is well described by Gaussian curves. In contrast to fiber optics, this mode is called fundamental transverse mode or TEM_{00} mode.

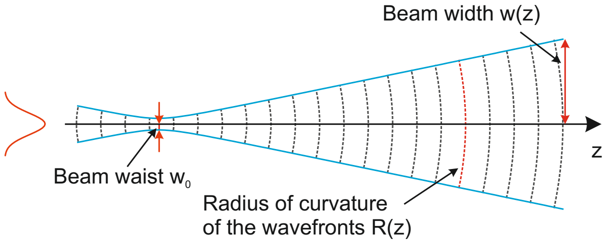

Figure 3.1. Schematic illustration of the propagation of a fundamental Gaussian mode. At the position of minimal beam width a nearly plane wave front is obtained.

Figure 3.1 shows a schematic illustration of the propagation of a Gaussian beam. It is described by the beam waist w_0, the Rayleigh parameter $z_0 = \frac{\pi w_0^2}{\lambda}$, the radius of curvature of the wavefronts $R(z)$, and the beam width $w(z)$, where z is the propagation distance of the Gaussian beam. λ is the wavelength of the Gaussian beam. Beam waist and beam width correspond to the radius of the beam, where the intensity drops down to $1/e^2$.

The electric field distribution of the fundamental Gaussian beam mode can be described by

$$E(r, z) = E_0 \frac{w_0}{w(z)} \exp\left(-\frac{\rho^2}{w^2(z)} - ikz - ik\frac{\rho^2}{2R(z)} + i\eta(z)\right), \quad (3.5)$$

where the beam width is given by

$$w(z) = w_0 \sqrt{1 + \left(\frac{z}{z_0}\right)^2} \quad (3.6)$$

and the radius of curvature of the wavefront is given by

$$R(z) = z\left(1 + \left(\frac{z_0}{z}\right)^2\right). \quad (3.7)$$

ρ and z represent the polar coordinate system, where the radial distance is given by $\rho = \sqrt{x^2 + y^2}$. E_0 is the maximal amplitude of the electric field at the position of the minimal beam width (corresponds to the position of the beam waist). η is the Gouy phase shift, which is given by

$$\eta = \arctan\left(\frac{z}{z_0}\right). \quad (3.8)$$

The Gouy phase indicates that a Gaussian beam acquires a different phase shift than a plane wave with the same wavelength. Thus, a phase shift of π is added by going through the focus.

Advantageously, Gaussian beams are transformed into Gaussian beams when they get refracted. Therefore, the description of optical systems with Gaussian beams is a convenient method. In addition, the ray transfer matrix analysis (ABCD matrix analysis) can be applied to the Gaussian beam parameters.

In the ABCD matrix formalism optical systems can be described by ray transfer matrices and rays are represented by vectors. Therefore, the tracing through an optical system is the multiplication of the transfer matrix of the optical system with the vector, describing the incident light ray. Thus, the light propagation is considered along the optical axis in the paraxial approximation of ray optics, where rays are assumed to have small angles and small distances with respect to the optical axis of the system.

Rays of light are described by the distance r and the angle α in relation to the optical axis. The matrix formalism is represented by the expression

$$\begin{pmatrix} r_2 \\ \alpha_2 \end{pmatrix} = \begin{pmatrix} A & B \\ C & D \end{pmatrix} \begin{pmatrix} r_1 \\ \alpha_1 \end{pmatrix}, \tag{3.9}$$

where the indices 1 and 2 refer to two planes in front of and after the optical system. In each case, the planes are perpendicular to the optical axis.
For example the propagation in free space or in a medium with constant refractive index is described by the matrix

$$M = \begin{pmatrix} 1 & d \\ 0 & 1 \end{pmatrix}, \tag{3.10}$$

where d is defined as shown in Table 3.1. An overview over a few ray transfer matrices are summarized in Table 3.1 [72]. The transfer matrix of complex optical systems can be calculated by multiplying the matrices of the several operations and thus determine the ABCD matrix of the complete optical system.

In order to describe the refraction of Gaussian beams by the ray transfer matrix formalism the Gaussian beam has to be represented by the parameters w_0 and z_0 or by the complex q parameter. It is defined as

$$q(z) = z + iz_0, \tag{3.11}$$

where i is the imaginary unit. Therefore, the transfer through an optical system can be described as

$$q_2 = \frac{Aq_1 + B}{Cq_1 + D}, \tag{3.12}$$

where the indices 1 and 2 represent two planes in front of and after the system. The q_j parameter contains information about the beam width $w(z)$ and the radius of curvature of the wavefront $R(z)$ at position j. This can be explicitly seen in the equation of the reciprocal q parameter, which is

$$\frac{1}{q(z)} = \frac{1}{R(z)} - \frac{i\lambda_0}{\pi n w^2(z)}. \tag{3.13}$$

Operation		ABCD matrix
Translation	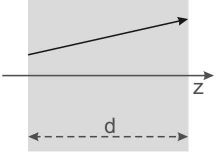	$\begin{pmatrix} 1 & d \\ 0 & 1 \end{pmatrix}$
Refraction Flat surface	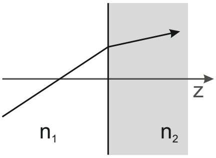	$\begin{pmatrix} 1 & 0 \\ 0 & n_1/n_2 \end{pmatrix}$
Refraction Spherical surface	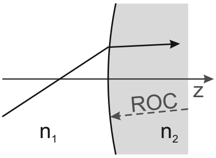	$\begin{pmatrix} 1 & 0 \\ \frac{n_1-n_2}{n_2 ROC} & \frac{n_1}{n_2} \end{pmatrix}$

Table 3.1. Overview over a few ray transfer matrices.

In order to describe a refractive optical element consisting of one spherical surface attached to an optical single mode fiber different ray transfer matrices are necessary. Fig.3.2 shows a schematic illustration of the optical system with the different ABCD matrices. The matrices are described in Table 3.1 in detail. Starting from a Gaussian beam with a beam waist w_0, emerging from an optical fiber, there is a transition from the core material n_{core} to the lens material n_{lens}. Subsequently, the beam propagates in the lens material over a distance D, which represents the lens thickness, followed by the refraction at a spherical surface with a certain radius of curvature (ROC) and a refractive index transition from n_{lens} to n_{air}. Finally, the beam propagates a certain distance L in air.

Using this method different lens thicknesses D in combination with varying ROCs are simulated. For example, in order to obtain a collimated beam after the optical fiber the beam width at a distance L is minimized. The distance L is set to be in the far field, which means $L \gg z_0$.

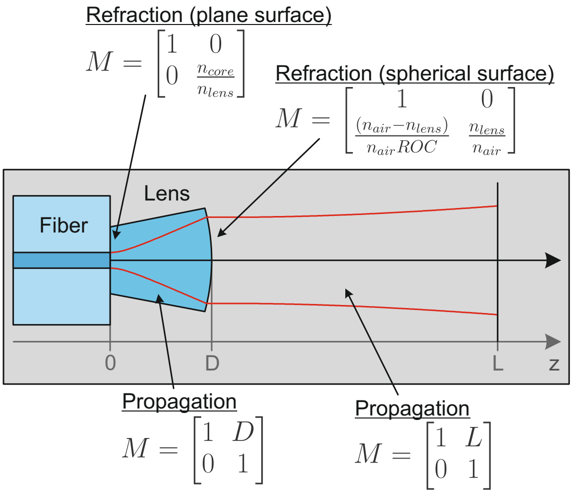

Figure 3.2. Schematic illustration of the ray transfer matrix formalism describing a refractive optical element consisting of one spherical surface attached to an optical single mode.

We cross check our simulation approach using Gaussian beam propagation with an ABCD matrix formalism by comparing the results with a Huygens-Fresnel diffraction approach (see Section 3.2) and simulations performed by using the optical design software Code V. Fig. 3.3 shows the simulation results. The ABCD matrix formalism is represented by the red line and the Huygens-Fresnel diffraction approach is indicated by the blue line. The dashed green line represent the Code V simulations. All simulations results are in excellent agreement.

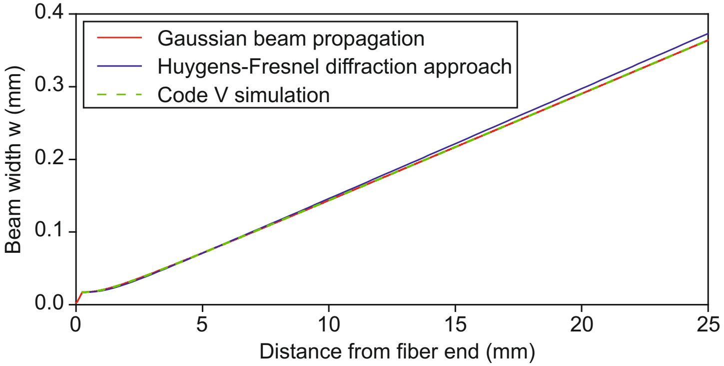

Figure 3.3. Comparison of the used simulation techniques. Comparison of simulations performed by Gaussian beam propagation based on ABCD matrix formalism, an Huygens-Fresnel diffraction approach and Code V simulations.

3.2 HUYGENS-FRESNEL DIFFRACTION APPROACH

In order to describe more complex optical surfaces the ray transfer matrix formalism is not sufficient any more. In this case, we numerically have to solve the Huygens-Fresnel diffraction integral.

According to Huygens' principle, each point of a wavefront of an electric-magnetic wave may be seen as a center of disturbance, which is a new source of a spherical wave. The wavefront at any subsequent time may be represented by the envelope of these secondary spherical waves. Fresnel extend Huygens' principle by adding the postulate, that the secondary spherical wave mutually interfere [67, 73, 74]. Concerning this, he additionally considered phase and amplitude of the Huygens' wavelets and an inclination factor (obliquity factor).

Using the Huygens–Fresnel principle the influence of optical elements on the light propagation can be described. Reflection, refraction, diffraction, and interference are thus taken into account by the Huygens-Fresnel principle.

As we consider optical elements directly attached to the end facet of single mode fibers we use the Huygens-Fresnel diffraction formula for Gaussian beams.

Figure 3.4 illustrates the geometry of the Huygens-Fresnel diffraction integral formulation for a Gaussian laser beam emerging from an optical fiber.

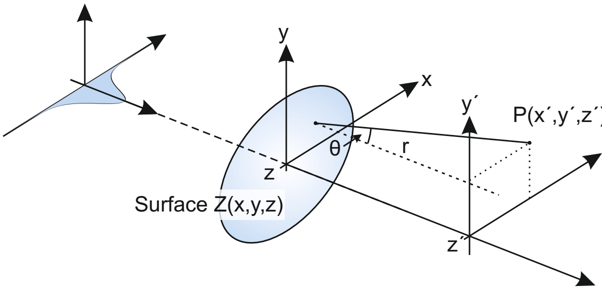

Figure 3.4. Geometry of the Huygens-Fresnel diffraction integral formulation for a Gaussian laser beam emerging from an optical fiber.

The refractive surface shape is given by an arbitrary function $Z(x, y, z)$. The refractive index of the lens material is n_{lens}.

The Gaussian field distribution at the surface can be described as

$$E_S(x, y, z) = E_0 \frac{w_0}{w(z)} \exp\left(-\frac{\rho^2}{w(z)^2} - ik_m Z(x, y, z) - \frac{ik_{\text{lens}}\rho}{2R(z)} + i\eta\right), \tag{3.14}$$

which results from the definition of the Gaussian beam in Equation 3.5 with the radial coordinate $\rho = \sqrt{x^2 + y^2}$. The Rayleigh parameter z_0 is given by

$$z_0 = \frac{\pi w_0^2 n_{\text{lens}}}{\lambda}, \tag{3.15}$$

where w_o is the beam waist and λ represents the wavelength of the Gaussian beam. The beam width $w(z)$ is

$$w(z) = w_0 \sqrt{1 + \left(\frac{z}{z_0}\right)^2} \tag{3.16}$$

and the radius of curvature R(z) is

$$R(z) = Z\left(1 + \left(\frac{z_0}{Z}\right)^2\right). \tag{3.17}$$

The Gouy phase shift η is given by

$$\eta = \arctan\left(\frac{Z(x,y,z)}{z_0}\right). \tag{3.18}$$

According to the Huygens-Fresnel-Kirchhoff diffraction integral formulation the electric field at a position $P(x',y',z')$ can be written as

$$E_P(x',y',z') = \frac{-i}{2\lambda}\iint_A E_S(x,y,z)\frac{e^{-ik_{\mathrm{air}}R}}{R}\kappa(\theta)\,dA, \tag{3.19}$$

where A is the aperture in the x-y-plane [75, 76]. The first expression in the integral describes the beam propagation from the beam waist to the aperture plane. In our case the propagation from the end facet of the optical fiber, through the optical element to the surface. The second term describes the subsequent propagation from the aperture to the observation plane.
$\kappa(\theta)$ is the obliquity factor

$$\kappa(\theta) = (1 + \cos\theta), \tag{3.20}$$

with the angle θ as shown in Fig. 3.4. Additionally, it is

$$\cos\theta = \frac{z' - z}{R}. \tag{3.21}$$

$$R = \sqrt{(x'-x)^2 + (y'-y)^2 + (z'-Z)^2} \tag{3.22}$$

represents the distance between the surface and the observation point. The wave vector k in air is k_{air}.

In order to calculate the refractive surface the Huygens-Fresnel-Kirchhoff diffraction integral formulation is implemented in an optimization algorithm. For this purpose, the structure of the optical element is iteratively improved such that the resulting intensity distribution converges to the desired one.

Consequently, this method allows for the simple and fast calculation of the optical structure for a desired intensity profile, as well as the intensity distribution at the observation plane for a given optical structure.
Thus, we calculated different diffractive and refractive optical elements attached to optical single mode fibers, including diffractive beam shaping elements and refractive free-form surfaces.

By using symmetry properties the Huygens-Fresnel-Kirchhoff diffraction integral (Equation 3.19) can be reduced in complexity and thus in computing time. For example, the integration dimension can be reduced for a rotationally symmetric surface to an integration along the radial coordinate.

As already seen in Fig. 3.3 the simulation results obtained by the Huygens-Fresnel-Kirchhoff diffraction integral approach are in excellent agreement with the results of the ray transfer matrix analysis (ABCD matrix analysis) and the optical design software results.

3.3 OPTICAL DESIGN SOFTWARE

More complex optical systems consisting of numerous optical elements are designed by an optical design software. Well-known programs are ZEMAX and Code V, which are used in optical engineering in order to design and optimize optical devices. In order to design a complex system different requirements exist. Among optical requirements, there can be physical and environmental needs to the system. Therefore, designing an optical device can be really challenging.

In order to calculate multi-lens systems we use the optical design software ZEMAX to design and optimize optical elements. ZEMAX can be used for designing, simulating and analysis of both imaging as well as illumination systems. For example, it can be used to design camera lenses, microscope objectives, or just components of optical instruments.

Optical design software usually use ray tracing in order to model the propagation of rays through optical systems. In addition, ZEMAX can work with physical optics to analyze optical systems, where diffraction becomes important. For stray light analysis ZEMAX can perform non-sequential ray tracing.

By defining the incident light field, the wavelength, the surface locations, the surface profiles, and the lens material(s) an optical design software calculates the performance of the system. Optimization tools can help to improve the optical design [77].

In order to compensate for optical aberrations and improve the image quality for each surface, we used aspherical surfaces $Z(\rho)$. They are the most common surface shape and are represented by

$$\begin{aligned} Z(\rho) = \frac{c\rho^2}{1+\sqrt{1-(1+k)c^2\rho^2}} + \dots \\ a_1 \cdot \rho + a_2 \cdot \rho^2 + \dots, \end{aligned} \tag{3.23}$$

where $\rho = \sqrt{x^2+y^2}$ is the radial distance and implies that the surface is rotationally symmetric. c is the curvature at the apex of the surface and the reciprocal of the radius of curvature (ROC). k represents the conic constant. The surface can be a hyperboloid for $k < -1$, a paraboloid for $k = -1$, a prolate spheroid for $-1 < k < 0$, a sphere for $k = 0$, and oblate spheroid for $k > 0$. a_1, a_2, ... are the deformation coefficients. If they are all 0, it results in a pure conic surface.

The performance of our designed lenses are evaluated by calculating the modulation transfer function (MTF). As the name implies it refers to the image modulation and thus to the contrast. The MTF gives a measure for the contrast as a function of of the spatial frequency. The modulation is calculated from

$$M = \frac{I_{max} - I_{min}}{I_{max} + I_{min}}, \tag{3.24}$$

where I is the intensity [78].

4

DIFFRACTIVE OPTICAL ELEMENTS

Due to their surface profile diffractive optical elements generate a spatial phase shift and can thus be used as focusing or beam shaping elements [44]. Instead of refraction or reflection, phase plates use diffraction in order to influence the light and thus can be smaller and lighter than equivalent refractive optical elements. The individual zones making up the diffractive optical elements differ from each other by different optical path lengths.

Up to now, these kind of optical elements are applicable in different fields including photography, illumination, material processing, and security features in documents and banknotes. Most of the application benefit from the small component size and the light weight.

Conventionally, phase plates are fabricated by lithographic techniques such as gray-scale, multiple mask, and moving mask lithography, followed by various etching processes [79, 80, 81]. These techniques are well suited for the fabrication of large-area samples but are cost and time intensive for prototyping. In the recent past, nonlinear fabrication approaches such as femtosecond laser surface ablation were introduced [82, 83]. These techniques enable maskless prototyping and production of small and medium numbers of devices, however, they are still suffering from drawbacks such as low resolution.

In constrast, femtosecond direct laser writing allows for the manufacturing of phase masks with unprecedented feature sizes in the sub-micrometer range [84, 9]. In this chapter we demonstrate the fabrication and characterization of diffractive optical elements directly attached to the end facet of optical fibers using femtosecond two-photon lithography.

Figure 4.1 illustrates such a phase plate consisting of different rings for beam intensity shaping directly attached to the end facet of an optical fiber.

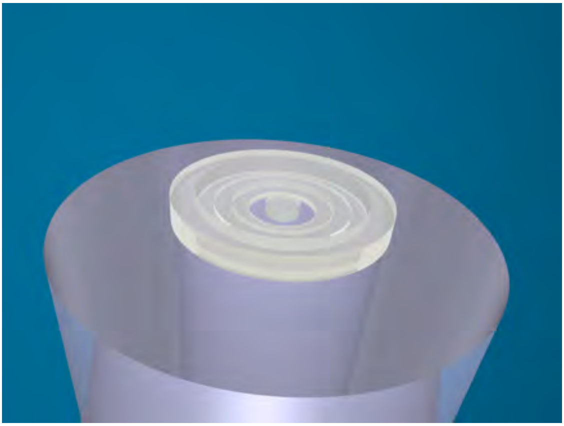

Figure 4.1. Illustration of a diffractive optical element directly attached to an optical fiber.

We measure for the first time the performance of such optics and demonstrate that we have sub-micrometer manufacturing accuracy. Specifically, we directly manufacture our optics on the tips of single-mode fibers, achieving sub-micrometer alignment accuracy during manufacture. No postfabrication positioning or alignment is necessary.

We give our printed optics different functionalities and demonstrate diffractive elements, which allow flat top illuminators or the generation of donut shaped light intensities. Our method extends the realm of additive optical manufacturing into micro- and nanooptics and opens a new field for integrated fiber optical or complex lab-on-a-chip devices.

In order to directly manufacture diffractive optical elements onto the end facet of optical fibers different approaches have recently been proposed. These are techniques such as interference lithography [85], photolithography [86], electron-beam lithography [87], and focused ion-beam milling [21]. Our method establishes a fast, simple, and straightforward fabrication alternative to the listed techniques with various advantages.

The combination of direct laser written phase plates with dielectric or metallic metasurfaces and other functional materials that are nonreciprocal or switchable, is possible. For this purpose, our sub-micrometer dielectric phase masks allow for the realization of the miniaturization of switchable high quality optical elements. This will enable a completely new generation of instruments, miniaturized microscopes, (fiber) sensors, light emitters, and beam shaping elements on the device level.

4.1 DONUT AND TOP HAT SHAPER

We demonstrate the generation of nontrivial intensity distributions by sub-micrometer diffractive optical elements. In particular, the emerged light of a single mode optical fiber is transferred into circular donut and tophat shaped intensity profiles.

The surface profiles of our phase masks are obtained by numerically solving the Huygens-Fresnel diffraction integral in two dimensions (see Chapter 3.2). In order to reach the target intensity distribution, the structures of the phase masks are stepwise improved by an iterative optimization algorithm [88], which is implemented in Matlab utilizing the rotational symmetry [76]. The refractive index of the exposed photoresist is assumed to be 1.513 for all simulations. The mode field diameter of our single mode optical fiber is 4.9 µm, which is obtained by mode theory with refractive indices of 1.4598 and 1.4537 for core and cladding material, respectively [71]. For the mode theory calculation a core diameter of the optical fiber of 4.4 µm is used. The radial integration range for solving the Huygens-Fresnel diffraction integral is determined to −6 to 6 µm, centered around the fiber core. The design wavelength is set to be 808 nm, corresponding to our laser source. The propagation distance between target and phase mask (fiber end face) is chosen to be 10 mm.

Every phase mask consists of five rings, where each ring has a width of 440 nm and is limited to a maximum height of 2 µm in simulation. As intensity distribution targets, donut and circular top hat shaped intensity distributions are chosen. The numerical simulation of the circular phase masks for the donut shaper results in surface relief heights of 785 nm, 793 nm, 805 nm, 868 nm, and 979 nm, beginning at the center. The top hat shaper is described by heights of 563 nm, 636 nm, 554 nm, 606 nm, and 613 nm.

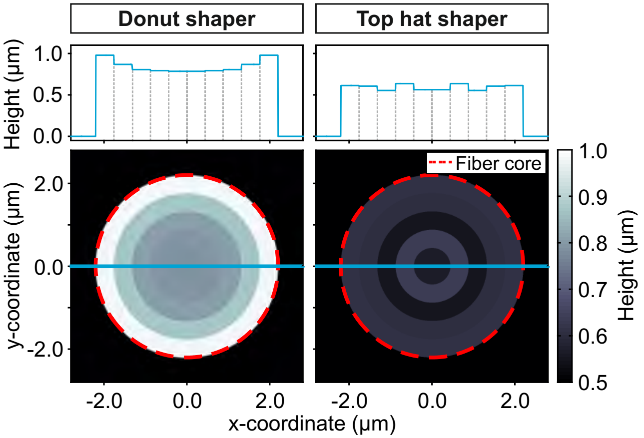

Figure 4.2. Diffractive donut and top hat intensity distribution shaper. Structure designs of diffractive optical elements for shaping a donut and top hat intensity distribution, respectively. Each structure consists of 5 rings with heights below 1 µm and widths of 440 nm.

Figure 4.2 shows the height profiles of the calculated phase masks for shaping a donut and a top hat intensity distribution, respectively. The target intensity distributions of the two beam shaping phase masks and the corresponding results of the simulations are shown in Fig. 4.3. The simulated beam profile deviates from the target as only a limited number of rings are used for discretization purposes to ease the final fabrication.

The simulated evolutions of the shaped intensity distribution as a function of the propagation distance are shown in Fig. 4.4. In both cases the desired target intensity profiles are formed in the first few millimeters behind the fiber end. Afterwards, the shaped intensity distributions propagate as known for beam propagation of optical single mode fibers as a divergent beam. The shaped intensity distributions are retained over the whole simulated propagation distance.

Two-photon polymerization allows for the fabrication of optical elements with feature sizes below 100 nm [45, 46]. There-

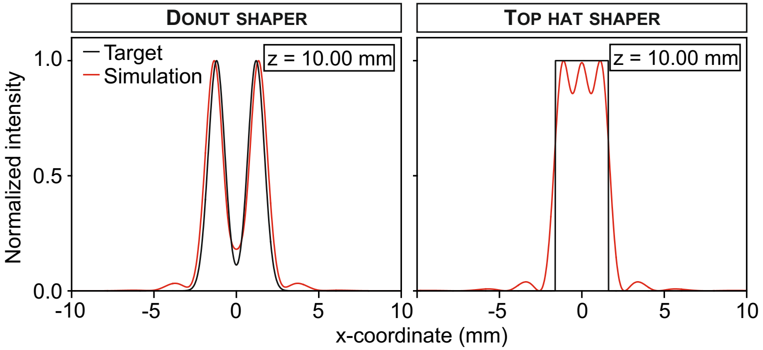

Figure 4.3. Simulations of the normalized intensity distribution of the donut and top hat shaping diffractive optical elements. Cross sections of the simulated intensity distribution of the donut shaped and the top hat shaped beam profile at a propagation distance z = 10 mm. Additionally, the target intensity distributions are shown. The intensity distribution at certain positions behind the surface is calculated by numerically solving the Huygens-Fresnel diffraction integral for a given diffractive optical element.

fore, this technique is perfectly suited for the fabrication of phase masks with feature size in the sub-micrometer range. The phase masks are directly manufactured onto the end facets of optical single mode fibers by the dip-in technique [64]. A droplet of the photoresist IP-Dip is deposited on the objective lens and subsequently, the fiber is dipped into this droplet of photoresist. During the fabrication process the laser is laterally moved via galvanometric mirrors. Ultra-precise piezo actuators execute the axial movement. For the fabrication optical single mode fiber pieces (SM 780HP, Thorlabs) with lengths of 15 to 20 cm are used.

The phase masks are fabricated ring-by-ring beginning at the center. Each 440 nm broad ring consists of five rings with the same height but different radii. By stacking numerous writing trajectories on top of each other every phase step is created. The layer-by-layer distance is 50 nm. Each circular trajectory consists of several points with 15 nm distance and begins at a random position on the circle in order that homogenous structures are created.

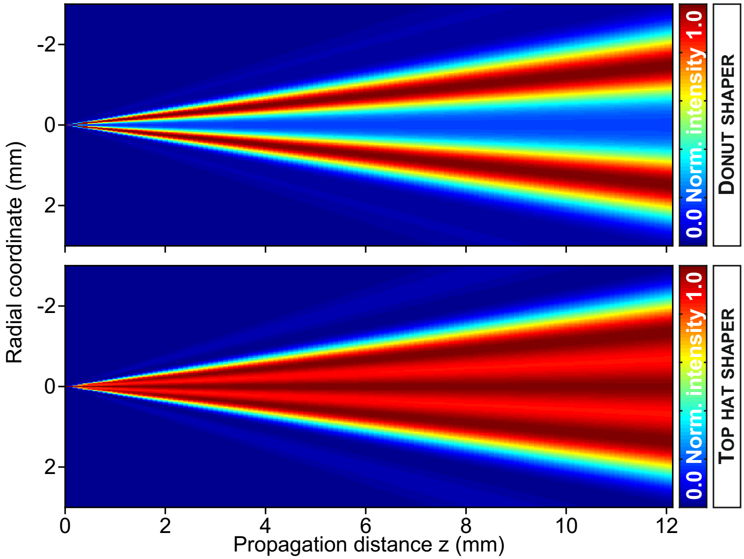

Figure 4.4. Simulations of the normalized intensity distribution of the donut and top hat shaping diffractive optical element. Simulations of the intensity distribution at different distances after the fiber end obtained by numerically solving the Huygens-Fresnel diffraction integral in two dimensions for the two different diffractive structure designs.

As it is quite challenging to locate the interface of the fiber end facet with an accuracy of a few tens of nanometers, a base with a height of 500 nm and a total diameter of 17.6 µm is fabricated beneath the phase mask. Figure 4.5 depicts scanning electron microscope images of a phase plate for beam intensity shaping directly attached to the end facet of an optical single mode fiber (SM 780HP, Thorlabs). The optical phase plate consists of a base and the diffractive element on top. The actual diffractive element has only a diameter of 4.4 µm and is precisely centered on the fiber core. Fig. 4.5b displays a detailed scanning electron image of the phase mask.

We characterize the written phase mask optically by coupling light of a laser diode with an operating wavelength of 808 nm (LP808-SF30, Thorlabs) into the fiber pieces. The emerged light is

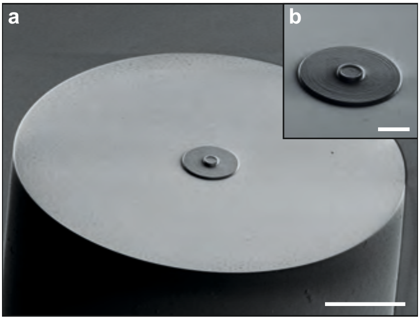

Figure 4.5. Scanning electron microscope image of a diffractive optical element for beam shaping application. a, The diffractive optical elements is attached to the end facet of an optical fiber and consists of 5 rings. The diffractive phase plate is fabricated ring-by-ring using three-dimensional direct laser writing. Scale bar, 25 µm. **b,** Zoom-in view of the phase mask sitting on a direct laser written base. Scale bar, 5 µm.

analyzed by taking pictures at several distances behind the fiber end with a CCD camera (GC 2450C, Allied Vision Technologies). Concerning this, the camera is moved with the help of a linear translation stage (PI miCos GmbH) in 250 µm steps. The absolute distance between fiber end and CCD chip is calibrated by comparing the measured profiles with the simulated ones.

Figure 4.6a shows the normalized intensity distribution of a donut shaping phase mask at a distance of 5 mm behind the fiber end. The emerged Gaussian intensity distribution of the single mode fiber is completely redistributed in order to form the beam profile within a few millimeters propagation distance. Additionally, the cross sections in x- and y-direction are depicted. Fig. 4.6b displays the intensity distribution of the top hat shaping phase mask with the corresponding cross sections. Both donut and top hat shaper exhibit high quality performance.

The corresponding normalized intensity distributions at a distance of 10 mm behind the fiber end facet are depict in Fig. 4.6c and d.

Figure 4.7a depicts the experimental results for the propagation of the intensity distribution behind the phase mask. The

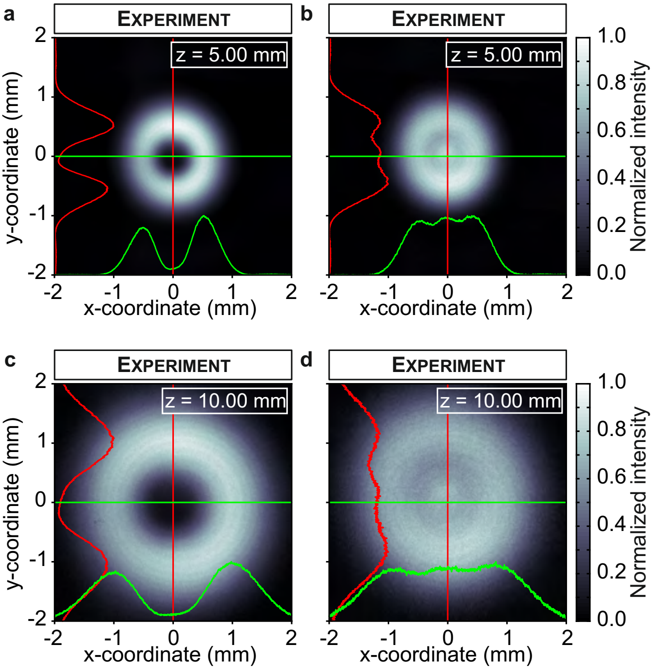

Figure 4.6. Measured intensity distribution for (a, c) the donut and (b, d) the top hat shaping diffractive optical element at distances of 5 mm and 10 mm behind the fiber end. The mode images are obtained by taking pictures with a CCD camera.

measured beam propagation of the donut shaping phase mask is in excellent agreement with the simulations in Fig. 4.4. At each z position of the evolution plot the beam profile is calculated as the average of the beam profile in x- and y-direction. The normalized intensity profiles of the cross sections at 4 mm, 8 mm, and 12 mm behind the fiber end, marked as positions A, B, and C, show excellent agreement with the simulations as well.

For comparison in Chapter C in the appendix the simulation and measurements of the pure single mode fiber SM 780HP without any optics are shown.

Fig. 4.7b shows the propagation of the intensity behind the top hat shaping phase mask. The two small dips in the mea-

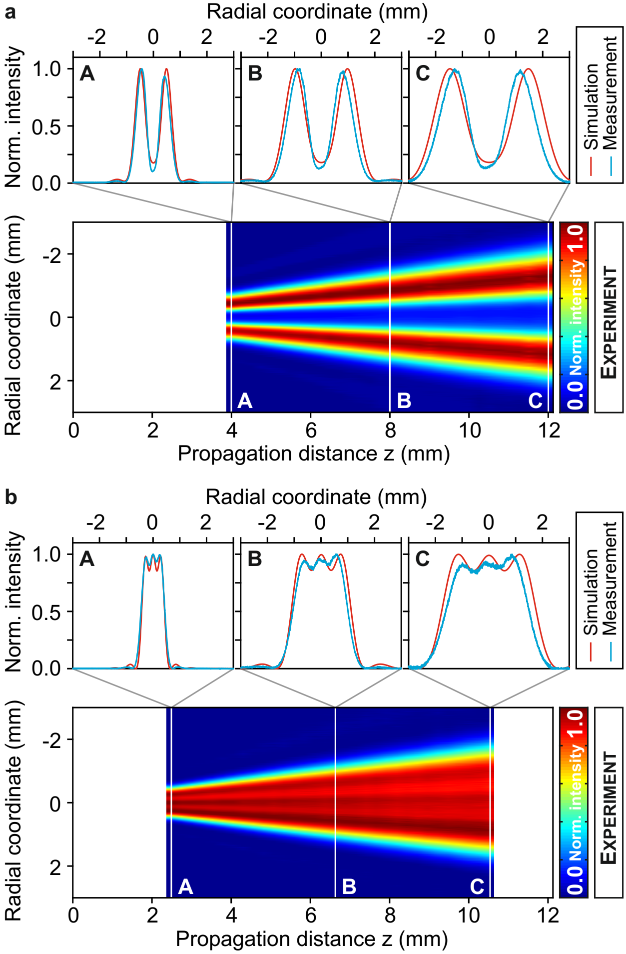

Figure 4.7. Measurement of the intensity distribution at different distances behind the fiber end for the donut and the top hat shaper. a, At each distances pictures of the mode are taken using a CCD camera. The cross section is obtained by taking the average of the cross section in x- and y-direction. At several positions the measurement is compared to the simulation. **b,** At each distances pictures of the modes are taken using a CCD camera. The cross section is obtained by taking the average of the cross section in x- and y-direction. At several positions the measurement is compared to the simulation.

sured intensity profiles can be seen in the simulated intensity distributions, too. There is again an excellent agreement between the measured and simulated intensity distributions, which can be seen in the cross sections at distances of 2.5 mm, 6.5 mm, and 10.25 mm marked as positions A, B, and C in the plots, as well.

The total degree of transmittance of phase masks on fibers with lengths of about 20 cm can reach up to 46.8 %. As the intensity shaping phase masks are directly fabricated onto the cores of optical fibers the alignment has to be tremendously accurate in order to obtain a highly symmetric intensity profile. Three-dimensional direct laser writing fabrication is well suited for the fabrication of these optical structures with feature sizes in the sub-micrometer range, which exhibit outstanding fabrication qualities. Our alignment procedure achieves positioning accuracy in the sub-micrometer range and thus allows for the beam shaping of the light emerging from a single mode fiber with a core diameter of only 4.4 µm (see Chapter 2).

We check the fabrication influences on the quality of the phase masks by fabricating phase masks on the one hand ring-by-ring as mentioned above and on the other hand layer-by-layer. The difference of the two fabrication methods can be seen in Fig. 4.8a and 4.8c. In Fig. 4.8a the phase mask is written ring-by-ring, whereas in Fig. 4.8c a layer-by-layer approach is used. The ring-by-ring fabrication method was introduced above, in the layer-by-layer fabrication method the diffractive element is fabricated by stacking several circular layers on each other. Fig. 4.8c shows that in the upper part the distances between the layer differ from each other in order to create the height profile of the mask, whereas in the lower part the layer are homogeneously separated by 50 nm.

As an example, we use the donut shaping diffractive element. The height profile is introduced above (see Fig. 4.2). Both fabrication methods result in high quality structures underlined by the virtually identical excellent optical performance of the two optics obtained from the different writing modes. The corresponding measurement results are depicted in Fig. 4.8b and 4.8d. The agreement between the elements of the two writing modes is excellent.

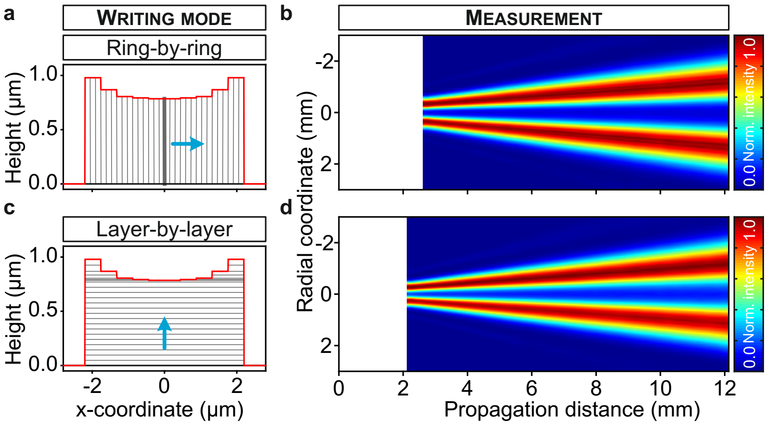

Figure 4.8. Comparison of different fabrication methods using three-dimensional direct laser writing. a, Fabrication schema of a diffractive optical element fabricated ring-by-ring. **b,** Measured intensity distribution at different distances behind the fiber end. **c,** Fabrication schema of a diffractive optical element fabricated layer-by-layer. **d,** Measured intensity distribution at different distances behind the fiber end.

In order to demonstrate the high reproducibility of this fabrication scheme, we fabricate phase masks with different numbers of rings. All of them are directly attached to the end facet of a single mode optical fiber and are designed to have the same target intensity distribution. We choose the donut shaped intensity distribution introduced in Fig. 4.3 as target profile.

The phase plates are fabricated in a two step procedure, in order to increase the quality even further. First the diffractive part of the phase plate is fabricated layer-by-layer and afterwards the base is fabricated. This procedure benefits from the fact that drifts of the fiber have nearly no influence.

Figure 4.9 depicts the different diffractive optical elements directly written onto an optical single mode fiber. The phase masks consist of four, five, and six rings and have a total diameter of 4.4 µm. Each ring is limited to a maximal height of 2 µm in simulation. As target a donut shaped intensity distribution is chosen. The numerical simulations of the circular phase masks consisting of four rings results in surface relief heights of 787 nm, 797 nm, 833 nm, and 970 nm beginning at the center (see Fig. 4.9, bottom). The heights of the phase plate with five rings are 785 nm, 793 nm, 805 nm, 868 nm, and 979 nm (see Fig. 4.9, middle) and for the six ring phase plate 680 nm, 666 nm, 663 nm, 720 nm, 622 nm, and 875 nm (see Fig. 4.9, top).

We find excellent agreement between the different measurements. This is also confirmed by the corresponding numerical calculations using Fresnel-Huygens diffraction. As they have different numbers of rings the phase mask profiles are quite different, a fact that again underlines the high fabrication quality and shape accuracy of the phase masks.

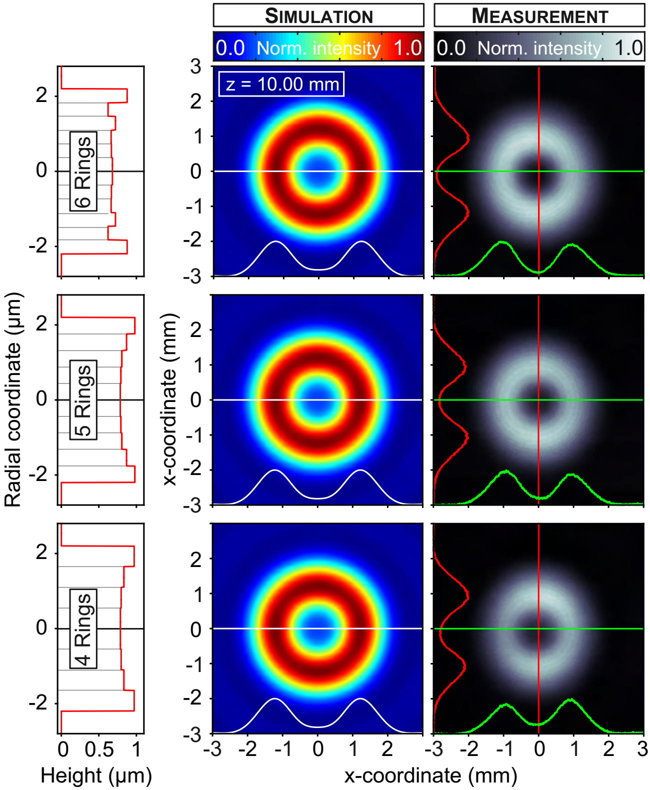

Figure 4.9. Comparison of the intensity distribution at a distance of 10 mm behind the fiber end for different number of diffractive rings. Structure designs of diffractive optical elements for shaping a donut with different numbers of rings. For each structure the Huygens-Fresnel diffraction integral is numerically solved in an iterative optimization algorithm in order to obtain the desired donut shaped intensity distribution.

4.2 SPECIAL BEAM SHAPING ELEMENTS

In addition, we analyzed different simpler diffractive optical elements consisting of simple steps or Siemens star like designs. These kind of phase plates can be of high interest for fiber optical sensors. Fiber sensors, which rely on transverse mode selection show tremendously larger sensitivities than sensors, which detect the whole light flux. Thus, diffractive optical elements directly fabricated on single mode fiber can be used for the registration of selected mode energies [89, 90, 91].

Moreover, these elements can be as well used for complex beam shaping and integrated optics.

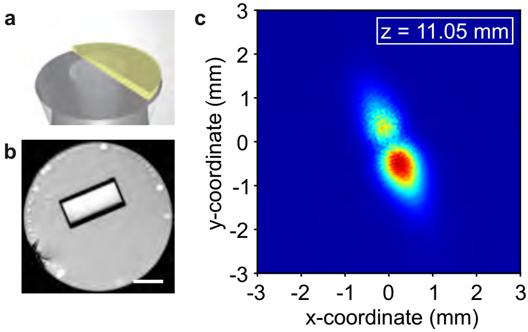

Figure 4.10. Diffractive optical element consisting of one single step on an optical single mode fiber SM 780HP. a, Illustration of the diffractive optical element. **b,** Microscope top view of the fabricated structure. Scale bar, 25 µm. **c,** Measurement result at a distance of $z = 11.05\,\mathrm{mm}$. The asymmetry is caused by a height, which does not correspond to a phase shift of π.

Figure 4.10 shows a diffractive optical element, which covers half of the core of an optical single mode fiber. This simple phase plate is designed to split the fundamental mode of the single mode fiber into two parts. The added phase shift caused by the dielectric, placed on one half of the fiber, is π. The simulation can be found in Fig. 4.11 and is confirmed by the measurement shown in Fig. 4.10c.

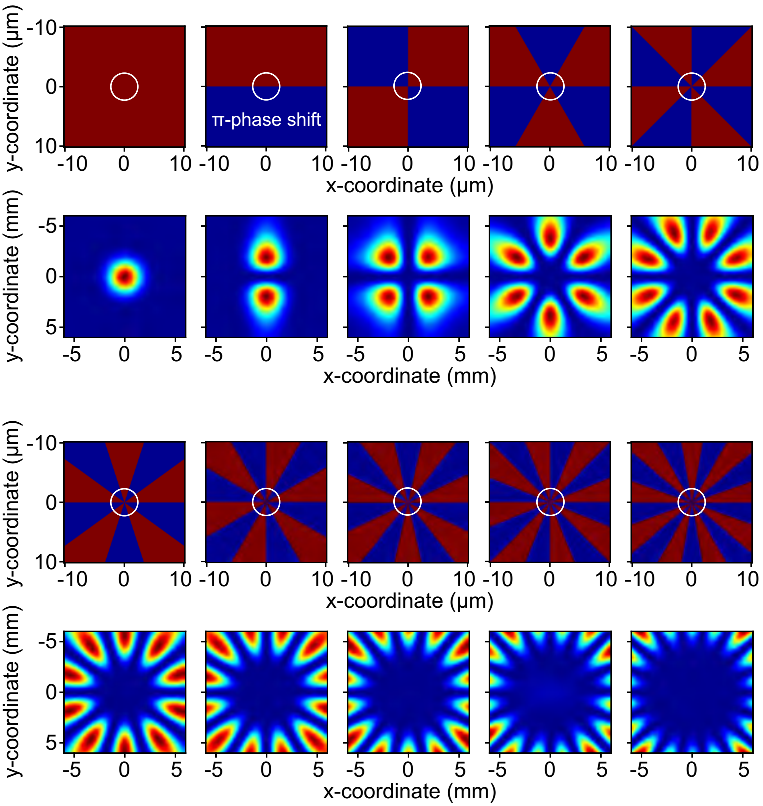

Figure 4.11. Simulation of different diffractive structures centered on an optical single mode fiber. In each case, in the upper row the structure and the lower row the intensity distribution is shown. The intensity distribution is calculated at a distance of 20 mm by numerically solving the Huygens-Fresnel diffraction integral in three dimensions. The white circle indicates the position of the fiber core, which has a diameter of 4.4 µm.

The simulations of the Siemens star shaped diffractive elements shown in Fig. 4.11 are inspired by the work of Gavrilov et al. and Salgado-Remacha [92, 93]. The simulated results are obtained by numerically solving the Huygens-Fresnel diffraction integral in three dimensions. In all simulations the refractive index of the photoresist is assumed to be 1.513. The simulations are carried out at a wavelength of 808 nm. The beam width at the end facet of the optical single mode fiber is 2.4 µm and is calculated by mode theory using 1.4598 and 1.4537 as refractive indices for cladding and core material. The core diameter of the fiber is 4.4 µm, which corresponds to the data of the single mode fiber 780HP.

In Row 1 and 3 of Fig. 4.11 the height profiles and therefore, consequently the phase shift profiles are shown. The white ring indicates the core of the optical single mode fiber. Row 2 and 4 show the simulation results of the intensity distribution at a distance of 20 mm in an area of $5 \times 5\,\mathrm{mm}^2$. The simulations show that the fundamental beam profile is divided into numerous parts, where the number is identical to the number of phase steps. Additionally the diameter of the complex intensity distribution increases with the number of steps. We simulate the influence of 0 to 18 steps, where the steps cause either a phase shift of 0 or a phase shift of π.

Figure 4.12 shows the measurements of different Siemens star like diffractive structures. Each structure is fabricated on the center of an optical singe mode fiber SM 780HP using dip-in direct laser writing. The structures is fabricated layer-by-layer by exposing the photoresist IP-Dip. Galvanometric mirrors move the laser focus over the end facet of the optical fiber.

The structure is manufactured by slicing the structure in lateral as well as in axial direction at a distances of $\leqslant$100 nm. The hatching angle between two layers is set to 90°. More details and the definition of slicing and hatching parameters can be found in Chapter D in the appendix.
The structure consists of a base with a height of 2 µm. The different steps are successively fabricated considering the symmetry.

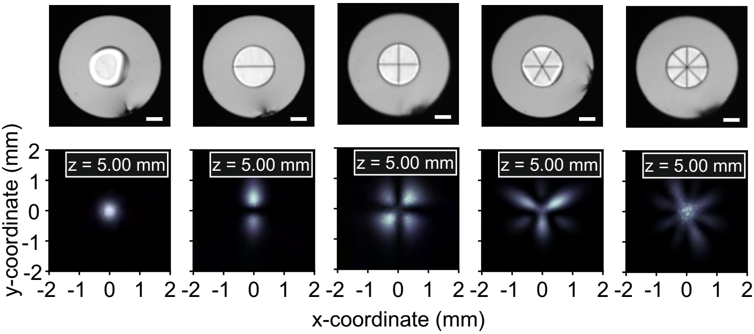

Figure 4.12. Measurement of different diffractive structures centered on an optical single mode fiber. The upper row shows microscope images of the fabricated structures. In the lower row the normalized intensity distribution are depicted. Scale bar, 20 µm.

This means that for each step one hatching direction is parallel to the radial direction. All steps have the same height d of

$$d = \frac{\lambda}{2} \frac{1}{n_{\text{photoresist}} - n_{\text{air}}}, \tag{4.1}$$

where λ is the wavelength of the light, which is 808 nm for the used laser diode. The refractive index of the photoresist is $n_{\text{photoresist}} = 1.513$ and the refractive index of air is 1. The step height d corresponds to a phase shift of π.

As shown in Fig. 4.12 the measurements (second row) show a good agreement with the simulation, depicted in Fig. 4.11. However, one needs to consider that the simulation does not contain any absorption. This means, there is an absorption difference caused by the different step height, which leads to a variation in the intensity distribution. Therefore, every second intensity peak is more pronounced in the image of the intensity distribution.
Additionally, there can be a deviation in step height, which causes as well an inhomogeneous intensity distribution, as shown below. Figure 4.13 shows the influence of the step height and thus the phase shift. We simulated the transition from a phase shift of 0 to a phase shift of π in 5 steps. Whereas in the upper row of Fig. 4.13, the phase profile is shown, the lower

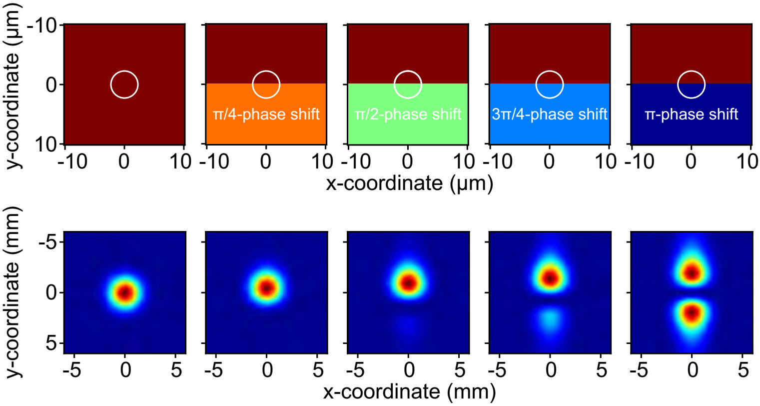

Figure 4.13. Simulation of different phase shifts centered on an optical single mode fiber. In each case, in the upper row the structure and the lower row the intensity distribution is shown. The intensity distribution is calculated at a distance of 20 mm by numerically solving the Huygens-Fresnel diffraction integral in three dimensions. The white circle indicates the position of the fiber core, which has a diameter of 4.4 µm.

row depicts the simulations results. While 0-phase shift and π-phase shift cause a symmetric intensity distribution, the shifts in-between create asymmetric beam profiles. There is a transition from the fundamental mode to a intensity distribution, which consists of two peaks.

In Fig. 4.14 the simulations for not perfectly centered phase masks are shown. The edge of a π-phase shift is moved over the core of an optical single mode fiber in 5 steps. Again, the upper row shows the phase shifts, whereas the lower part of Fig. 4.14 shows the simulated intensity distribution. At each position the intensity distribution is symmetric.

From these results we can conclude that the asymmetry in the intensity profile in Fig. 4.10c of our fabricated phase mask is not just caused by a misalignment but as well by a variation in the step height, which does not correspond to a phase shift of π. Therefore, the base which we usually fabricate beneath our phase mask is absolutely essential, as the interface of the fiber end facet

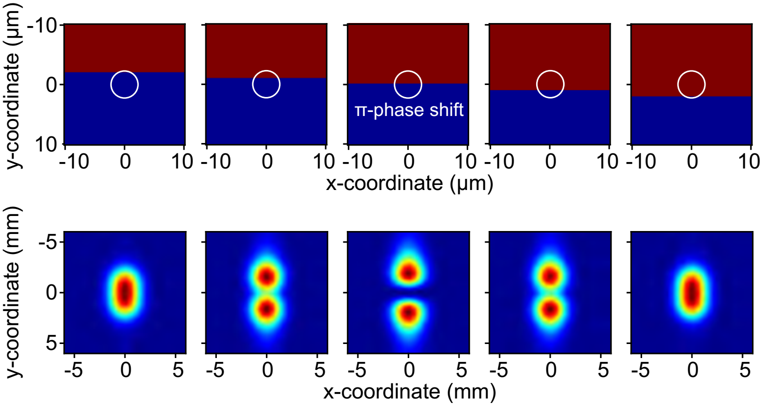

Figure 4.14. Simulation of a π-phase shift at different positions on an optical single mode fiber. In each case, in the upper row the structure and the lower row the intensity distribution is shown. The intensity distribution is calculated at a distance of 20 mm by numerically solving the Huygens-Fresnel diffraction integral in three dimensions. The white circle indicates the position of the fiber core, which has a diameter of 4.4 μm.

cannot be found with the required accuracy. In addition, there is absorption in the photoresists, which increase the effect of the mismatch (see Fig. 4.12).

5

PHOTONIC CRYSTALS

Periodic dielectric structures can influence the polarization state of light in the optical wavelength regime [94, 55, 95, 56]. In combination with fiber optics we select specific circular polarization states in the telecomunication wavelength region directly at the end facet of an optical single mode fiber.

Wavelength separation and polarization control are achieved by using a chiral polymer photonic crystal structure schematically shown in Fig. 5.1a. The structure design is inspired by chiral nematic liquid crystals. In the cholestric mesophase the liquid crystals are ordered in layers, where in each layer there is an order in the direction of the molecules [96]. For our chiral polymer photonic crystal structure this means that there are parallel rods or wires in a first layer. A second identical layer is stacked on top of the first one, but rotated by an angle of 360°/N. By placing several rod layers on each other the crystal is formed.

The individual layers can be stacked clockwise or counterclockwise and thus build two different symmetries with respect to the substrate: A left-handed and a right-handed chiral structure. Due to the appearance of the structure, it can be regarded as a ″twisted woodpile″.

The design of such chiral photonic crystals leads to photonic band gap effects, which cause stop bands dependent on the incoming polarizations state. According to the circular polarization state of the light and the handedness of the structure the transmission is suppressed for a certain wavelength. Therefore, this structure filters polarization states and can be used to generate circular polarized light, where the polarization state and the wavelength range can be controlled by the structure parameters.

By using the photoresist IP-Dip we directly fabricated the chiral polymer photonic crystal structure on the end facet of an optical single mode fiber SMF-28 (Newport). The twisted woodpile in Fig. 5.1b is designed to have the polarization stop band at the

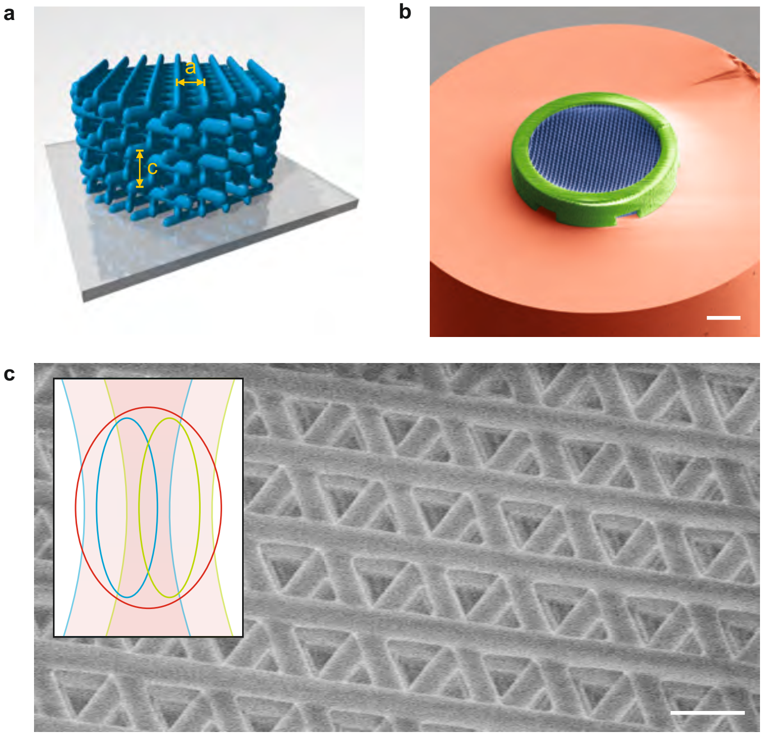

Figure 5.1. Chiral photonic crystal for polarization control directly fabricated on an optical fiber tip. a, Illustration of a ”twisted woodpile” structure. **b,** Colored scanning electron microscope image of the fabricated left-handed structure (blue) containing a solid ring (green) in order to increase the stability and reduce deformation of the structure. Scale bar, 10 µm. **c,** Detailed view of left-handed chiral photonic crystal. The inset illustrates the superposition of two individual exposure processes, which lead to a reduction of the rod aspect ratio. Scale bar, 1 µm.

telecommunications wavelength at 1.55 µm. In the design we use a rotation angle of 120° between neighboring layers, which corresponds to N = 3. Thus, every fourth layer is identically oriented. A rod-by-rod distance a of 1.25 µm and a layer-by-layer distance of 0.44 µm are used. This corresponds to a lattice constant c of 1.32 µm. In order to overcome the ellipticity of one single rod, every rod consists of two similar written lines spaced by a distance of 100 nm.

Figure 5.1b depicts a scanning electron microscope image of a left-handed structure (blue) containing a solid ring (green) in order to increase the stability and reduce deformation of the structure. The structure is directly fabricated on the end facet of a single mode fiber, centered on the fiber core with an alignment accuracy in the sub-micrometer range.

Figure 5.1c shows a detailed view of the chiral photonic crystal structure. The wires are homogeneously arranged over the whole structured area. The superposition of two wire results in a rod thickness of around 240 nm.

We obtain high resolution as visible in the scanning electron microscope image (Fig. 5.1c) of a left handed structure that exhibit good homogeneity. Note that the requirements for this kind of structure are completely different than for the refractive optics (Chapter 6 and Chapter 7), however, the fabrication process is the same in both cases.

The optical characteristics are displayed in Fig. 5.2a and 5.2b for the left-handed and right-handed structure. Around the design wavelength of 1550 nm, the devices exhibit circular polarization selectivity with a bandwidth of roughly 50 nm. Additionally, we study the influence of having the photonic crystal structure at the input and at the output coupling facet, which is negligible. As a reference, an unstructured single mode fiber with the same length (17.5 cm) is used. Due to slightly different fiber lengths and in-coupling efficiencies between sample and reference, the absolute values are not exactly calibrated, whereas the spectral shape corresponds to similar structures on glass [55].

For the polarization control measurement the incident light from a white light source (Energetiq EQ-99 LDLS) is circularly polarized by a Glan-Thompson polarizing prism (Bernhard Halle

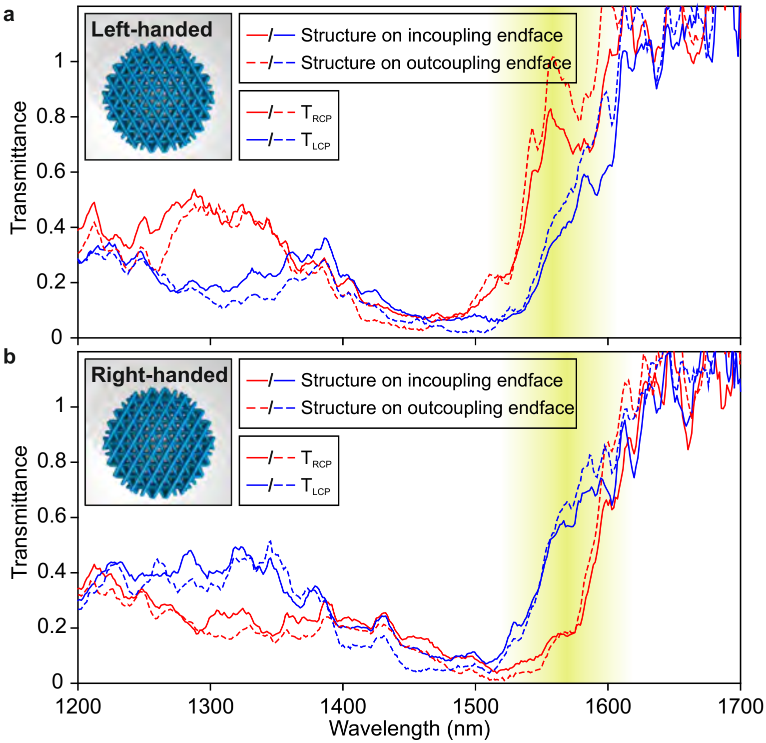

Figure 5.2. Chiral photonic crystal for polarization control directly fabricated on an optical fiber tip. a, b, Measured transmittance spectra for right- and left-handed circularly polarized light for the chiral photonic crystal at the in-/out-coupling end facet of an optical fiber and for the left- (**a**) and right-handed (**b**) photonic crystal structure, respectively. The design wavelength for the polarization filter was 1550 nm.

Nachfl.) in combination with a broadband achromatic quarter wave plate (Bernhard Halle). A 10x- and a 6.3x-objective are used for the input and the output coupling, respectively. The transmittance spectra are measured by using an optical spectrum analyzer (Ando AQ6315E) with a sensitive region ranging from 350 nm to 1750 nm.

6

REFRACTIVE OPTICAL ELEMENTS

Micro-optics are widely used in numerous fields of application such as beam shaping in terms of collimation and focusing as well as imaging purposes. Among the relative small size of the system the optical performance is crucial. Usually, micro lenses consist of one flat plane and one spherical surface.

In order to fabricate small and simultaneously well performing micro-optical systems, so far a large number of different fabrication methods exist. Refractive micro lenses are fabricated by diamond milling [19], femtosecond two-photon photopolymerization [97], gray-scale lithography [15], imprint lithography using soft or hard stamps [98], injection molding [12], modified LIGA processes [11], photoresist reflow [10], simple ink-jet printing techniques [18, 13, 99], two-mask processes [100], and wafer level packaging technology [20].
However, these technologies suffer from drawbacks such as limited miniaturization, lack of combining multiple elements, restriction in designing the surfaces [10, 11, 12, 18], and problems in the alignment [19].

In this chapter, 3D printed refractive micro- and nano-optics, fabricated by femtosecond two-photon direct laser writing are introduced. We show the performance of these optics and demonstrate that we reach sub-micrometer manufacturing accuracy, down to the level of about one optical wavelength, which is equivalent to other low-cost optics. Specifically, we directly manufacture our optics on the tips of single-mode fibers, achieving sub-micrometer alignment accuracy directly at manufacturing. No postfabrication positioning or alignment is necessary.

We combine our printed optics with different functionalities and demonstrate free-form optics, which allow for flat top illuminators or the generation of doughnut shaped light intensities.

Figure 6.1 shows a photograph of a sub-micrometer optical device attached to the end facet of an optical fiber. For this purpose,

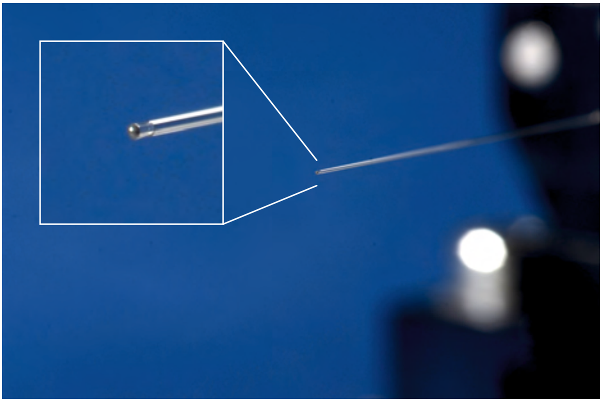

Figure 6.1. Sub-micrometer optical device attached to the end facet of an optical fiber. Macro photograph of a lens which has a diameter of 140 µm and a height (lens thickness) of 250 µm. The lens is entirely fabricated out of a dielectric transparent photoresist.

the lens is directly fabricated on the end facet. The dielectric photoresist shows high transparency and is thus perfectly suited for manufacture high-quality optical elements.

Using this technique we show different applications of sub-micrometer optical components for beam collimation, generation or correction of astigmatism, and beam shaping. This allows the specific shaping of the intensity distribution directly at the output of an optical fiber by refractive elements.

6.1 SPHERICAL LENS - BEAM COLLIMATOR

In using a spherical surface we show the collimation of the beam emerging from an optical fiber.

For the simulation of spherical lenses Gaussian beam propagation with an ABCD matrix formalism is implemented in Matlab (see Section 3.1). The lenses consist of a spherical refractive surface with its apex at a distance D behind the end facet of an optical single mode fiber (SMF). The distance D can also be seen as the lens thickness. A schematic drawing of a spherical lens is shown in the inset of Fig. 6.2. In order to achieve a collimated laser beam using a spherical lens attached to a single mode fiber, we optimize the radii of curvature (ROCs) for different lens thicknesses D by minimizing the beam width w at a distance z of 20 mm after the fiber end facet.

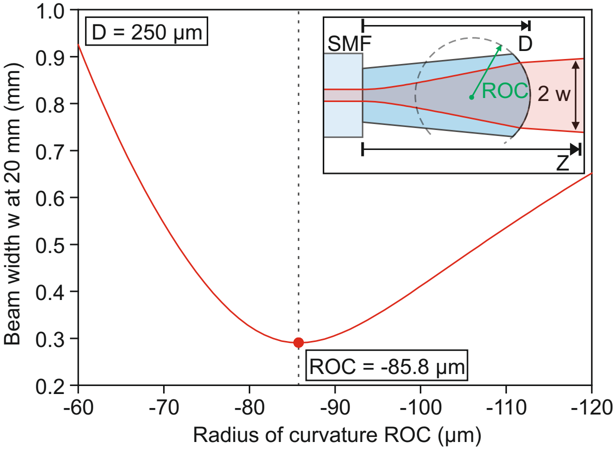

Figure 6.2. Simulation of the radius of curvature (ROC) for a 250 µm thick spherical lens. The ROC is varied while the beam width (radius of intensity at $1/e^2$) at a distance of 20 mm is analyzed. A minimal beam width is obtained for a ROC of −85.8 µm. As an inset a schematic drawing of a spherical lens attached to a single mode fiber (SMF) is shown.

Figure 6.2 shows the beam width (radius of intensity at $1/e^2$) of a 250 µm thick spherical lens for different ROCs. By varying the ROC and observing the beam width in simulation a minimal beam width is obtained for a ROC of −85.8 µm.

The simulations are carried out using a refractive index of 1.513 for the lens material, which is also confirmed by refractive index measurements in Chapter A. The beam waist at the end facet of the single mode fiber is 2.45 µm, which is determined by mode theory using 1.4598 and 1.4537 as refractive indices of core and cladding material, respectively [71]. The core diameter is 4.4 µm. All simulations are carried out at a wavelength of 800 nm, which corresponds to our laser source.

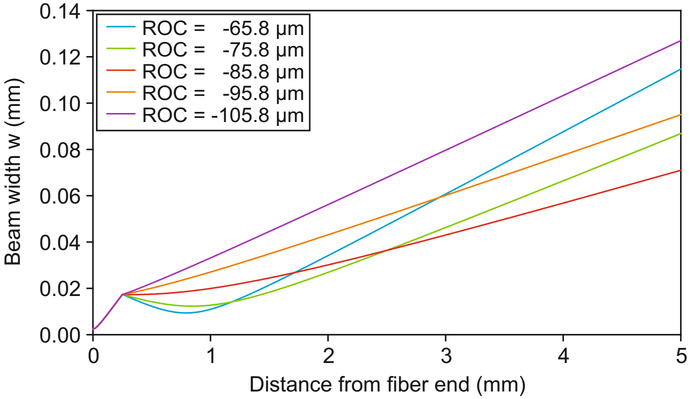

Figure 6.3. Radius of curvature variation for a 250 µm thick spherical lens. The ROC is varied in 5 steps around the optimized ROC value of −85.8 µm.

The beam width w is strongly dependent on the ROC (see Fig. 6.2). Gaussian beam propagation simulations show that small ROCs cause focuses within a few millimeters of the propagation distance and therefore, the beam becomes strongly divergent far away from the optic. Low curvatures do not focus the beam and thus the beam as well strongly diverges. By showing the beam width of a 250 µm thick spherical lenses with different ROC values of −65.8 µm, −75.8 µm, −85.8 µm, −95.8 µm, and −105.8 µm this behavior is depicted in Fig. 6.3. For the red line, which corresponds to a ROC value of −85.8 µm the beam width at a distance of 5 mm is minimal and therefore, the best collimation at this distance is reached. Stronger or weaker focusing leads to larger beam width at 5 mm distance. Therefore, there is an optimum in the ROC value, for which the beam width becomes minimal. In the case of a 250 µm thick lens the optimal ROC is −85.8 µm for a optimization distance of 20 mm.

Figure 6.4 shows the optimal ROCs for different lens thicknesses D in order to get a minimal beam width at a distance of 20 mm. For thin lenses the ROC has to have a strong curvature and thus a small ROC in order to get a sufficient collimation. In order to achieve a collimated laser beam with mini-

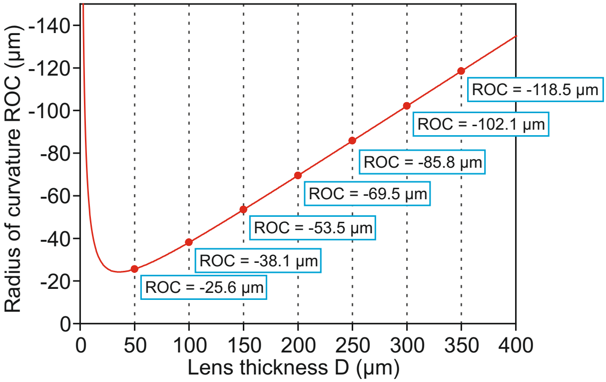

Figure 6.4. Radius of curvature (ROC) variation for different spherical lenses. The simulated ROCs are −25.6 µm, −38.1 µm, −53.5 µm, −69.5 µm, −85.8 µm, −102.1 µm, and −118.5 µm for lens thicknesses D of 50 µm, 100 µm, 150 µm, 200 µm, 250 µm, 300 µm, and 350 µm, respectively.

mal beam width, a certain lens thickness is required typically in the $\geqslant$100 µm range. Otherwise the lateral extent of the Gaussian beam is not large enough to obtain good collimation of the beam by a single refractive element [8, 41].

For lens thicknesses D of 50 µm, 100 µm, 150 µm, 200 µm, 250 µm, 300 µm, and 350 µm the simulated radii of curvature are −25.6 µm, −38.1 µm, −53.5 µm, −69.5 µm, −85.8 µm, −102.1 µm, and −118.5 µm. As one can see in Fig. 6.4 the ROC is proportional to the lens thickness for thick lenses.

In order to measure the intensity distribution of the beam profile at different distances, light from a single mode fiber-coupled laser diode with a wavelength of 808 nm (LP808-SF30, Thorlabs) is coupled into the unstructured end facet of the fiber. At several distances pictures of the mode emerging from the opposite facet are taken using a CCD camera (GC 2450C, Allied Vision Technologies). The camera is moved by a linear translation stage (PI miCos GmbH, Germany). The beam width is taken as the radius, where the intensity has decreased to $1/e^2$. A schematically illustration of the measurement setup is shown in Fig. 6.5.

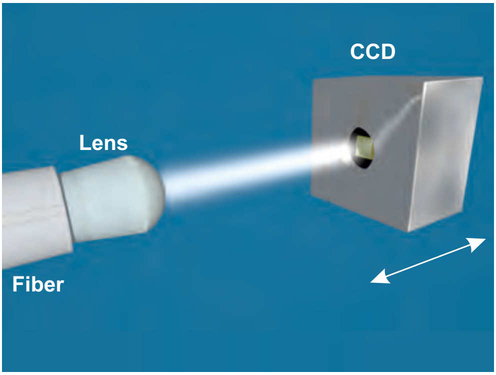

Figure 6.5. Setup for measuring the spherical lenses. Schematic drawing of the measurement setup. A CCD camera is moved with respect to micro-optical lens system by a linear translation stage. At each position an image of the intensity distribution is taken.

We experimentally demonstrate in Fig. 6.6 the collimation of a Gaussian beam emerging from a single mode optical fiber (SM 780HP, NA = 0.13). Our lenses are directly fabricated on the end facet of the fibers. Spherical lenses with different radii of curvature (ROCs) and thicknesses D are produced.

Figure 6.6 depicts the propagation of the beam waist of the initial fiber and six different lenses with thicknesses varying from 50 µm to 300 µm and ROCs from −25.6 µm to −102.1 µm. The plots display the designed beam waist calculated using Gaussian beam propagation, and red and blue dots denote the measured beam waist radii w_x and w_y at distance z from the fiber end, respectively. The agreement is excellent. The collimation improves with increasing lens thickness, which is also verified by the simulations using the ABCD matrix formalism algorithm. These are summarized in Fig. 6.7, where the measured and simulated beam width at a distance of 20 mm is plotted over the lens thickness D. Fig. 6.7 shows that a certain lens thickness ($\geqslant$100 µm) is necessary in order to sufficiently collimate the emerging beam of a single mode fiber. Good agreement is obtained between measurement and simulation. The excellent performance of the printed lenses is as well confirmed by the Gaussian-shaped lateral beam profile

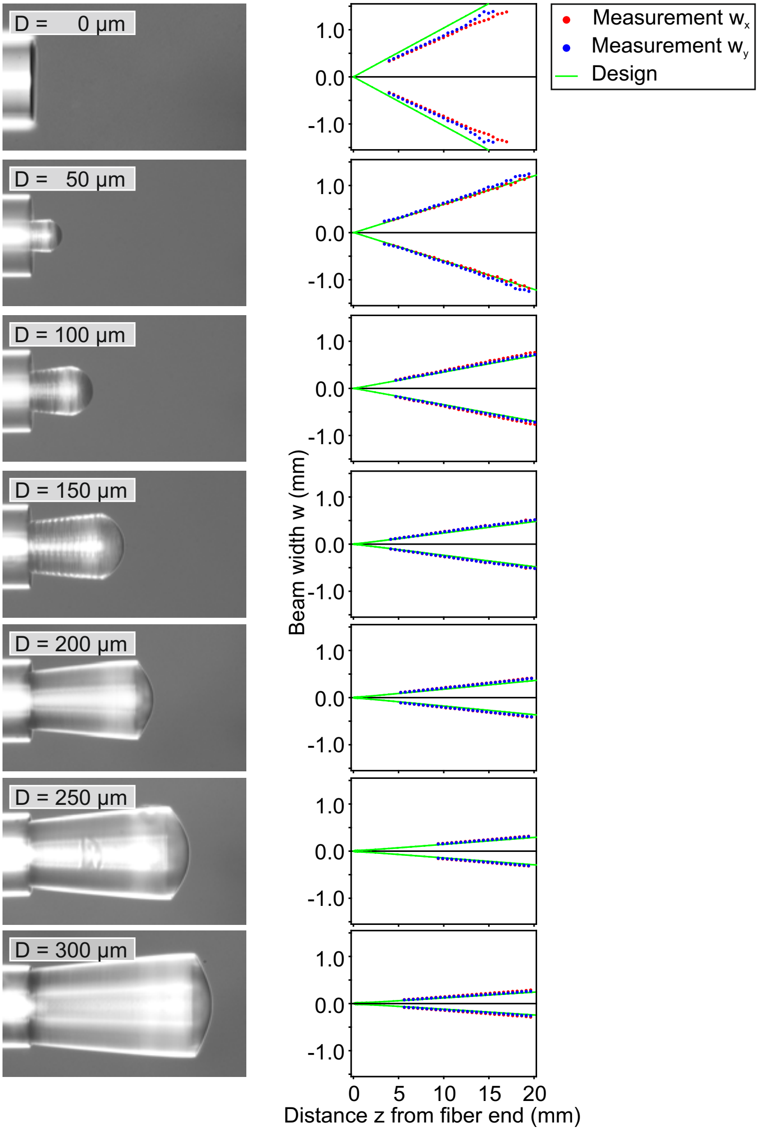

Figure 6.6. Characterization of a spherical lens for the collimation of a Gaussian beam.

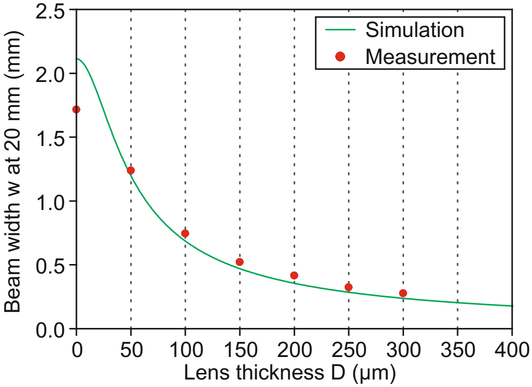

Figure 6.7. Measurement and simulation of different spherical lenses. Beam width for different lenses taken at a distance of 20 mm after the fiber end facet and the comparison with the simulation obtained by Gaussian beam propagation with an ABCD matrix formalism. The ROCs are −25.6 µm, −38.1 µm, −53.5 µm, −69.5 µm, −85.8 µm, and −102.1 µm for lens thicknesses D of 50 µm, 100 µm, 150 µm, 200 µm, 250 µm, and 300 µm, respectively.

measured for a 300 µm thick lens with a ROC of −102.1 µm at a distance of 10 mm after the fiber end (Fig. 6.8).
At a distance of 10 mm an image of the intensity distribution is taken. The profiles in x- and y-direction are compared to a Gaussian profile and excellent agreement is observed. The lateral beam profile in Fig. 6.8 proves that our refractive surface are of high optical quality, as the Gaussian beam profile is not disturbed.

As our structures possess strong curvatures within a small area and additionally small features sizes, characterization methods of the topography are very restricted. However, optical interferometry measurements validate the high quality of the fabricated lenses, although our structures are challenging for this kind of measurement method. In Fig. 6.9a the topography of a lens with a thickness D of 250 µm and a ROC of −85.8 µm is shown.

In order to manufacture the complete optical element with a homogenous refractive index, each lens is fabricated with a con-

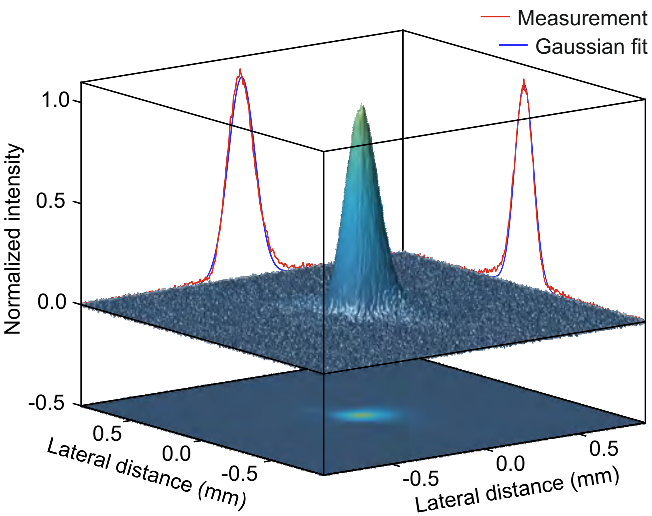

Figure 6.8. Beam profile of a 300 µm thick spherical lens. Intensity distribution of the beam profile at a distance of 10 mm measured from the optical fiber using a lens thickness D of 300 µm.

stant distance between the writing layers of 200 nm. The layer-by-layer fabrication process is not visible as the photoresist forms a smooth surface, which makes this fabrication method excellently suited for this kind of optical elements. In order to accelerate fabrication, we used 800 nm writing distance and higher writing power in the lower part of the lenses. The deformation during the exposure process and the development causes small deviations between the designed and the measured surface (Fig. 6.9b), which are below ±1 µm. This implies a maximal surface tolerance of roughly one wavelength for the designed wavelength of 800 nm, which is our design wavelength. Atomic force microscopy measurements result in 43 nm rms (root mean square) surface roughness for lenses fabricated with a layer-by-layer distance of 400 nm. This is as well confirmed by optical white light interferometry measurements. Flat films even exhibits a surface roughness of below 10 nm rms. According to our experience, the shrinkage or deformation of such "bulky" objects consisting of layer-by-layer written is not uniform, as it depends on too many

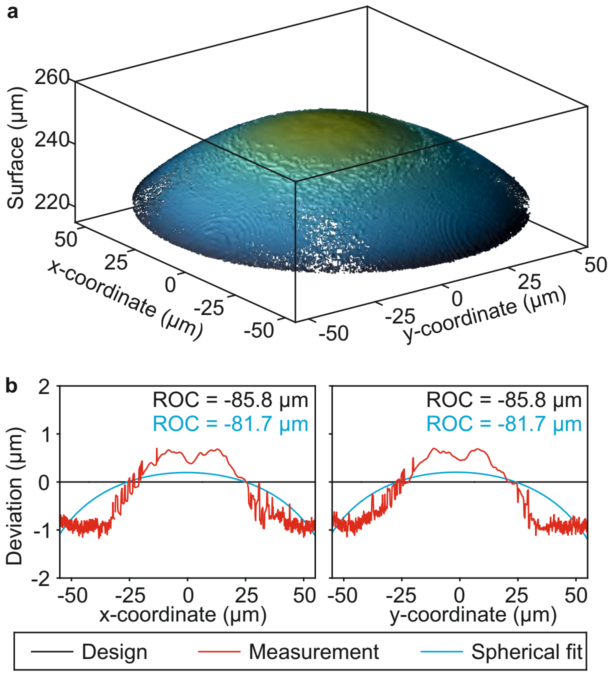

Figure 6.9. Characterization of the topography of a spherical lens. a, Measurement of the topography using optical interferometry of a spherical lens with a lens thickness D of 250 µm and a designed radius of curvature of −85.8 µm. **b,** Deviation of the measured surface topography, which is well below ±1 µm. The blue line describes a spherical fit to the surface. The fitted radius of curvature is −81.7 µm.

parameters, such as the photosensitive material, the writing parameters, and the shape itself. Therefore, a prediction of the deformation is still difficult to make, especially for complex surfaces. However, the smooth surfaces and the high quality of the photoresists make it possible to reach total transmittance of up to nearly 70 % for fiber pieces of up to 20 cm at a wavelength of 808 nm including the input and output coupling losses.

6.2 CYLINDRICAL LENS

As shown before, Gaussian profiles of a beam of light are maintained when they are refracted by spherical lenses. In order to transform Gaussian beam profiles more complex surfaces have to be used. Cylindrical lenses only focus light in one direction, thus the Gaussian beam profile is laterally compressed along one axis, whereas the profile in the perpendicular direction stays unchanged.

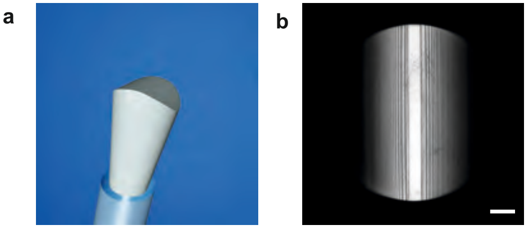

Figure 6.10. Cylindrical lens directly attached to an optical fiber tip. a, Schematic illustration of a cylindrical lens, which focus light into a line. **b,** Microscope top view of a cylindrical lens with a radius of curvature (ROC) of −75.1 µm in the x-direction and a thickness of 250 µm. Scale bar, 20 µm.

Cylindrical lenses have a cylindrical surface with a circular cross section in one direction and a flat cross section in the perpendicular direction. Fig. 6.10a shows an illustration of such a lens. The curvature along one axis focuses light into a point, whereas the flat cross section does not influence the light. Therefore, cylindrical lenses can be used for the generation of line focuses. Additionally, non-uniform stretching of images can be achieved, as cylindrical lenses focuses light only in one direction.

Figure 6.10b shows a microscope top view of a lens with a radius of curvature (ROC) of −75.1 µm in x-direction. The lens is directly fabricated on the end facet of a single mode fiber by direct laser writing. The lens consist of the dielectric photoresist Ormocomp and is fabricated layer-by-layer. The lower part of the structure is exposed with a layer distance of 800 nm and thus higher power values. In the upper part, which contains the curvature, the layer-to-layer distance is 200 nm. The lens has a thickness of 250 µm and a diameter of 120 µm. For the fabrication the fiber is moved with respect to the laser focus by ultra-precise piezo actuators.

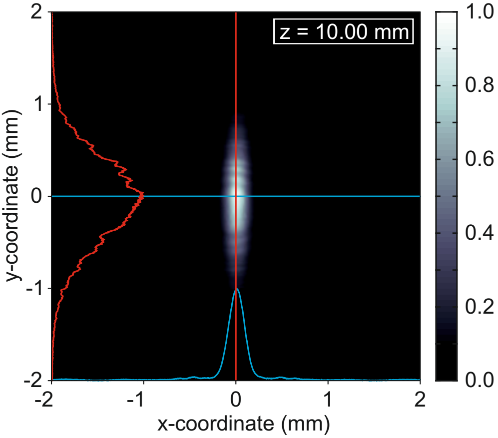

Figure 6.11. Measured intensity distribution of a cylindrical lens with a radius of curvature (ROC) of −85.8 µm and a thickness of 250 µm. The mode image is obtained by taking a picture at a distance of 10 mm behind the fiber end facet with a CCD camera. Additionally, the cross sections in x- and y-direction are plotted

Figure 6.11 shows the measured intensity distribution of a cylindrical lens directly attached to an optical single mode fiber at a distance of 10 mm behind the end facet of the fiber. The lens has a ROC of −85.8 µm and generates a line focus along the y-coordinate with a broad Gaussian beam profile. In x-direction the beam has a narrowed Gaussian profile. The lens is fabricated using the same parameters as the lens in Fig. 6.10b.

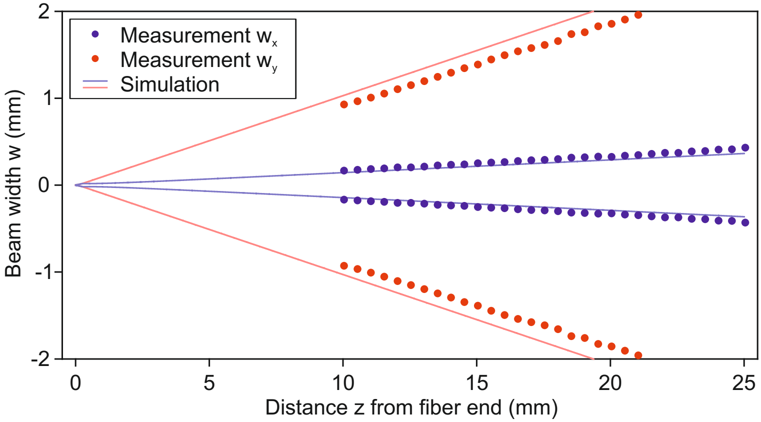

Figure 6.12. Characterization of a cylindrical lens with a radius of curvature (ROC) of −85.8 µm. Propagation measurements and simulations of the beam width w (radius of intensity at $1/e^2$). The lens thickness is 250 µm.

Figure 6.12 depicts the measured and simulated beam with respect to the propagation distance z measured from the fiber end. At each position an image of the intensity distribution is taken and the beam width at an intensity value of $1/e^2$ is determined. The measurements are in agreement with the simulation. As shown in the figure the beam profile in x-direction is not focused, but narrowed, where as in y-direction it propagates divergent, as if there is no lens on top. Therefore, a line focus is created.

For the simulations the Gaussian beam propagation with an ABCD matrix formalism introduced in Chapter 3.1 is used. The simulation parameters can be found in Section 6.1.

6.3 TORIC LENS

In order to generate or correct astigmatism, toric lenses are usually the tool of choice. The surfaces of these lenses consist of the upper part of a torus with two different radii of curvature (ROCs) along the x- and the y-direction (Fig. 6.13).

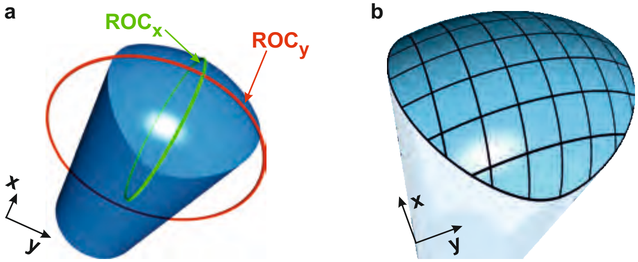

Figure 6.13. Illustration of a toric lens, which exhibits two different radii of curvature along the x- and the y-coordinate. The surfaces of toric lenses consist of the upper part of a torus. **a,** Schematic drawing of a toric lens with two radii ROC$_x$ in x-dircetion and ROC$_y$ along the y-axis. **b,** Illustration of a toric lens, which we fabricate by using direct laser writing.

For this purpose, the focal length in the x-plane differs from the focal length in the y-plane, which leads to a transition from an elliptical beam profile with the long axis in x-direction, to a circular beam profile to an elliptical beam profile with the long axis in the y-direction. Fig. 6.14 shows an illustration of the transition. The strong curvature in the x-plane causes a short focal length, whereas the large radius of curvature in the y-plane results in a long focal length. This behavior is connected to the transition in the intensity distribution.

Fig. 6.15 shows the measured non-rotationally symmetric topography of a toric lens directly fabricated on a single mode fiber. The topography is obtained by optical white light interferometry. The toric lens has a ROC of $-75.8\,\mu m$ in x-direction and a ROC of $-95.8\,\mu m$ in y-direction, respectively. The white light interferometer measurement shows a homogenous surface without any disturbances or defects. Although the structure is fabricated layer-by-layer no steps in the surface can be observed.

The two different curvatures cause different focal lengths in x- and y-direction, which result in intersecting beam waists, displayed in Fig. 6.14 and Fig. 6.16a. Figure 6.16a shows the mea-

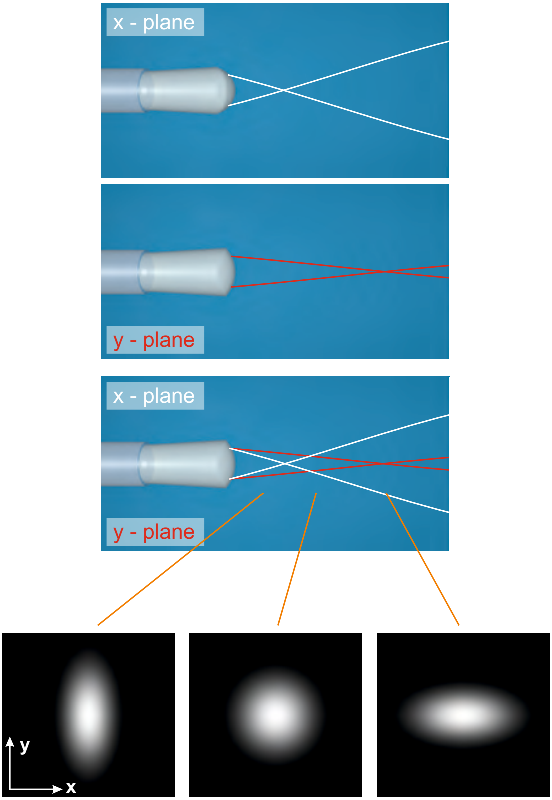

Figure 6.14. Illustration of a toric lens which exhibits two different radii of curvature along the x- and the y-coordinate. In the x-plane the lens features a strong curvature (small radius of curvature) and therefore, a short focal length. In the perpendicular plane (y-plane) the radius of curvature (ROC) is larger (slight curvature) and thus the focus is further away from the apex of the toric lens. All in all, this leads to a transition of the two-dimensional intensity distribution. At the beginning there is an elliptical distribution with the long axis along the x-axis, which is transferred to a circular intensity distribution to in the end an elliptical distribution with the long axis along the y-axis.

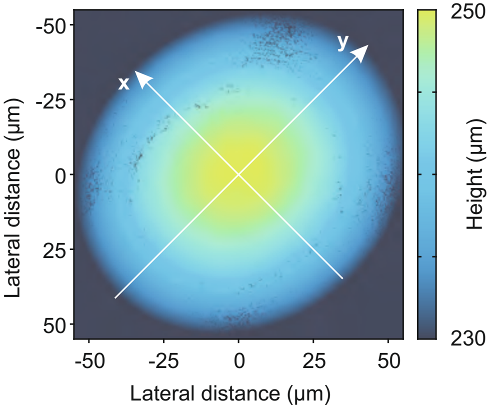

Figure 6.15. Characterization of the topography of a toric lens. Measurement of the topography using optical white light interferometry of a toric lens with radii of curvature of −75.8 µm and −95.8 µm in x- and y-direction, respectively.

sured beam width of the emerged beam of an optical single mode fiber SM 780HP. The beam width is determined by taking an image at each position. The toric lens has radii of curvature of −65.8 µm and −110.8 µm in the x- and y-coordinate, respectively. The simulations shown as straight lines are in good agreement with the measurement.

The two different focal length are linked to the conversion of the mode profile from an elliptically shaped profile with the long axis in y-direction, to a spherical one at a distance of around 2.81 mm behind the fiber, to an elliptically shaped mode profile with the long axis perpendicular to the first one. This is clearly visible in Fig. 6.16b, which shows two-dimensional Gaussian fits. For better visualization, Gaussian distributions are fitted to the measured images of a CCD camera of the stigmatic beam at different distances. The red circles are for clarification and support the visibility of the transition.

The toric lenses are fabricated layer-by-layer by exposing the photoresist Ormocomp on the tip of an optical fiber. A single mode fiber SM 780HP is used, as a laser diode with a wavelength of 808 nm is coupled into the fiber. In the lower part of

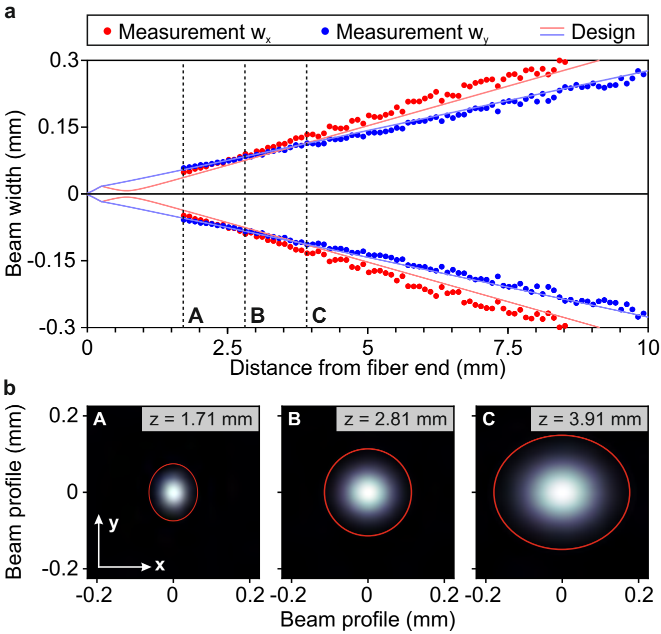

Figure 6.16. Toric lens for the generation or the correction of astigmatism. a, Measurement and simulation of the beam width w (radius of intensity at $1/e^2$) along the x- and y-coordinate of a toric lens with radii of curvature −65.8 µm and −110.8 µm, respectively. **b,** Two-dimensional Gaussian distributions fitted to the measured images of a CCD camera at different distances with respect to the optical fiber. The mode profile is converted from an elliptical beam profile with the long axis in y-direction (A), to a spherical one (B), to an elliptical beam profile with the long axis in the x-direction (C).

the toric lens the layer distance is 800 nm in order to save fabrication time during the manufacturing of this less crucial part of the lens. The curved part of the lens is fabricated with a layer distance of 200 nm and a lower laser power. During the fabrication the laser beam stays at a fixed position, whereas the fiber is moved by ultra-precise piezo actuators.

For the simulation Gaussian beam propagation using ABCD matrices is used in order to determine the beam width at certain distances behind the toric micro-lens. The simulation parameters are given in Section 6.1.

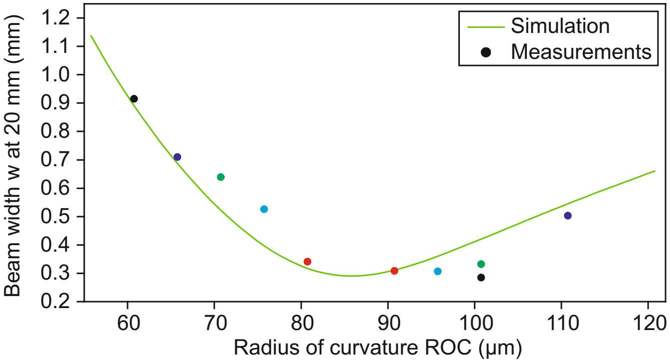

Figure 6.17. Beam widths of different toric lenses with respect to the radius of curvature. Same lenses are indicated by the same color.

In order to control the reliability of our fabrication method, we fabricated toric lenses with different ROC combinations and compared them in Fig. 6.17 with the simulations. The beam width at a distance of 20 mm is plotted over the radius of curvature (ROC). In the figure each toric lenses is indicated by two dots with the same color. In particular, the toric lenses have ROCs of 60.8 µm and 100.8 µm (black dots), 80.8 µm and 90.8 µm (red dots), 70.8 µm and 100.8 µm (green dots), 65.8 µm and 110.8 µm (dark blue dots), and 75.8 µm and 95.8 µm (blue dots). All toric lenses have a thickness D of 250 µm and are manufactured using the same fabrication parameters. The measurements are in agreement with the simulation.

6.4 DONUT INTENSITY SHAPER

Arbitrarily shaping the intensity distribution is one of the key goals of free-form optics. To this end, we present different examples of sub-micrometer free-form optics directly attached to single mode fibers.

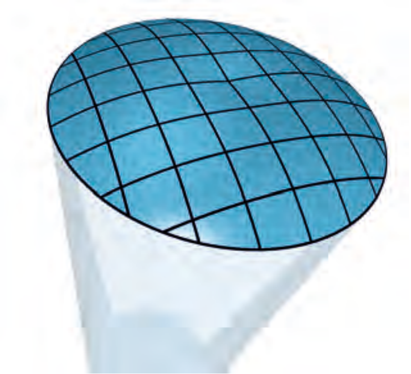

Figure 6.18. Free-form optical elements: Donut shaper. Illustration of a donut shaping free-form lens. The lens designs are calculated using an iterative optimization algorithm based on the Huygens-Fresnel principle.

As the calculation of free-form surfaces for optical applications is quite challenging and additionally strongly depends on the incident illumination field, different approaches to solve the redistribution of the radiation in order to create desired intensity distributions have been reported [101, 102, 103].

For our work, the scalar electromagnetic field at a certain distance behind the surface is calculated by numerically solving the Huygens-Fresnel diffraction integral for a given surface form (see Section 3.2).

As our micro-lenses are fabricated on the end facets of optical fibers, a Gaussian beam profile as the incident electromagnetic field distribution is used. Using a local optimization algorithm we iteratively improve our surface profile such that the resulting intensity distribution converges to the desired one. Using this simulation method we design the refractive surface in order to obtain a donut shaped intensity distribution.

Fig. 6.18 shows an illustration of a donut shaping free-form micro-optic. The lens shape consists of a slightly curved surface with an dip in the center of the optic.

The designed surface function of the donut shaper is represented by

$$Z(\rho) = a_0 + a_1 \cdot \rho + a_2 \cdot \rho^2 + a_3 \cdot \rho^3 + a_4 \cdot \rho^4 + a_5 \cdot \rho^5, \quad (6.1)$$

where

$$\rho = \sqrt{x^2 + y^2} \quad (6.2)$$

is the radial distance measured from the optical axis.
a_0, a_1,... are the coefficients of the polynomials. The parameters for the designed surface for the donut shaper are given in Table 6.1.

Parameters	
a_0	0.250 mm
a_1	0.109
a_2	−2.258 mm^{-1}
a_3	−56.670 mm^{-2}
a_4	308.000 mm^{-3}
a_5	930.646 mm^{-4}

Table 6.1. Parameters of the donut shaping free-form optic.

For the calculations the refractive index of the photoresist in the exposed state is 1.513, confirmed by refractive index measurements carried out by measuring the critical total internal reflection angle at different wavelengths (see Chapter A). For the beam waist of the Gaussian beam profile directly behind the end facet of the single mode fiber 780HP we use 2.45 µm, which is obtained by mode theory using the refractive indices of 1.4598 and 1.4537 for core and cladding material, respectively [71]. The core diameter of the fiber is 4.4 µm. The micro-lens surface is determined, so that the desired intensity profile is obtained on an observation screen at 20 cm distance.

Our free-form optics are directly fabricated on the end facet of an optical single mode fiber (SM 780HP). As photoresist IP-S is used in order to obtain a smooth surface, because of the high proximity effects. The beam shaping element has a diameter of 120 µm and a nominal height of 250 µm as specified in Table 6.1. The structures are manufactured by scanning the laser focus lateral by galvanometric mirrors. The vertical movement is carried out by piezo actuators. This method allows for fast and reproducible fabrication of sub-micrometer optical elements in a layer-by-layer technique. In order to save writing time, every lens is separated into two parts with different layer-by-layer distances, where the upper one contains the volume with the surface that is crucial for the refraction and the lower one only represents a base. The lower part is fabricated with a distance of 400 nm between the layers. In the upper part a layer distance of 100 nm is used. Additionally, the scan speed snd laser power is reduced in order to get an accurate surface shape.

Figure 6.19a displays the resulting two-dimensional intensity distributions after the fabrication at distances of 15 mm behind the fiber.

For comparison in Chapter C in the appendix the simulation and measurements of the pure single mode fiber SM 780HP without any optics are shown.

As non-uniform deformation occurs during the fabrication and development process, the intensity distribution of the free-form surfaces are extremely sensitive to variations of the surface. They are even more responsive to deviations than the spherical or toroidal lens surfaces, as the radiation field has to be completely redistributed. In order to determine the deviations, the measured intensity distribution is used in a backward calculation process, where the measurement results are used in our iterative optimization algorithm in order to calculate the fabricated surface. The backward calculated surface and a microscope side view is shown in Fig. 6.19b. Additionally, the designed surface shape is plotted as well. The intensity distribution achieved by using the backward calculated surface (depicted in Fig 6.19a as red curves) are in good coincidence with the measured ones.

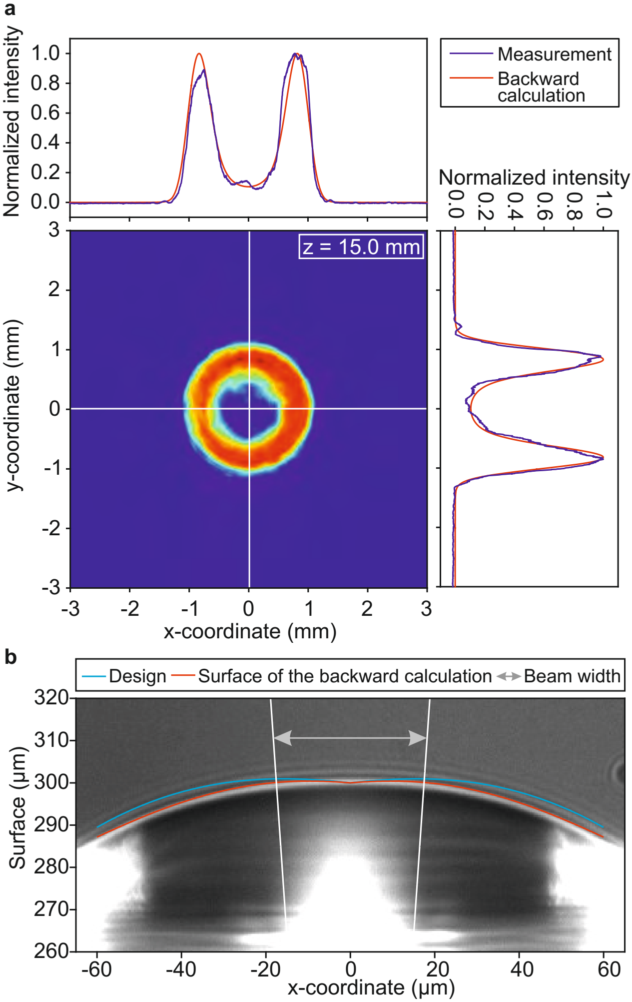

Figure 6.19. Measurement of a donut intensity distribution shaping micro optic. a, Intensity distribution of a donut shaped beam profile with cross sections in x- and y-direction. In addition, the backward calculation which has been determined from the measurement is shown. **b,** Microscope image of the side view of the donut shaping free-form optical element with indicated designed surface and the surface based on backward calculation out of the measurement results.

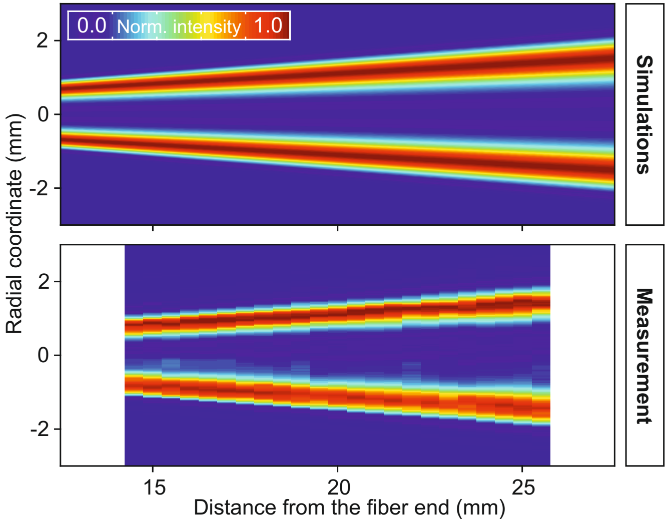

Figure 6.20. Comparison between measurement and simulation of intensity distribution of the donut shaper for different distances. Simulation (top) and measurement (bottom) of the intensity distribution of the donut shaping free-form optics at different distances after the fiber end. The measured cross section is obtained by taking the average of the cross section in x- and y-direction.

The backward calculated surface is described by a modified aspheric surface

$$\begin{aligned} Z(\rho) = a_0 + \frac{c\rho^2}{1+\sqrt{1-(1+k)c^2\rho^2}} \cdots \\ + a_1 \cdot \rho + a_2 \cdot \rho^2 + \cdots + a_{10} \cdot \rho^{10}, \end{aligned} \tag{6.3}$$

where c is the curvature (inverse of radius of curvature (ROC)) and k is the conic constant. ρ is the radial distance measured from the optical axis. a_0, a_1,... are the polynomial deformation parameters. The backward-calculated surface is described by the parameters given in Table 6.2. The surface is in good agreement with the microscope side view of the lens.

Figure 6.20 shows simulations in comparison to the measurement results. The simulated intensity distribution is determined

Parameters	
a_0	$0.250\,\mathrm{mm}$
a_1	$8.150 \cdot 10^{-2}$
a_2	$-3.430\,\mathrm{mm}^{-1}$
a_3	$-6.696 \cdot 10^{1}\,\mathrm{mm}^{-2}$
a_4	$7.639 \cdot 10^{2}\,\mathrm{mm}^{-3}$
a_5	$1.059 \cdot 10^{3}\,\mathrm{mm}^{-4}$
a_6	$1.384 \cdot 10^{-3}\,\mathrm{mm}^{-5}$
a_7	$7.024 \cdot 10^{-4}\,\mathrm{mm}^{-6}$
a_8	$-3.896 \cdot 10^{-3}\,\mathrm{mm}^{-7}$
a_9	$-9.114 \cdot 10^{-4}\,\mathrm{mm}^{-8}$
a_{10}	$-1.962 \cdot 10^{-4}\,\mathrm{mm}^{-9}$
c	$4.164 \cdot 10^{-5}\,\mathrm{mm}^{-1}$
k	$-4.188 \cdot 10^{-4}$

Table 6.2. Parameters of the backward calculation for the donut shaping free form optic.

by numerically solve the Huygens-Fresnel integral for each propagation distance value using the backward calculated surface shape. For the measurement at each position an image of the intensity distribution is taken. The resulting cross section is determined by taking the average of the cross section in x- and y-direction. Measurement and simulation are in excellent agreement.

In addition the surface is characterized by an optical Linnik interferometer in order to proof the high optical quality of the donut shaping lens (Fig. 6.21) [104, 105]. The surface shape is very smooth and homogeneous, which confirms the good fabrication quality.

The topography is determined by analyzing the phase data. The rms (root mean square) roughness is determined by subtracting a two-dimensional polynomial surface of 10th order. We obtained a roughness of 30 nm rms in the central region of the free-form optic, which is in good agreement with the sub-micrometer fabrication accuracy of two-photon direct laser writing.

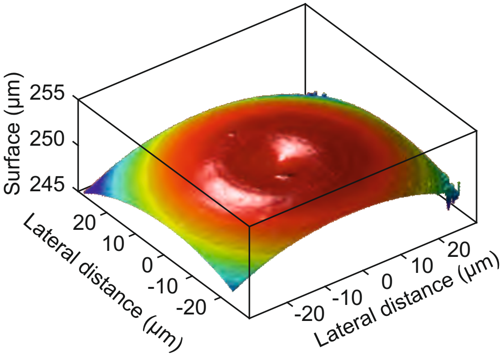

Figure 6.21. Surface characterization of the donut intensity distribution shaping micro-optic. Measurement of the topography using optical Linnik interferometry measurements.

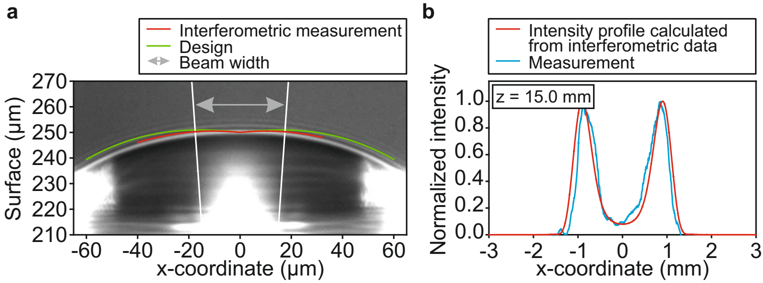

Figure 6.22. Optical Linnik interferometry measurements for controlling the fabrication quality of the donut shaping sub-micrometer freeform optic. a, Comparison between the designed surface and the interferometry measurement results. **b,** Cross sections of the measured intensity distribution of the donut shaped beam profile at a distance z of 15 mm. In addition, the profile achieved by simulating the interferometry measurement data is shown.

Figure 6.22a depicts a cross section of the interferometric measurement. In the figure the measurement results are compared to a microscope side view of the free-form lens and to the design. The surface shape excellently fits with the measurement results, but deviates from the design, as there is a non-uniform shrinkage. We use the measurement data of the interferometric measurement in order to calculate the intensity distribution. Fig. 6.22b shows the measurement data as well as the intensity profile, which is calculated from the interferometric measurement data. Both are in excellent agreement and show the designed donut shaped intensity profile.

Although, there is a non-uniform deformation, which leads to a deviation between designed and fabricated surface, a nicely shaped donut profile is created by our free-form micro optic.

6.5 CIRCULAR TOP HAT INTENSITY SHAPER

In various fields there is the need to have a flat intensity distribution with defined size and shape. Top hat intensity distribution, e.g., have a uniform intensity over a certain area with a sharp transition region from the area illuminated by maximal intensity and the non-illuminated one. This can be of advantage for laser treatment as there is a clear border between the two regions. Usually, Gaussian intensity distributions are used, where the intensity gradually decreases from the maximal intensity in the center to zero-intensity at the borders.

Figure 6.23 shows an illustration of a circular top hat intensity shaping free-form optic. The micro-lens is designed to be directly attached to an optical single mode fiber. In contrast to the diffractive elements presented in Chapter 4 the free-form optics use refraction in order to shape the emerged beam. The top hat shaping element consists of a strongly curved surface at the edge and a nearly flat central region, as shown in Fig. 6.23.

The surface shape is calculated by a Huygens-Fresnel diffraction approach, which was introduced in Chapter 3.2. The Huygens-Fresnel-Kirchhoff diffraction integral is numerically solved for an incident Gaussian beam and the aspheric surface shape is optimized by utilizing the rotational symmetry of

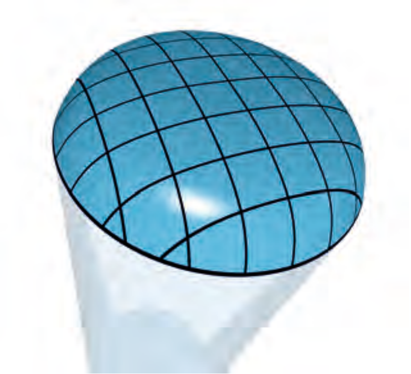

Figure 6.23. Free-form optical element: A circular top hat shaper. Illustration of a circular top hat shaping free-form optic. The lens design is calculated by an iterative optimization algorithm using Huygens-Fresnel principle.

surface and electromagnetic field in an iterative algoritm. In each iteration step the intensity distribution at a certain distance behind the optical element is calculated and compared to the desired intensity distribution.

The designed surface function of the top hat intensity shaper is represented by

$$Z(\rho) = a_0 + a_2 \cdot \rho^2 + a_4 \cdot \rho^4 + \cdots + a_{10} \cdot \rho^{10}, \tag{6.4}$$

where

$$\rho = \sqrt{x^2 + y^2} \tag{6.5}$$

is the radial distance measured from the optical axis. The calculated parameters for the designed surface for the top hat intensity shaper are given in Table 6.3. For the simulations a propagation wavelength of 808 nm is used. The beam waist emerging from the optical single mode fiber is set to be 3.0 µm, although the calculated value is 2.45 µm. As the top hat intensity shaper completely redistributes the light field, the created intensity distribution is strongly dependent on the surface shape. In order to compensate the non-uniform deformation during fabrication, the surface

Parameters	
a_0	$0.295\,\mathrm{mm}$
a_2	$2.749 \cdot 10^{-1}\,\mathrm{mm}^{-1}$
a_4	$-3.423 \cdot 10^{3}\,\mathrm{mm}^{-3}$
a_6	$1.722 \cdot 10^{6}\,\mathrm{mm}^{-5}$
a_8	$-4.971 \cdot 10^{8}\,\mathrm{mm}^{-7}$
a_{10}	$1.072 \cdot 10^{9}\,\mathrm{mm}^{-9}$

Table 6.3. Parameters of the top hat intensity shaping free-form optic.

is adapted by using a slightly different beam waist ($w_0 = 3.0\,\mu\mathrm{m}$). The adaption is not obvious and is arbitrarily chosen, but experimental results and experience confirm the choice. Alternatively, an iterative algorithm can be used in order to compensate the non-uniform deformation. In each step the surface shape is improved in order to get a circular uniform intensity distribution. More details can be found in Chapter 8.5.

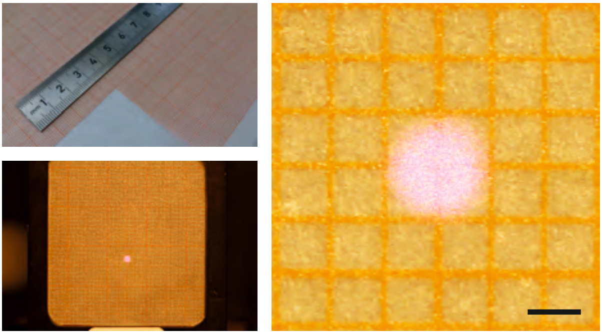

Figure 6.24. Measured intensity profile of a top hat intensity shaping micro-optic. The micro-optic is directly fabricated on the end facet of a single mode fiber. The lens has a height of 295 µm. As an observation screen graph paper is used at a distance of 22 mm. Scale bar, 1 mm.

Figure 6.24 shows the measurement results of a top hat shaping micro-lens, directly fabricated on an optical single mode fiber SM 780HP. As an observation screen graph paper is used. The screen is at a distance of 22 mm. The free-form micro-optic creates a homogenous illumination over a circular area with a diameter of roughly 2 mm.

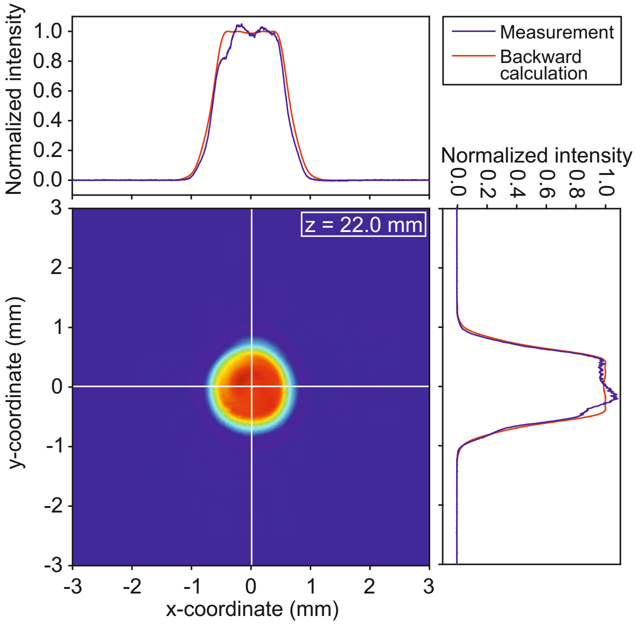

Figure 6.25. Measurement of a top hat intensity shaping micro-optic. Intensity distribution of a top hat shaped beam profile with cross sections in x- and y-direction. In addition, the backward calculation which has been determined from the measurement is shown.

The micro-lens is fabricated using dip-in direct laser writing. Fabrication time is saved by again dividing the micro-optic into two parts. The lower part represents a base, which is fabricated with a layer distance of 400 nm. The curved part is fabricated with 50 nm between neighboring layers, in order to get a highly accurate surface shape.

Figure 6.25 depicts the measured intensity distribution. The measurement results are obtained by taking an image of the intensity distribution by a CCD camera at a distance of 22 mm behind the optical fiber. The cross sections in x- and y-direction confirm the uniform intensity over an area of a circle.

As there is a non-uniform deformation during the fabrication and development process, we used the measured intensity distribution in order to calculate the real surface shape. The backward calculated surface is described by a modified aspheric surface, given by

$$\begin{aligned} Z(\rho) = a_0 + \frac{c\rho^2}{1+\sqrt{1-(1+k)c^2\rho^2}} \dots \\ + a_1 \cdot \rho + a_2 \cdot \rho^2 + \dots + a_{10} \cdot \rho^{10}, \end{aligned} \tag{6.6}$$

where c is the curvature (inverse of radius of curvature ROC) and k is the conic constant. ρ is the radial distance measured from the optical axis. For the backward calculation we use the calculated value of the beam waist, which is 2.45 µm. As mentioned above this value is determined by mode theory using the refractive indices of the fiber material and the parameter of fiber geometry. The backward calculated surface is described by the parameters given in Table 6.4. The intensity profile generated by the backward calculated surface is plotted as a red line in Fig. 6.25. It is in

Parameters	
a_0	0.295 mm
a_1	$-5.737 \cdot 10^{-4}$
a_2	$-2.410\,\text{mm}^{-1}$
a_3	$-8.461 \cdot 10^{-2}\,\text{mm}^{-2}$
a_4	$-2.010 \cdot 10^{3}\,\text{mm}^{-3}$
a_5	$-1.908 \cdot 10^{-1}\,\text{mm}^{-4}$
a_6	$1.557 \cdot 10^{6}\,\text{mm}^{-5}$
a_7	$-4.580\,\text{mm}^{-6}$
a_8	$-5.385 \cdot 10^{8}\,\text{mm}^{-7}$
a_9	$9.165 \cdot 10^{-2}\,\text{mm}^{-8}$
a_{10}	$-1.196\,\text{mm}^{-9}$
c	$-1.839 \cdot 10^{-3}\,\text{mm}^{-1}$
k	$-1.594 \cdot 10^{-2}$

Table 6.4. Parameters of the backward calculated for the top hat intensity shaping free-form optic.

good agreement with the measured intensity profiles (blue lines). Fig. 6.27 shows a side view of the free-form optic. In addition the designed surface is depicted in green. The surface, which is determined by the backward calculation is shown as a red line. The surface in the microscope image is in excellent agreement with the backward calculated surface shape. Therefore, the approach by using the measured intensity to determine the fabricated surface including the deformation is a valid method.

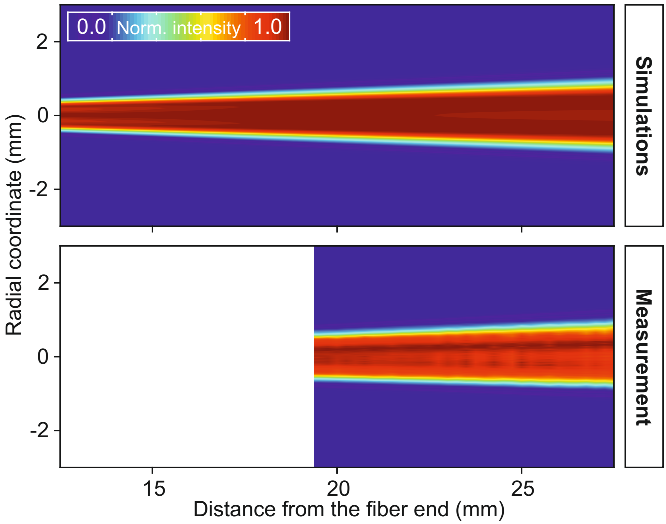

Figure 6.26. Comparison between measurement and simulation of intensity distribution of the top hat shaper for different distances. Simulation (top) and measurement (bottom) of the intensity distribution of the donut shaping free-form optics at different distances after the fiber end. The measured cross section is obtained by taking the average of the cross section in x- and y-direction. The simulated intensity distribution in each step is obtained by numerically solving the Huygens-Fresnel diffraction integral in two dimensions. As surface parameters the backward-calculated parameters are used. For the measurement at each distance a picture of the intensity profile is taken using a CCD camera.

Figure 6.26 shows intensity profiles in simulation and measurement for different distances behind the fiber end facet. The simulated intensity distribution is determined by numerically solving the Huygens-Fresnel integral for each propagation distance value using the backward calculated surface shape. For the measurement at each position a image of the intensity distribution is taken. The resulting cross section is determined by taking the average of the cross section in x- and y-direction. Measurement and simulation are in excellent agreement.

For comparison in Chapter C in the appendix the simulation and measurements of the pure single mode fiber SM 780HP without any optics are shown.

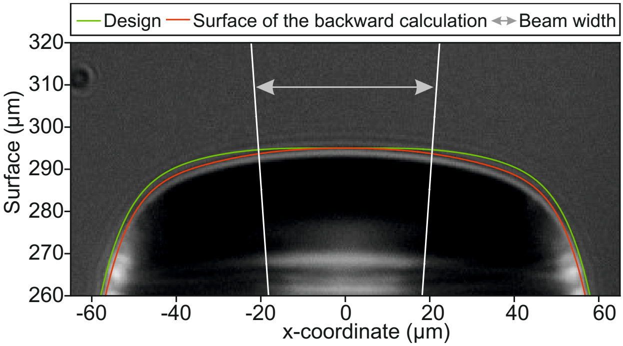

Figure 6.27. Surface characterization of the top hat intensity shaping micro optic. Microscope image of the side view of the top hat shaping free-form optical element with indicated designed surface and the surface based on backward calculation out of the measurement results.

The fabricated surface shape is additionally verified by white light interferometer measurements using an optical Linnik interferometer [104, 105]. Fig. 6.28 shows the measured central area of the surface. Although the free-form optic is fabricated layer-by-layer, the surface is smooth without any defects. At the edge of the measured area there are some steps, which are likely caused by phase shifts in the Linnik interferometer measurement. As the surface is strongly curved at the edges phase jumps in the measurements are very likely.

For the evaluation the phase values of the interferometric measurement are used. We determined the surface roughness by subtracting a two-dimensional polynomial of 10th order. The rms

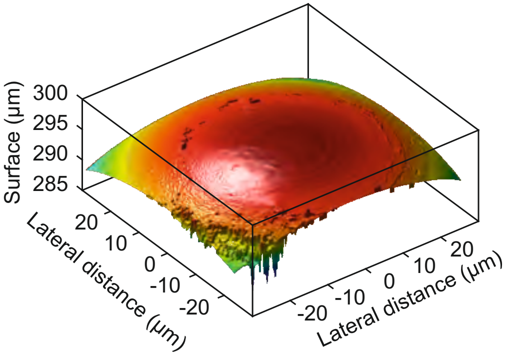

Figure 6.28. Surface characterization of the top hat intensity shaping micro optic. Measurement of the topography using optical Linnik interferometry. Although the micro-optical element is fabricated layer-by-layer a smooth surface is obtained.

surface roughness is 30 nm in the central area of the optic. The obtained value is in excellent agreement with the measurements of the donut shaping sub-micrometer free-form optic presented in Section 6.4 and proves the high sub-micrometer accuracy of two-photon direct laser writing.

Figure 6.29a shows the surface profile obtained by the white light interferometer measurement in comparison to the design and a side view of the free-form optic. The surface shapes are in good agreement, however the non-uniform deformation is clearly visible. Fig. 6.29b depicts the simulated intensity distribution, calculated using the interferometric measurement results. As the absolute height of the micro-lens cannot be determined by an optical Linnik interferometer the apex of the surface is set to 295 µm. The cross sections of the intensity distributions are plotted at a distance z of 22 mm. Most likely, the mismatch is due to a wrong height or a slight shift in lateral direction.

In order to make some assumption concerning the non-uniform deformation during the fabrication and development process we calculated the deviation between the designed surface and the surface obtained by the backward calculation. Fig. 6.30 shows the deviation. Additionally, we fitted a polynomial Z_p and a conic

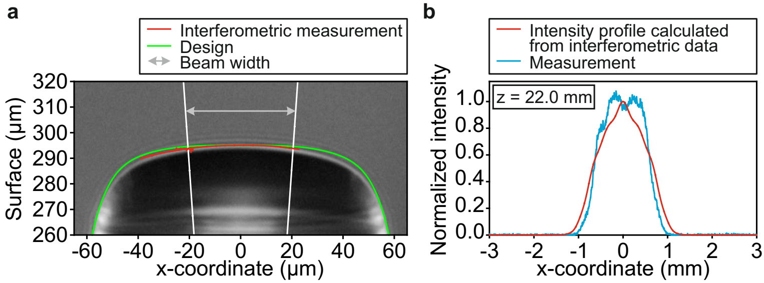

Figure 6.29. Optical Linnik interferometry measurements for controlling the fabrication quality of the top hat shaping free-form optic. a, Comparison between the designed surface and the interferometry measurement results. **b,** Cross sections of the measured intensity distribution of the top hat shaped beam profile at a distance z of 22 mm. In addition, the profile achieved by simulating the interferometry measurement data are shown.

curve Z_c to the deviation. The polynomial function is plotted as a green dashed line and fits perfectly with the deviation (red line). The more simple conic curve is shown as a blue dashed line. As polynomial curve we use even terms up to 12th degree. The function is given by

$$\begin{aligned} Z_p(\rho) = a_{0,p} + a_{2,p} \cdot \rho^2 + a_{4,p} \cdot \rho^4 + a_{6,p} \cdot \rho^6 + a_{8,p} \cdot \rho^8 \dots \\ + a_{10,p} \cdot \rho^{10} + a_{12,p} \cdot \rho^{12}, \end{aligned} \tag{6.7}$$

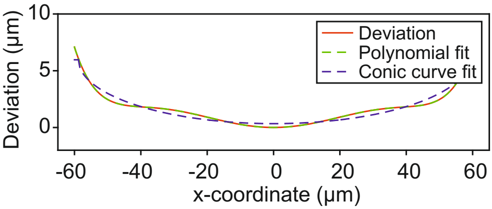

Figure 6.30. Surface deviation between design and backward calculated profile. As fit functions a polynomial and a conic curve are used in order to mathematically describe the non-uniform deformation.

where $\rho = \sqrt{x^2 + y^2}$ represents the radial coordinate, assuming a rotationally symmetric deformation. $a_{0,p}$, $a_{2,p}$,... are the polynomial coefficients. The fit parameters are are given in Table 6.5. The conic surface Z_c is described by

Parameters	
$a_{0,p}$	$3.206 \cdot 10^{-9}$ m
$a_{2,p}$	$2.792 \cdot 10^{3}$ m^{-1}
$a_{4,p}$	$-1.394 \cdot 10^{12}$ m^{-3}
$a_{6,p}$	$1.436 \cdot 10^{20}$ m^{-5}
$a_{8,p}$	$4.996 \cdot 10^{28}$ m^{-7}
$a_{10,p}$	$3.073 \cdot 10^{-4}$ m^{-9}
$a_{12,p}$	$-3.054 \cdot 10^{-4}$ m^{-11}

Table 6.5. Parameters of the polynomial fit to the deviation.

$$Z_c(\rho) = a_c + \frac{c_c \rho^2}{1 + \sqrt{1 - (1 + k_c) c_c^2 \rho^2}}, \tag{6.8}$$

where a_c is an offset. c_c is the curvature at the apex of the deviation and k_c is the conic constant. Dependent on the value of the k_c the deviation can be a hyperboloid, a paraboloid, or a oblate or prolate spheroid. The fit parameters for the conic surface are given in Table 6.6. The fitted functions can be used for the compensation of the deformation. More details are in the following section or in Chapter 8.5. However, one has to keep in mind that to our experience the mathematical description of the deformation can in general not be used as it is highly dependent on the

Parameters	
$a_{0,c}$	$3.367 \cdot 10^{-7}$ m
c_c	$1.627 \cdot 10^{3}$ m^{-1}
k_c	$1.083 \cdot 10^{2}$

Table 6.6. Parameters of the conic fit to the deviation.

surface shape by itself. Additionally, the photoresist material and the writing parameters influence the shape, as well.

6.6 SQUARE TOP HAT INTENSITY SHAPER

Free-form optics are not restricted to the generation of rotationally symmetric intensity distributions. As the surface can be designed freely, nearly any intensity profile can be created by two-photon direct laser writing. Usually complex non-rotationally symmetric intensity patterns are generated by diffractive optics, as the fabrication of refractive free-form optics is highly challenging.

Two-photon direct laser writing has the advantage, that the additive fabrication process enables complex structures without any restrictions. Therefore, we use dip-in direct laser writing for the fabrication of a square top hat intensity shaping micro-optic.

The shape of the surface is assumed to be a two-dimensional aspheric surface, given by

$$\begin{aligned} Z(x,y) = a_0 &+ \frac{c_x x^2}{1+\sqrt{1-(1+k_x)c_x^2 x^2}} \dots \\ &+ a_{2,x}\cdot x^2 + a_{4,x}\cdot x^4 \dots \\ &+ a_{6,x}\cdot x^6 + a_{8,x}\cdot x^8 + a_{10,x}\cdot x^{10} \dots \\ &+ \frac{c_y y^2}{1+\sqrt{1-(1+k_y)c_y^2 y^2}} \dots \\ &+ a_{2,y}\cdot y^2 + a_{4,y}\cdot y^4 \dots \\ &+ a_{6,y}\cdot y^6 + a_{8,y}\cdot y^8 + a_{10,y}\cdot y^{10}, \end{aligned} \tag{6.9}$$

where c_x and c_y are the curvatures at the apex along the x- and y-axis, respectively. The curvatures are the reciprocal of the radius of curvature (ROC). k_x and k_y are the conic constants in x- and y-direction, where the surface can be a hyperboloid for $k < -1$, a paraboloid for $k = -1$, a prolate spheroid for $-1 < k < 0$, a sphere for $k = 0$, and oblate spheroid for $k > 0$. $a_{2,x}, a_{2,y}, \dots$ are the deformation coefficients. If they are all 0, it results in a pure conic surface.

By numerically solving the Huygens-Fresnel-Kirchhoff diffraction integral in four dimensions the coefficients are determined. For the numeric calculation a refractive index of the lens material of 1.513 is used. The beam waist at the end facet of the optical fiber is 2.45 µm, which is determined by mode theory using 1.4598 and 1.4537 as refractive indices of core and cladding material, respectively. The core diameter of the single mode fiber SM 780HP is 4.4 µm. Additionally, we use 808 nm as wavelength, which corresponds to the used laser source.

In order to reach a quadratic uniform intensity distribution at a distance of 20 mm, we use an iterative optimization algorithm. In each step the Huygens-Fresnel-Kirchhoff diffraction integral for a given surface shape is solved in order to obtain the intensity distribution. The intensity profile is compared to a desired one and subsequently, the surface shape is optimized.

Parameters			
a_0	$295 \cdot 10^{-6}\,\mathrm{m}$		
c_x	$-1.200 \cdot 10^{-1}\,\mathrm{m}^{-1}$	c_y	$-1.200 \cdot 10^{-1}\,\mathrm{m}^{-1}$
k_x	$-4.448 \cdot 10^{-4}$	k_y	$-4.448 \cdot 10^{-4}$
$a_{2,x}$	$2.542 \cdot 10^{2}\,\mathrm{m}^{-1}$	$a_{2,y}$	$2.542 \cdot 10^{2}\,\mathrm{m}^{-1}$
$a_{4,x}$	$-4.672 \cdot 10^{12}\,\mathrm{m}^{-3}$	$a_{4,y}$	$-4.672 \cdot 10^{12}\,\mathrm{m}^{-3}$
$a_{6,x}$	$3.838 \cdot 10^{21}\,\mathrm{m}^{-5}$	$a_{6,y}$	$3.838 \cdot 10^{21}\,\mathrm{m}^{-5}$
$a_{8,x}$	$-1.310 \cdot 10^{30}\,\mathrm{m}^{-7}$	$a_{8,y}$	$-1.310 \cdot 10^{30}\,\mathrm{m}^{-7}$
$a_{10,x}$	$2.330 \cdot 10^{36}\,\mathrm{m}^{-9}$	$a_{10,y}$	$2.330 \cdot 10^{36}\,\mathrm{m}^{-9}$

Table 6.7. Parameters of the shape of the square top hat intensity shaper.

Table 6.7 contains the coefficients of the surface shape. The parameters are the same for the x- and y-direction.

Figure 6.31a and 6.31b show a three- and two-dimensional plot of the surface shape, which is described by the parameters in Table 6.7. The micro-optical beam shaper has a height of 295 µm and a diameter of below 60 µm. The surface shape already suggests the quadratic, uniform intensity distribution.

For several distances the simulated intensity distributions are shown in Figure 6.31c. We simulate the profile at distances of 5 mm, 7 mm, and 20 mm, numerically solving the Huygens-Fresnel-Kirchhoff diffraction integral for the designed surface.

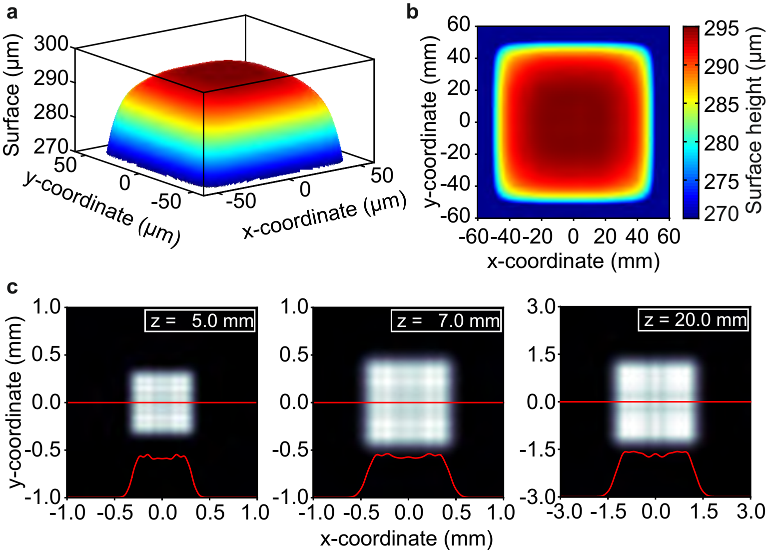

Figure 6.31. Surface design and simulation in order to shape a top hat intensity distribution. a, b, Surface shape of a top hat shaping free-form optic. The optic design is calculated by an iterative optimization algorithm using Huygens-Fresnel principle. **c,** Simulated intensity distribution of a top hat shaped intensity profile with cross sections in x-direction. The intensity distribution is simulated at distances of 5 mm, 7 mm, and 20 mm.

There are only small differences in the intensity pattern for varying distances of the observation screen. The quadratic, uniform intensity can be recognized at all distances.

Figure 6.32 shows the intensity measurements at distances of 5 mm and 7 mm. As there is a non-uniform shrinkage the fabricated surface without any adaption (left column) indeed creates a quadratic intensity pattern, but this does not have an uniform intensity distribution. By adding some compensation for shrinkage to the designed surface the intensity pattern can be considerably improved. We added the fitted deviation shown in 6.30. The deviation is obtained from the measurements and backward calculations of the spherical top hat intensity shaper. The profiles are defined in Equation 6.7 and 6.8 for the polynomial and the

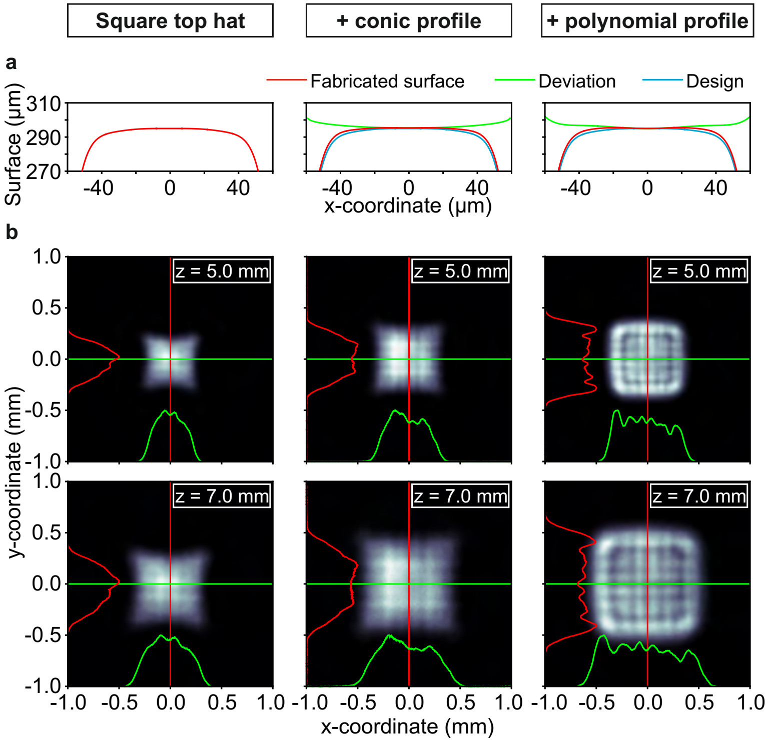

Figure 6.32. Measurements of a top hat intensity shaping optic. a, In order to compensate non-uniform shrinkage during the fabrication process, the design (left) as well two modified surface shapes are fabricated. A conic (middle) and a polynomial (right) profile are added to the complex surface shape of the design. The profile mathematically describes the deformation obtained in the case of the circular top hat intensity shaper presented in Section 6.5. **b,** Intensity distribution of a square top hat shaped beam profile with cross sections in x- and y-direction at 5 mm and 7 mm distance for the different surface shapes.

conic fit. The related parameters can be found in Table 6.5 and 6.6.

The middle row of Fig. 6.32 depicts the measurements of the adapted surface, where we added a conic compensation. The measurements are carried out at distances of 5 mm and 7 mm by taking images with a CCD camera. There is an improvement in the intensity pattern. The cross sections show an uniform intensity distribution in the central region, whereas there is a large transition region on the flanks. This can be further improved by adding a more detailed polynomial curve to the designed surface. The two-dimensional intensity patterns are shown in the right column of Fig. 6.32.

The measurements are in good agreement with the simulations shown in Fig. 6.31. In simulation as well as in the measurements overshoots on the flanks are visible. Additionally, there are only small differences in the intensity at distances of 5 mm and 7 mm, which is confirmed by the measurements.

7

MULTI-LENS SYSTEMS

Complex micro-optical elements for imaging or beam shaping, which show satisfying optical quality and performance are still difficult in fabrication. In addition, most approaches are limited in design freedom and system complexity [19]. Until now the fabrication of micro-optical multi-lens optical systems, which show performance comparable to conventional microscope objectives and optics appear to be beyond reach. In this chapter we will discuss ways to overcome the aforementioned challenges.

The sub-micrometer compound elements presented in this chapter are designed and optimized within the optical design software ZEMAX (see Chapter 3). In order to compensate for optical aberrations and improve the image quality for each surface, aspheric surface shapes are used. Our optical devices consist of several different free-form lens elements separated by air. The lens design is exported and converted into a stereo-lithographic file format. Subsequently, the compound lenses are fabricated by three-dimensional dip-in direct laser writing utilizing a commercially available femtosecond laser lithography system (Photonic Professional GT, Nanoscribe GmbH, Germany) [64]. The complete optical compound system is manufactured from a single material. We use a photoresist that exhibits high optical quality and at the same time creates smooth surfaces (IP-S, Nanoscribe GmbH, Germany).

7.1 MULTI-LENS SYSTEMS FOR IMAGING

Figure 7.1 shows a schematic illustration of a triplet lens system. Several different free-form lens elements are combined into a compound lens in a supporting shell, which serves differnt requirements at once. On the one hand, it axially and laterally aligns the individual optical elements and therefore, prevents tilting; on the other hand, it serves as protection. The shell is

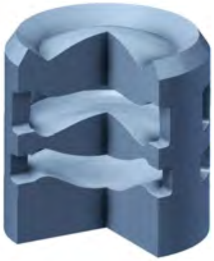

Figure 7.1. Schematic illustration of a triplet system. The triplet system consists of several different singlet lenses, which are combined to a multi-lens system in a supporting shell.

equipped with several holes that are needed for the development process but can also be used for a subsequent structuring with an antireflection coating by atomic layer disposition (ALD) or other surface treatments. Additional information concerning the design and fabrication are included in Chapter 2 and 3, respectively.

We manufacture compound lenses with different numbers of surfaces starting from one to five refractive interfaces. Fig. 7.2 depicts a comparison between a singlet, a doublet, and a triplet lens system, fabricated on a 170 µm thick glass substrate. Each compound lens has a total diameter of around 115 µm. The lenses are designed to have a large field of view of 80°, which corresponds to an object space NA of 0.98. The focal lengths are 68.3 µm at a wavelength of 550 nm. As one can already see from the optical design and the ray-tracing simulations in Fig. 7.2a and Fig. 7.2b, the performance improves with increasing number of interfaces. While in the singlet lens design the rays across the field are not well imaged onto one single point, in the triplet lens design the rays incident from different angles converge into a single point in the image plane at the rightmost interface. Simulations with a USAF 1951 resolution test chart in Fig. 7.2b confirm this observation. The simulation of the singlet lens exhibits a strong image field curvature that is recognizable by blurry edges of the image. Additionally, the magnification of the singlet lens is non-

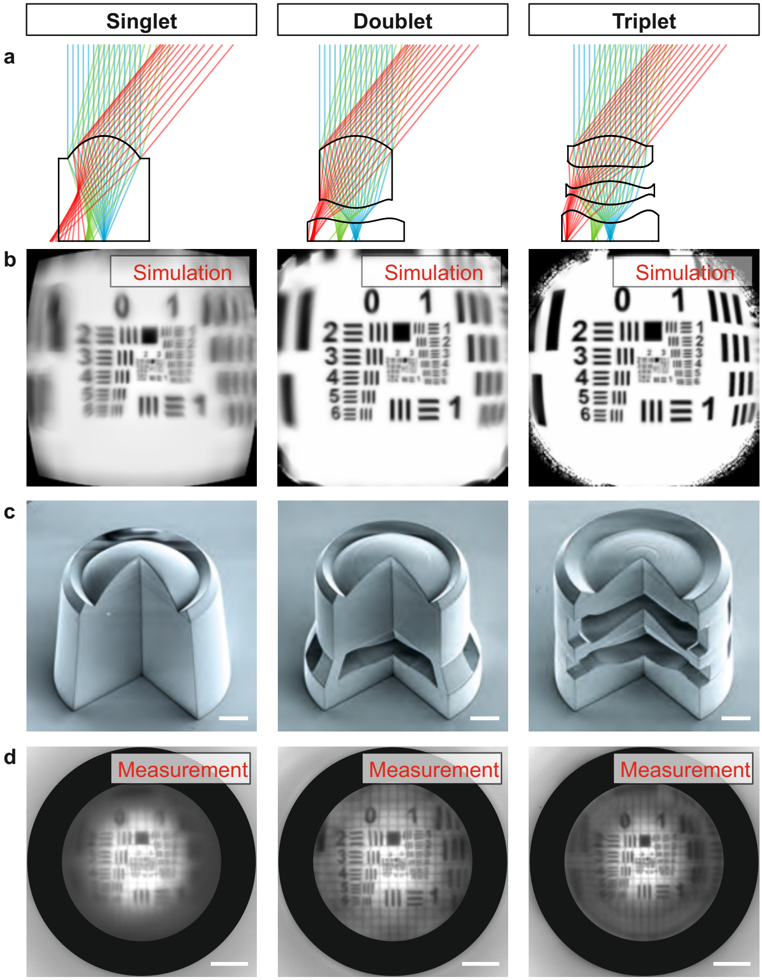

Figure 7.2. Comparison of singlet, doublet, and triplet printed lens system. a, Optical design of a singlet, doublet, and triplet lens system optimized within ZEMAX. **b,** Image simulation of the USAF 1951 resolution test chart. **c,** Scanning electron microscope images of the singlet, doublet, and triplet lens systems. **d,** Image of the USAF 1951 resolution test chart taken through the singlet, doublet, and triplet lens systems. The distance between lens and target is 20 mm. Scale bars, 20 µm.

uniform across the image field. The barrel distortion is clearly visible at the edges of the image in the singlet simulation of Fig. 7.2b. By increasing the numbers of refractive interfaces, the optical aberrations, namely image field curvature and distortion, can be compensated.

Fig. 7.2c shows scanning electron microscope images of the singlet, doublet, and triplet lens system that have been manufactured with a 90° slice cut out for demonstration purposes. Each lens element is manufactured layer-by-layer from the same material. The lenses are exposed by two-photon absorption in an ultraviolet sensitive photoresist (IP-S, Nanoscribe GmbH, Germany) at a wavelength of 780 nm. In order to fabricate these bulky structures a dip-in lithography configuration is used. The designed structures are written layer-by-layer with a distance of 100 nm between the individual layers. For this, ultra-precise piezo actuators move the sample in axial direction after fabricating each layer. In lateral direction the laser beam is guided by galvanometric mirrors parallel to the substrate. The diameters of the lenses are 120 µm including the supporting shell. The SEM image confirms the high manufacturing quality and the excellent shape fidelity.

Fig. 7.2d shows the optical performance of the singlet, doublet, and triplet lens system achieved by imaging the USAF 1951 resolution test chart at a distance of about 20 mm. We imaged the rightmost surface by an optical microscope using a 50x objective lens and a CCD camera. The true color images are subsequently converted to grayscale intensity images. The simulations and measurements of the imaging performance exhibit good agreements. Just as in the simulations, the barrel distortion and the image field curvature disappear by increasing the number of refractive surfaces. In the measurements the natural illumination dropoff and the effect of optical vignetting are visible. The optical vignetting is caused by the physical dimensions of the optical system, whereas the natural drop is caused by $\cos^4$-law for the relative illumination. The drop-off is particularly enhanced for the triplet lens system, as Fresnel reflections at five interfaces are substantial.

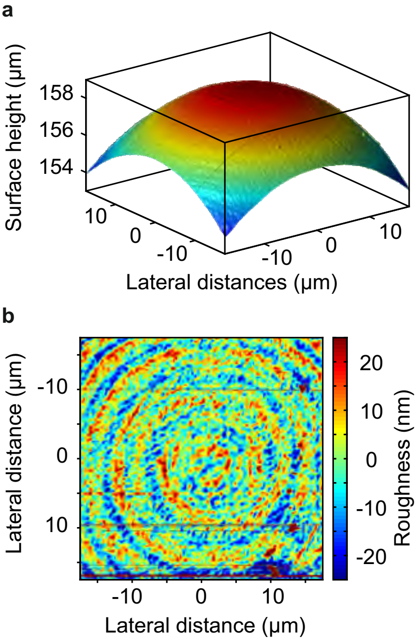

Figure 7.3. Atomic force microscope measurement of the central part of the front surface of a doublet lens system. The doublet lens system is fabricated with a layer-by-layer distance of 100 nm. **a,** 35 × 35 μm^2 area of the surface. **b,** Roughness obtained by subtracting a two-dimensional polynomial surface of 10^{th} order. The surface shows a roughness of 13 nm rms.

In order to quantify the fabrication tolerances the surface is additionally characterized by atomic force microscope measurements (AFM measurements). We analyzed an area of 35 × 35 μm^2 of the front surface of doublet lens system, which is introduced in Fig. 7.2. The region is centrally adjusted with respect to the vertex. The lens is fabricated with a layer-by-layer distance of 100 nm. Fig. 7.3 shows the measured surface shape, which shows a smooth surface. The rms (root mean square) roughness is obtained by subtracting a two-dimensional polynomial surface of 10^{th} order. A surface roughness of less than

15 nm rms is easily feasible (see Fig. 7.3) as we use a photoresist which exhibits high proximity effects.

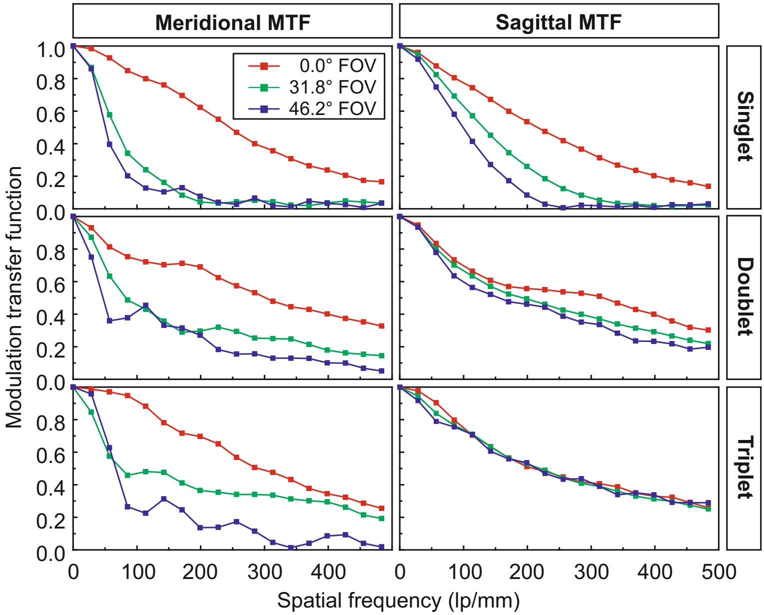

Figure 7.4. Performance measurement using knife edge methodology in order to determine the modulation transfer function (MTF) of the singlet, doublet, and triplet. Measurement of the meridional and sagittal modulation transfer function (MTF) for different angles. The singlet, doublet, and triplet lens systems are introduced in Fig. 7.2.

Figure 7.4 shows the modulation transfer function (MTF) of the single, doublet, and triplet lens system. They are measured using a knife edge method [106, 107, 108, 109]. In order to accomplish this, the sharp edge of a razor blade is imaged by the 3D printed compound lens and a 50x objective onto the CCD camera at various field positions and with different orientations.

A measurable improvement in the contrast (modulation) is observed by increasing the number of refractive elements. Whereas the singlet lens only shows a sufficient performance for an angle of 0°, the doublet and triplet lens systems even show a good performance for large angles.

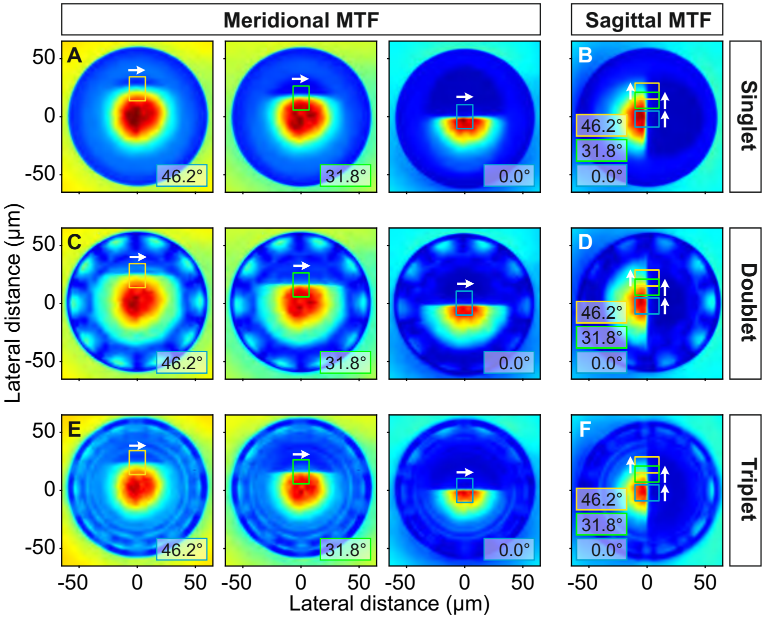

Figure 7.5. Knife edge measurement methodology in order to determine the modulation transfer function (MTF) shown in Fig. 7.4. **a,** Images of the knife edge for the calculation of the edge spread function in the meridional plane. For the different fields of view (48.0°, 34.6°, and 0.0°) the edge spread function is determined by summing up along the arrows. **b,** Images of the knife edge for the calculation of the edge spread function in the sagittal plane. For the different fields of view (48.0°, 34.6°, and 0.0°) the edge spread function is determined by summing up along the arrows. **c,** Edge spread function of the knife edge for an angle of 34.6° determined by summing up along the arrow. **d,** Line spread function calculated by differentiating the edge spread function. The MTF can be determined by Fourier transformation.

This can be also seen in the images of the sharp edge in Fig. 7.5. The modulation transfer function is determined by imaging the sharp edge of a razor blade by the lenses and a 50x objective (Nikon CFI LU Plan BD ELWD 50x) at various positions and with different orientations (7.5). The image was taken by a CCD sensor (GC 2450C, Allied Vision Technologies). The images are analyzed by summing up the edge spread function over a certain image region indicated by the small arrows in Fig. 7.5. Even in the images of the razor blade the improvement of the imaging quality is clearly visible. In order to get a better image contrast we use a median filtering for the illustration of the knife edge images. The obtained values are unaffected. The median filter only removes the salt-and-pepper noise originating from long exposure times.

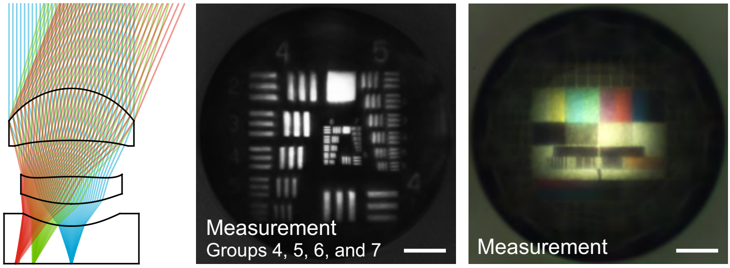

Figure 7.6. Performance measurement of a triplet lens system using 1951 USAF resolution test chart and Telefunken FuBK test card. Ray tracing design of a triplet lens system optimized within ZEMAX (left); image of the 1951 USAF resolution test chart (groups 4, 5, 6, and 7) taken through the triplet lens system at a distance of 1 mm behind the lens (center), and image of the Telefunken FuBK test card at a distance of 20 mm (right). Scale bars, 20 µm.

The quantitative optical performance of different doublet and triplet systems is further investigated by using different test charts. In Fig. 7.6 the imaging properties of a triplet lens system are analyzed. The left image shows the optical ray tracing design of the lens. The lens consists of five refractive interfaces, which are all of aspheric shape. The field of view in the object space is designed to be 47°. The last surface is attached to a 170 µm substrate, on which the lens is fabricated. Using the 1951 USAF

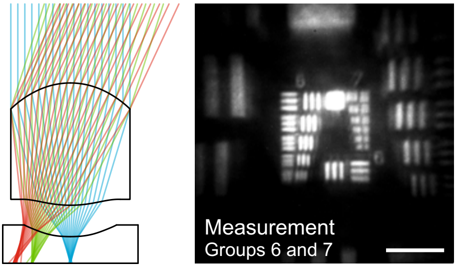

Figure 7.7. Performance measurement of a doublet lens system using 1951 USAF resolution test chart and Telefunken FuBK test card. Ray tracing design of a doublet lens system (left) and image of the 1951 USAF resolution test chart at a distance of 1 mm behind the lens (right). The three bars in group 6, element 5 corresponding to 101.6 lp/mm are clearly visible. Scale bar, 10 µm.

resolution test chart we achieve a maximal resolution of 128 line pairs/mm, which corresponds to the element 1 of group 7 of the test chart (center image of Fig. 7.6). Further details to resolution and the test pattern can be found in Chapter B. The 3D printed optical system and the resolution chart are separated by a distance of around 1 mm. The color fidelity is investigated by a Telefunken FuBK test card in the right image of Fig. 7.6. The image exhibits a yellowish hue, which is caused by remaining photo initiator in the lens material. By adjusting the color balance of the CMOS sensor the color distortion can be eliminated.

In Fig. 7.7 the performance measurement of a doublet lens system with three refractive surfaces is depicted. On the left-hand side the optical design optimized within the optical design software ZEMAX is shown. The lens is designed to have a field of view in the object space of 50° and a diameter of the imaging area of 100 µm. The measurement is displayed on the right-hand side. The optical performance is measured with a 1951 USAF resolution test chart at a distance of around 1 mm. In order to record the image a 100x objective lens is used. We achieve a resolving power of 101.6 line pairs/mm associated with element 5 of group 6 and corresponds to a line width of 4.92 µm in the 1951 USAF resolution test chart. More details of the 1951 USAF resolution test

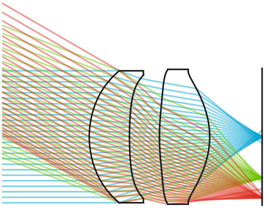

Figure 7.8. Ray tracing design of a doublet lens system with four refractive surfaces optimized within ZEMAX. The two lens elements are mounted in a shell, which axially and laterally aligns the individual compontents. The field of view is 60°

chart can be found in Chapter B in the appendix. Due to chromatic aberrations, the images appear blurry. In Fig. 7.8a doublet lens system with four refractive interfaces is shown. The optical system has a field of view in the object space of 60° and exhibits a meridional and sagittal modulation transfer function (MTF) of at least 195 lp/mm for a 10 % modulation contrast over the complete field of view.

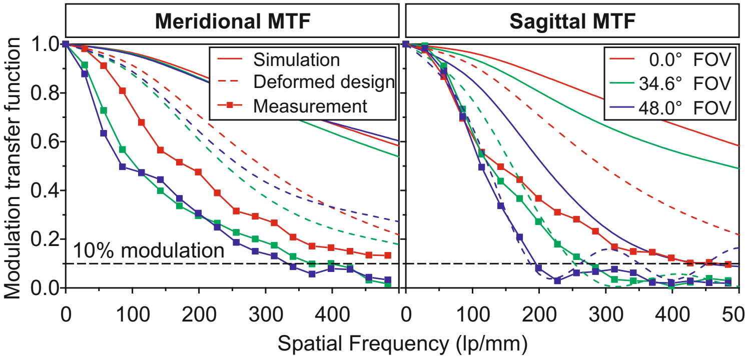

Figure 7.9. Performance measurement using knife edge methodology in order to determine the modulation transfer function (MTF). Simulation and measurement of the meridional and sagittal modulation transfer function (MTF) for different angles and for the doublet lens system of Fig. 7.8.

Figure 7.9 shows the curves of the MTF measurements, which are measured using a knife edge method [106, 107, 108, 109]. For small angles resolving powers of more than 400 lp/mm are achieved. Compared to wafer-level objective lenses [20, 19] fabricated by micro imprint technology with edge lengths of 500 µm [110] our 3D printed compound lenses show better resolving powers and considerably higher fields of view of up to 80° in object space.

Due to an alleged non-uniform shrinkage of the photoresist during the fabrication and development process, the final shape of the optical system is not perfectly as designed, which might be the source of the deviation between measurement and simulation. Therefore, in a first approximation we additionally plot a simulation of the MTF (dashed lines in Fig. 7.9), where the radius of curvature part of the aspheric surface shape is shrunken by 8 %. This corresponds to an axial deviation of roughly 2 µm in a radial distance of 50 µm for a radius of curvature of 80 µm. The simulation shows that the origin of the deviations can be partly explained by a shrinkage of the 3D printed lenses. The sagittal MTF shows better agreements between experiment and simulation than the meridional MTF. These hints point into the direction of an anisotropic shrinking process. Details and dependence on exposure and writing condition will be investigated in the future. Furthermore, uncertainties of material properties as well as material inhomogeneities might lead to deviating simulation results, which predict modulation depths of up to 0.5 at 500 lp/mm for the doublet lens system of Fig. 7.8.

Figure 7.10 shows details of the MTF measurements. The images are analyzed by summing up the edge spread function over a certain image region indicated by the small arrows in Fig. 7.10a and 7.10b. The averaged edge spread function in Fig. 7.10c is differentiated in order to obtain the line spread function in Fig. 7.10d, which is again Fourier transformed to receive the MTF presented in Fig. 7.9. In Fig. 7.10c and 7.10d the procedure is shown based on the image, where the edge is at an angle of 34.6°.

A throughfocus MTF scan is depicted in Fig. 7.11. We remeasure the MTF in different focal planes with z-offsets from

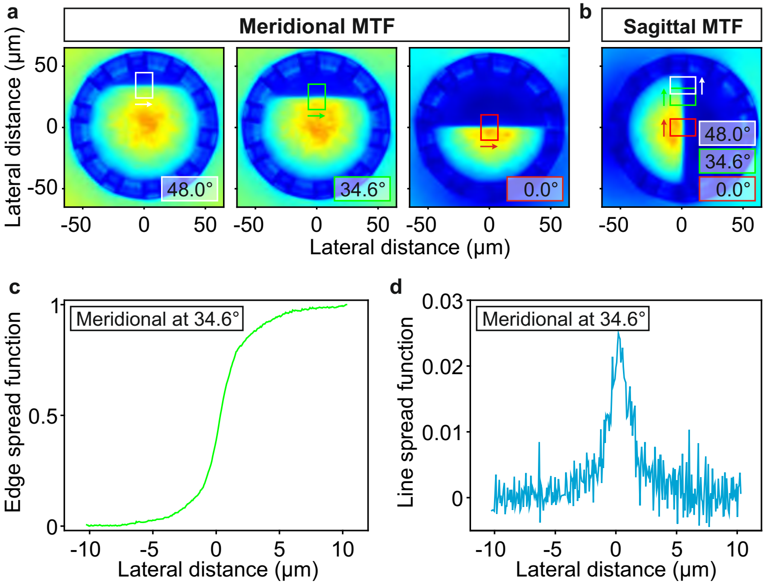

Figure 7.10. Knife edge measurement methodology in order to determine the modulation transfer function (MTF) shown in Fig. 7.8. **a,** Images of the knife edge for the calculation of the edge spread function in the meridional plane. For the different fields of view (48.0°, 34.6°, and 0.0°) the edge spread function is determined by summing up along the arrows. **b,** Images of the knife edge for the calculation of the edge spread function in the sagittal plane. For the different fields of view (48.0°, 34.6°, and 0.0°) the edge spread function is determined by summing up along the arrows. **c,** Edge spread function of the knife edge for an angle of 34.6° determined by summing up along the arrow. **d,** Line spread function calculated by differentiating the edge spread function. The MTF can be determined by Fourier transformation.

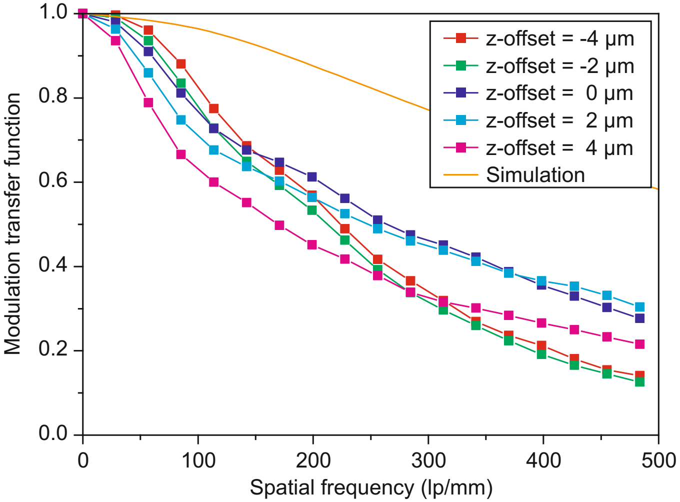

Figure 7.11. Throughfocus modulation transfer function scan (MTF scan). The MTF scan is created by measuring the MTF at different focus planes with z-offsets from −4 µm to −4 µm. The MTF measurement is carried out for the doublet lens system introduced in Fig. 7.8.

−4 µm to −4 µm. The different z-positions show nearly no influence on the MTF behavior. At each position a strong modulation of more than 10 % can be seen for resolving powers of ⩽500 line pairs per millimeter. In general from this curves effects such as astigmatism, defocusing, field curvature, and spherical and chromatic aberrations can be determined [106].

We also measured the MTF curves by a slanted-edge method [107], where the edge of the razor blade is not parallel to the borders of the image. These measurements show similar measurement results.

Chromatic aberrations are analyzed for the singlet, doublet, and triplet lens system introduced in Fig. 7.2. 40 nm wide bandpass filters in the range from 450 nm to 850 nm are used for target illumination. By adjusting the focal position at each wavelength the image is sharpened and highest contrast is achieved.

Figure 7.12 depicts images of a test chart at different wavelengths from 450 nm to 850 nm at different focal positions. The

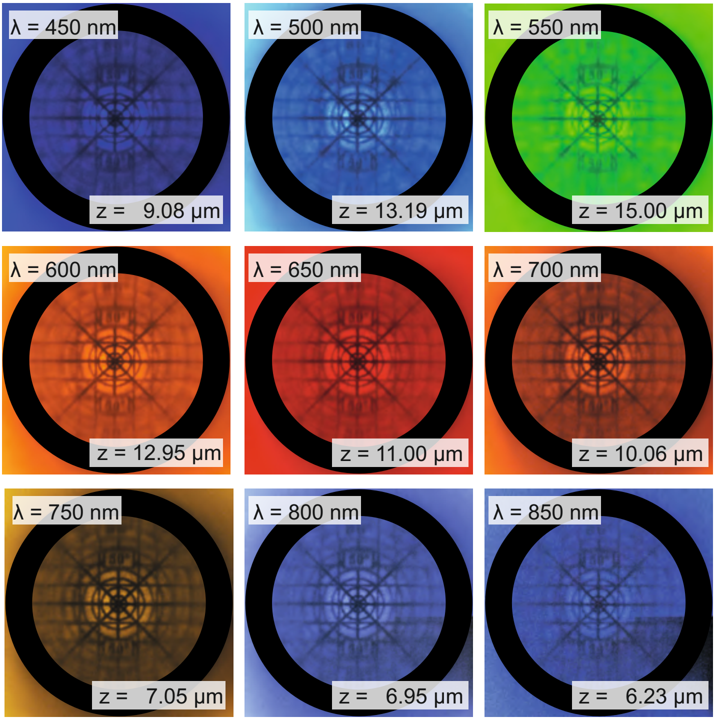

Figure 7.12. Measurement of the longitudinal (axial) chromatic aberration. Images of a test chart taken with the triplet lens system and a CCD camera in a wavelength range between 450 nm and 850 nm. A white light lamp with 40 nm wide bandpass filters is used for illumination. Each ring corresponds to 10° field of view (FOV). The outer ring corresponds to 80° FOV. High image contrasts up to 50° FOV are observed. The relative z-position of each image is chosen in order to obtain highest contrast. The distance between the target and the lens is 5 mm. The measurements are carried out for the triplet lens system of Fig. 7.2.

test chart is imaged by the triplet lens system introduced in Fig. 7.2. High image contrast can be observed up to 50° field of view (FOV). The test chart consists of concentric rings, which correspond to azimuthal angles of 10° field of view. The outer ring corresponds to 80° FOV in abject space, which agrees very well with the optical design (see Fig. 7.2). For more details in regard to the test pattern see Chapter B in the appendix.

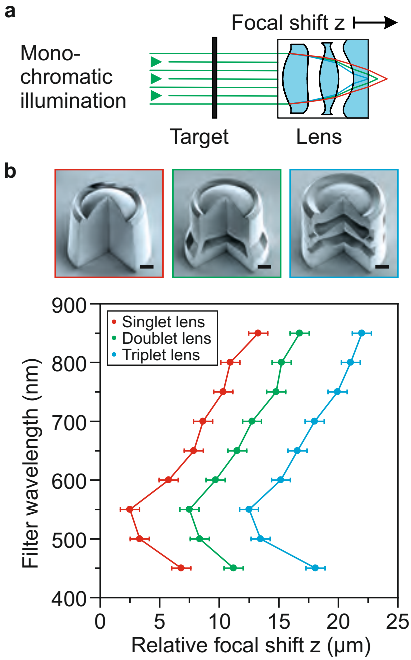

Figure 7.13. Measurement of the longitudinal (axial) chromatic aberration. Relative focal shift due to longitudinal chromatic aberration for the singlet, doublet, and triplet lens system introduced in Fig. 7.2 for different wavelengths. The curves are displaced horizontally by 5 µm relative to each other for better visibility.

Fig. 7.13 shows the measurement results of the longitudinal (axial) chromatic aberrations for the singlet, doublet, and triplet lens system. For better visibility, the curves are displaced by 5 µm relative to each other. All three lenses show the same chromatic aberration behavior. Due to dispersion effects in the lens material at each wavelength, the target is imaged onto a different focal plane and thus causes chromatic aberration. In order to avoid this effect a classical achromatic lens design consisting of two materials with different Abbe numbers can be used in the future. In this case, the direct laser writing process will be performed in two steps using different photosensitive materials.

In order to enhance the optical quality and thus the performance of our 3D printed compound lenses, additional post processing treatments can be applied. Anti-reflection coatings reduce stray light and improve the image contrast and efficiency. In order to accomplish this feat, atomic layer deposition (ALD), moth-eye based structures, or other surface treatments such as chemical roughening could be utilized. Additional optimization of the contour accuracy will further improve the performance. The designed target shape could be as well obtained by reducing the shrinkage of the photoresists during the fabrication process utilizing suitable polymers. Alternatively, adaption of the shape of the compound lens elements can compensate the shrinkage of the materials during development. In an iterative process, the deviation between lens design and real lens shape could be added to the designed surface shape and subsequently, the modified compound lens would be manufactured. This method could stepwise improve the contour fidelity and therefore enhance the optical performance. Also, by using a desensitized lens design, which is tolerant to small deformations of the design, improved optical quality can be obtained. More details can be found in Chapter 8.

In order to make the system integration capability of 3D printed ultra-compact compound lenses evident, we demonstrate direct manufacturing on image sensors and imaging fibers. Fig. 7.14a depicts several arrays of doublet lens systems with four refractive interfaces directly fabricated on an Omnivision 5647 CMOS image sensor. The doublet lens system with 60° FOV and a design f-number of 0.78 has already been introduced in Fig. 7.8. The 5-megapixel CMOS image sensor possesses a total active area of 2592 pixels × 1944 pixels. Each pixel has a size of $1.4 \times 1.4\,\mu\text{m}^2$. Before manufacturing, we remove the microlens

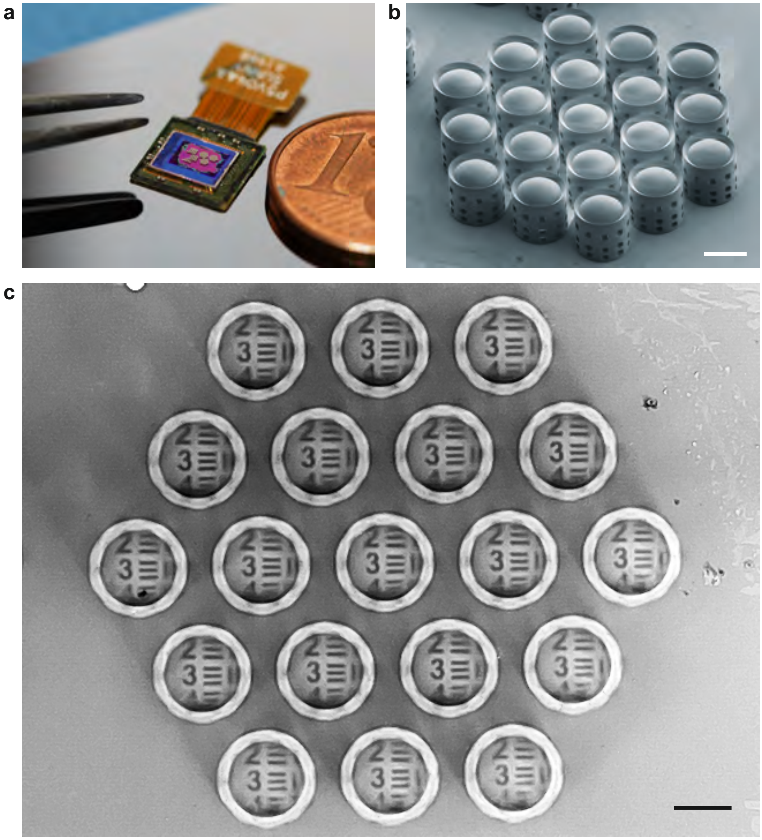

Figure 7.14. Regular arrangement of doublet lens systems directly fabricated on a CMOS image sensor. a, Photograph of an Omnivision 5647 CMOS image sensor with doublet lens systems. The CMOS-chip has a pixel size of 1.4 × 1.4 μm^2. **b,** Scanning electron microscope image of the hexagonal lens arrangement. Each doublet lens has a diameter of 120 µm and a height of 128 µm. Scale bar, 100 µm. **c,** Image of a part of the 1951 USAF resolution test chart at a distance of 30 mm taken through a hexagonal lens arrangement. The elements are of group -2. The image section consists of 640 pixels × 480 pixels. Scale bar, 70 µm = 50 pixel.

layer and color filter. Additional information to the pretreatments and fabrication can be found in Chapter 2. In Fig. 7.14b a scanning electron microscope image of a hexagonal arrangement of 19 printed doublet lens systems is shown. Each individual lens shows uniformly high quality and performs very similarly to neighboring lenses. Image acquisitions confirm the optical quality. Fig. 7.14c depicts the image of a part of the 1951 USAF resolution test chart taken through a hexagonal lens arrangement. The image part has a size of 640 pixels × 480 pixels and the chart is at a distance of 30 mm. The numbers and lines of elements of group -2 can be clearly distinguished. Each lens has a diameter of 120 µm and an imaging area with a diameter of around 100 µm. This area contains about 4000 pixels. Each doublet lens system images with the same performance as its neighboring one. This proves that femtosecond direct laser writing is extremely well suited for the reliable and reproducible fabrication of multiple identical or different 3D printed micro-optics even on large sensor areas.

High quality and high acceptance angle Shack-Hartmann wavefront sensors consisting of a regular arrangement of multi-lens systems can be fabricated as well. Fig. 7.15 shows a hexagonal array of triplet lenses, shown in Fig. 7.2. In comparison, Fig. 7.14 shows an arrangement of doublet lens systems. An array of high quality micro-lenses will allow for the simultaneous measurement of the wavefront and the image using only a single compact CCD or CMOS sensor. The superior performance will allow for rapid prototyping and production of small and medium numbers of integrated micro-optical devices, well suited for a plethora of applications.

An endoscopic application on the micrometer scale can be realized by using an imaging fiber with a total outer diameter of only 210 µm. To this end, we directly manufacture a triplet lens system with five refractive interfaces on the end facet of the fiber. The triplet lens system has already been introduced in Fig. 7.2. Fig. 7.16a depicts a microscope side view of the micro-optical lens system.

For the writing process the triplet lens system is centered by illuminating the opposite end facet and aligning with respect to

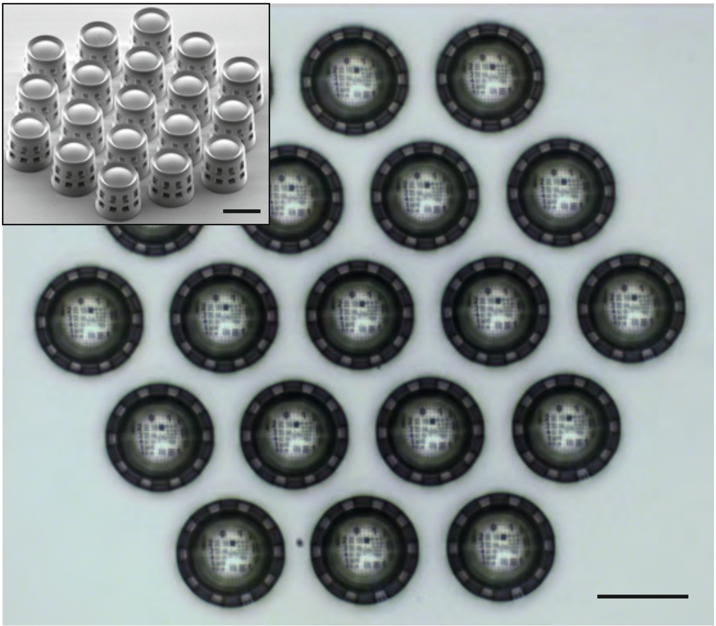

Figure 7.15. 1951 USAF resolution test chart image taken through a hexagonal arrangement of 19 triplet lenses introduced in Fig. 7.2. 19 triplet lenses arranged in a hexagonal pattern can be used as a Shack-Hartmann wavefront sensor. Each lens is fabricated with a layer-by-layer distance of 400 nm. The distance between 1951 USAF resolution test chart and triplet lens array is 20 mm. As inset a scanning electron microscope image of the lens arrangement is depicted. In comparison, Fig. 7.14 shows an array and the imaging properties of doublet lens systems. Scale bars, 100 µm.

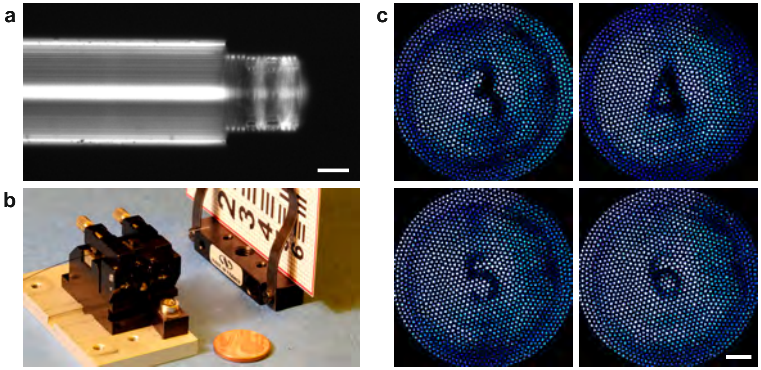

Figure 7.16. triplet lens system directly fabricated on an imaging fiber with 1600 single mode cores of 4 µm diameter each. a, Microscope image of the side view of the triplet lens system introduced in Fig. 7.2. Scale bar, 50 µm. **b,** Measurement setup. **c,** Image of a part of the 1951 USAF resolution test chart through a 170 cm long fiber piece of an imaging fiber with 1.600 pixels. The numbers are the labels of the elements of group 0. The distance between fiber end facet and test chart is 3 mm. Scale bar, 20 µm.

the writing beam. The fabrication section in Chapter 2 contains more details on the fabrication process. Fig. 7.16b depicts the setup, which is used for the measurement of the optical performance. The opposite fiber end facet is then imaged using an optical microscope with a 50x objective (NA = 0.55). The active area of the fiber has a diameter of 145 µm, whereas the 3D printed objective provides an imaging area with a diameter of 100 µm. Thus, right now not the complete fiber area is utilized for transmitting the images. 45 % of the active fiber area transfer the image along the 170 cm long fiber piece. This area contains roughly 700 pixels. As each pixel has a pixel diameter of 4 µm the resolution is limited by this specific fiber geometry. Fig. 7.16c displays the images of a small section of the 1951 USAF resolution test chart. The labels of the elements 3 to 6 of group 0 are clearly recognizable. As an example the number 6 (bottom right) of group 0 has a height of about 1.6 mm. The test target is mounted at a distance of 3 mm after the fiber end facet, resembling typical endoscopic situations in medical imaging.

The images are modified by enhancing the contrast and adjusting the brightness, except the images which are used for the calculation of the MTF. Some images are converted from a true color image in a grayscale intensity image in order to remove the color cast.

7.2 MULTI-LENS SYSTEMS FOR BEAM SHAPING

High intensity illumination over a large area can be of great advantage in inspection and medical endoscopy. Fiber based illumination enables easy positioning for numerous applications without the nood for complex mounting systems. In addition, it allows for multiple illumination sources by using only one single light source.

As in endoscopic applications there usually is a lack of space, fiber bases illumination system have numerous advantages. Unfortunately, optical fibers do not offer a homogenous illumination. There is a natural intensity dropoff, which can only be compensate by complex optics. Thus, we present an optical single mode fiber equipped with an ultra-compact beam shaping lens.

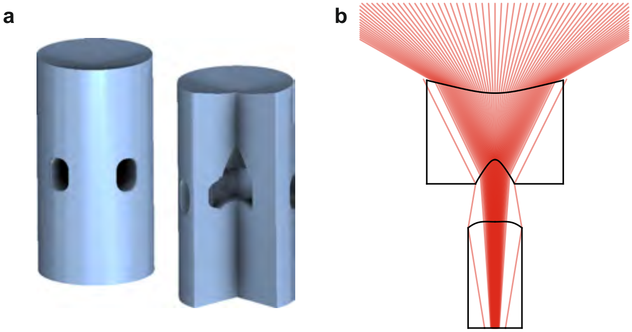

Figure 7.17. Design of a 120°-beam shaper consisting of two lenses. a, Illustration of the doublet lens system. **b,** Ray tracing design of the doublet lens system with three refractive surfaces optimized within ZEMAX.

Figure 7.17a depicts an illustration of our doublet lens system. The lens consists of three refractive surfaces. In Fig. 7.17b the ray tracing design is shown. The doublet lens system is designed to illuminate a field of 120°, which corresponds to numerical aperture (NA) of 0.87. The pure single mode fiber SMF-28, which is beneath our beam shaping doublet lens system has a NA of 0.09. This value corresponds to a NA of 0.14 determined at the 1 % intensity level.

The doublet lens system is directly fabricated by three-dimensional direct laser writing on the end facet of an optical single mode fiber SMF-28. The fiber core has a diameter of 8.2 µm.

Fig. 7.18 shows the fabricated beam shaping element on top of a single mode fiber. The lens has a height of 187 µm and a diameter of 100 µm.

We use fiber pieces of 15 - 20 cm length, which we subsequently equip with a fiber connector by splicing optical patch cables to our fiber pieces. This enables a wide field of applications, as the fiber pieces can be connected to different light sources.

As a light source we use a femto-second laser source, which we spectrally broaden by a tapered fiber. The laser operates at a wavelength of 1030 nm with a pulse duration of 170 fs at a repetition rate of 44 MHz. The tapered fiber piece has a length of 8 cm

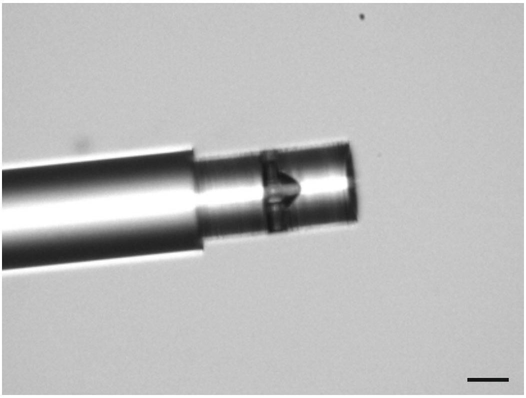

Figure 7.18. Microscope side view of a 120°-beam shaper with three refractive surfaces. The doublet lens system is directly fabricated on the end facet of a single mode fiber SMF-28 by two-photon direct laser writing. Scale bar, 50 µm.

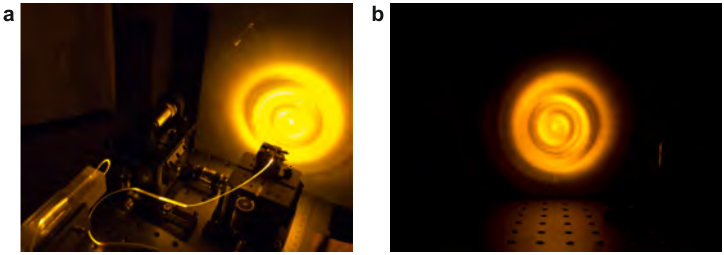

Figure 7.19. Photograph of the setup for measuring the intensity distribution of a 120°-beam shaper. a, Using a tapered fiber for white light generation we measured the intensity distribution on an opal diffusing observation screen. **b,** The through put is imaged with a Canon digital reflex camera equipped with a 18 - 135 mm objective lens.

and a diameter of 3.5 µm. The transition length is 1.5 cm. We used a 10x microscope objective to couple into the non-tapered fiber end. The opposite end is equipped with a fiber connector. A mating sleeve connects the tapered fiber and the fiber piece with the 120°-beam shaper.

Figure 7.19a shows an image of the setup. An opal diffusing observation screen is mounted at a distance of 50 mm behind the fiber end facet. The beam profile is monitored by a Canon digital reflex camera utilized with a 18 - 135 mm objective lens. For this purpose, the transmitted light through the opal diffusing observation screen is imaged. Fig. 7.19b depicts a typical image taken behind the screen.

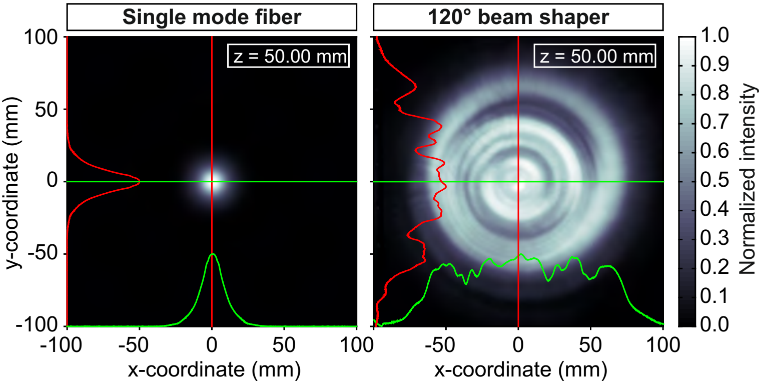

Figure 7.20. Intensity profile of single mode fiber and 120°-beam shaper. The intensity distribution is measured at a distance of 50 mm. We measure a beam diameter of 166.3 mm, which corresponds to a measured angle of 118.0° (diameter at $1/e^2$ intensity).

In Fig. 7.20 the measurement results of the beam shaping element in comparison to a pure fiber end facet are shown. The 120°-beam shaper creates an illumination over a large area. At a distance of 50 mm the beam diameter at the position, where the intensity is dropped down to $1/e^2$ is 166.3 mm. This corresponds to an angle of 118.0°. Due to surface inhomogeneities, the illumination is not perfectly symmetric. Apart from that, the intensity distribution shows an uniform illumination over a large area. Therefore, it is perfectly suited for illumination applications in medical and inspection endoscopy.

8

FABRICATION ISSUES

In order to fabricate high quality optics, which show excellent performance, different parameters influence the fabrication process. We check the influence of the laser power, the surface shape, and the lens material on the fidelity of the fabricated shape. Additionally, we try to optimize fabrication speed by writing only a photoresist filled scaffold, which is flash exposed by UV light after the fabrication process in order to get a homogeneous optical element. We also introduce the idea of fabricating a perfect lens by an iterative method.

All multi-lens devices presented in this chapter are fabricated layer-by-layer with a distance of 100 nm, unless specified otherwise. During the fabrication process the laser is laterally moved via galvanometric mirrors and ultra-precise piezo actuators execute the axial movement.

8.1 ADAPTATION OF THE MULTI-LENS SURFACE SHAPE

As shown in the previous chapters, there is an alleged non-uniform deformation during the fabrication and development process. This deformation leads to a strong deviation of the surface of the micro-optical element from the design and thus reduces the optical performance.

As the holes in the shell of our multi-lens system cause inhomogeneities during the fabrication, we improved our design by changing the size and position of the holes. In particular, the curved surface gets bumps and steps when there are strong changes in the geometry of the single layers. As the system has to calculate the new, more complex trajectory of the layer, there are short breaks in the fabrication process, which cause inhomogeneities in the surfaces. Therefore, we developed an *improved design*, which exhibit no holes at the vertical position of curved surfaces.

The optical design software ZEMAX allows for the integration and analysis of requirements. As our surfaces deform during the fabrication we develop a *desensitized design*. Here, the surfaces of the desensitized design are optimized to exhibit constant optical performance although there are slight deviations in the fabricated surface shape.

In addition, we modify the improved design by adding an offset to the radius of curvature in order to compensate the deformation. For this purpose, in the *modified design* we add roughly 1 µm as it is obtained by the circular top hat shaper (see Chapter 6.5).

Figure 8.1 shows a comparison between the initial design, the improved design, the desensitized design, and the modified design. All lenses are doublet lenses based on the initial design, which is the doublet lens shown in Fig. 7.8. They are fabricated with the aim to improve the optical performance. In Fig. 8.1a the USAF 1951 resolution test chart is imaged by the lenses. The target is at a distance of 20 mm behind the multi-lens systems. All images show comparable optical performance nearly without any deviations. The deviations can be explained by incorrectly adjusted focal positions. Fig. 8.1b shows the image of the sharp edge of a razor blade, which is once oriented along the x-axis and once along the y-axis. The USAF 1951 resolution target as well as the razor blade are imaged through the micro-lens system and a 50x objective (Nikon CFI LU Plan BD ELWD 50x) onto a CCD sensor (GC 2450C, Allied Vision Technologies).

The average of the modulation transfer function of both orientations is plotted in Fig. 8.1c. For the illumination a halogen lamp is used.

As shown in Fig. 8.1 all lenses show nearly the same optical performance. The lenses with the adapted surface shapes exhibit a stronger modulation for the low spatial frequencies, whereas for the higher spatial frequencies it is the other way round. As a whole, the modification of the surface shapes only have a weak influence, as there is only an improvement for the spatial frequencies blow 100 line pairs per millimeter.

These results further underline the stability and reproducibility of our method.

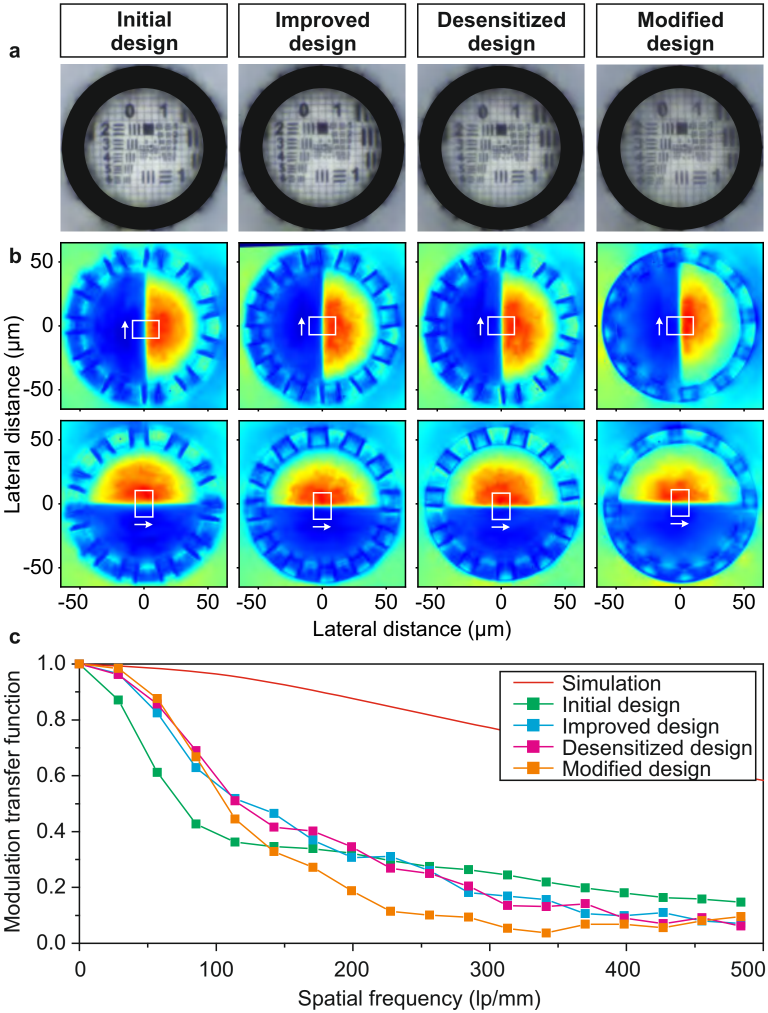

Figure 8.1. Comparison of a doublet lens, a improved version, a desensitized version and a modified version. a, Image of the USAF 1951 resolution test chart imaged by the different lenses. The distance between lens and target is 20 mm. **b,** Images of the knife edge for the calculation of the edge spread function. **c,** Simulation and measurement of the modulation transfer function (MTF) for the different lenses.

8.2 VARIATION OF THE WRITING PARAMETERS

As we use reflecting substrates, we sometimes have to reduce the power level in order to avoid overexposure. Overexposure results in bubbles and other inhomogeneities in the exposed photoresist and thus reduces the optical quality of our micro-optical systems.

Therefore, we check the influence of the laser power by decreasing it from our standard value of 42.5 % in two 5 % steps. The definition of 1 % laser power can be found in Chapter D in the appendix. Figure 8.2 shows the measurement results of the power series. We measure the resolution by test targets as well as the modulation transfer function (MTF) with increasing laser power for the fabrication. Values of 34.5 %, 38.5 %, and 42.5 % are used. As a micro-lens we used the doublet lens with four refractive surfaces introduced in Fig. 7.8. In Fig. 8.2a the USAF 1951 resolution test chart is imaged by the micro-optical lens and a 50x objective (Nikon CFI LU Plan BD ELWD 50x). The images are taken by a CCD sensor (GC 2450C, Allied Vision Technologies). All three images show nearly the same optical performance. Fig. 8.2b shows the images of the sharp edge used for the calculation of the MTF curves. The MTFs in Fig. 8.2c are obtained by taking the average of the MTF calculated by the two orientations.

As there is nearly no difference in the MTF curves, the influence on the optical performance by decreasing the power is negligible. The MTF measurements confirm the results obtained by the images of the USAF 1951 resolution test chart and knife edges in Fig. 8.2a and 8.2b. This proves that the photoresist IP-S has a wide power level range, in which it shows the same exposure behavior. Therefore, it is perfectly suited for the fabrication of high quality micro-optical devices on different substrate materials.

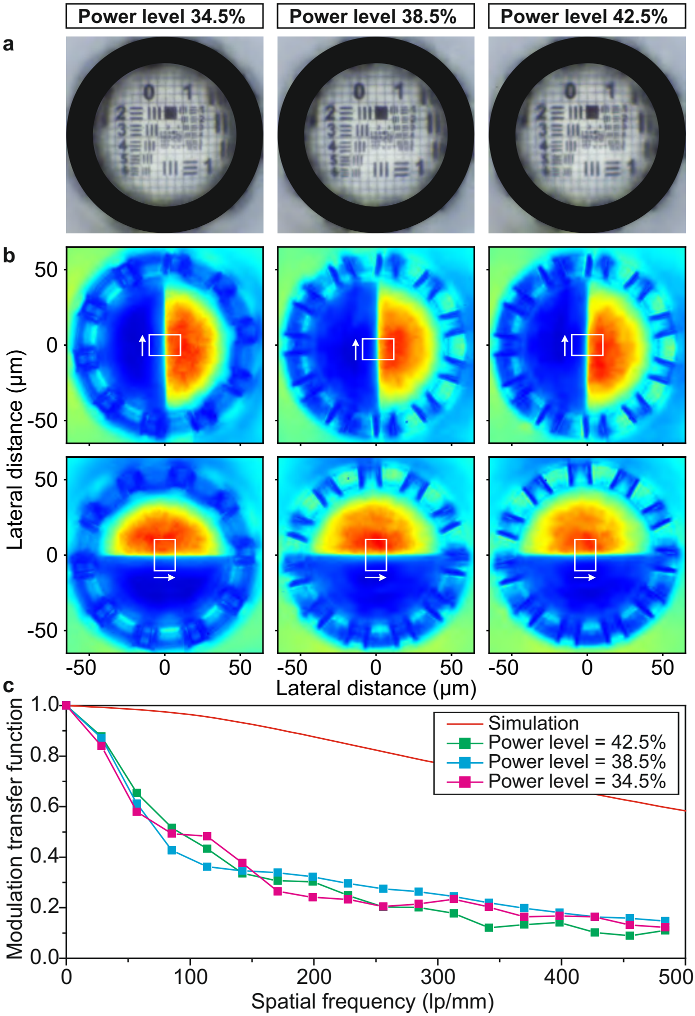

Figure 8.2. Comparison of doublet lenses fabricated with different laser powers. **a,** Images of the USAF 1951 resolution test chart at a distance of 20 mm. **b,** Images of a knife edge for the determination of the modulation transfer function (MTF). **c,** Simulation and measurement of the MTF for the different lenses.

8.3 VARIATION OF THE LENS MATERIAL

As aberration due to material dispersion can be avoided by using different materials in an achromatic design, we check the fabrication influences of the photoresist IP-Dip on the optical performance.

Usually, we use Nanoscribe IP-S in order to fabricate smooth refractive surfaces as it exhibits high proximity effects. Nanoscribe IP-Dip is used for the manufacturing of detailed structures and thus unsuitable for smooth surfaces, but terrific for diffractive structures.

In order to make an achromatic design an additional photoresist with different dispersion (see Chapter A in the appendix) is needed. Therefore, we check whether lenses fabricated out of Nanoscribe IP-Dip show the same performance than micro-lenses fabricated out of IP-S.

Figure 8.3a shows scanning electron microscope images of the two lenses. The lens design is adapted to the refractive index of the material. For IP-Dip we use a refractive index of 1.5495, for IP-S we use 1.513. This values are confirmed by refractive index measurements carried out by measuring the critical angle of total internal reflection at different wavelengths (see Chapter A). As a design we use a doublet lens with four refractive surfaces optimized within ZEMAX. The ray tracing design for IP-S was already introduced in Fig. 7.8.

Both lenses are fabricated layer-by-layer with the same layer distance of 100 nm. The difference in the optical performance are clearly visible in Fig. 8.3b, where the USAF 1951 resolution test chart is imaged using the two different lenses.

In Fig. 8.3c images of a razor blade in two orientations are shown. These images are used in order to calculate the modulation transfer function (MTF). In Fig. 8.3d MTF curves are obtained by taking the average of the two different orientations.

As IP-Dip is a high resolution photoresist there is no smooth surface, as it can also be seen in the scanning electron microscope images in Fig. 8.3a. Therefore, the MTF shows a weaker optical performance than the doublet lens fabricated out of IP-S. This proves that, although the layer distance and thus the steps in

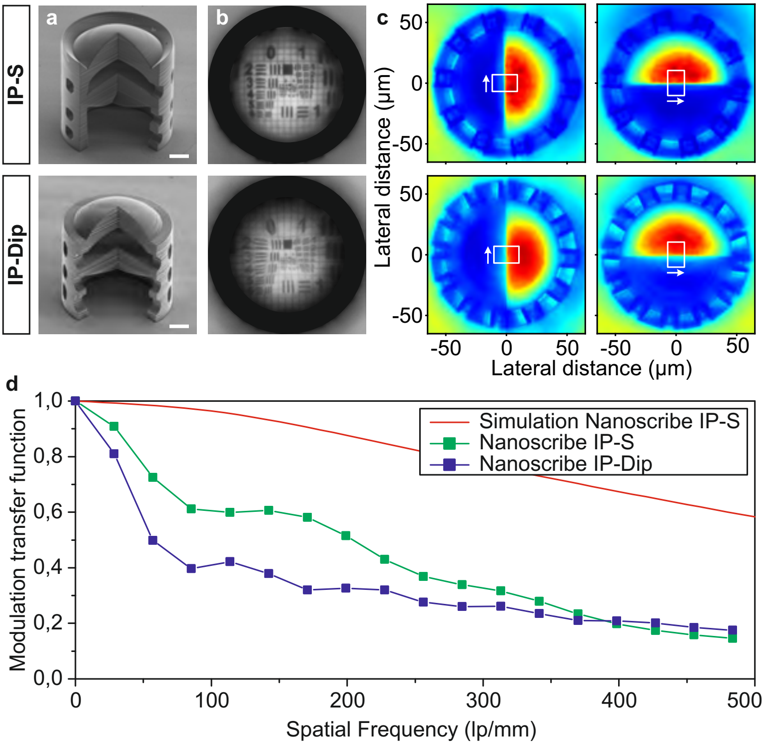

Figure 8.3. Comparison of doublet lenses made out of the photoresists IP-S and IP-Dip (Nanoscribe GmbH, Germany). a, Scanning electron microscope images of the doublet lenses. Scale bar: 25 µm. **b,** Recorded images of the USAF 1951 resolution test chart using a 50x microscope objective and a CCD camera. The distance between lens and target is 20 mm. **c,** Images of the knife edge for the calculation of the edge spread function. For different orientations the edge spread function is determined by summing up along the arrows. **d,** Simulation and measurement of the modulation transfer function for the different lenses. Each curve is determined by calculating the average of the two different orientations.

the refractive surfaces are way below the wavelength of the light, the high proximity effects of the photoresist IP-S plays a crucial role. However, we have to mention that for the fabrication two different kind of substrates are used in order to use the automatic interface finder. The substrate differ from each other in refractive index as well as thickness. Therefore, a slight difference in the performance can arise from the substrate material, although there are both high quality substrates.

The optical strain is as well analyzed by using two crossed polarizes. One is installed in front of the lens and one is installed behind the lens. Optical strain is only detected at the edges of the supporting shell, where the holes are. Additionally, there is a bright spot in the center of the image of the optical strain measurement with the crossed polarizes, which, we assume, is caused by the focusing behavior of our lenses and not by optical strain.

8.4 VARIATION OF THE WRITING MODES

As presented before, our lens are bulky and fabricated by exposing the complete structure by two-photon polymerization. In order to optimize fabrication time, there is the possibility to only manufacture an encasing shell and parts of the interior to serve as a scaffold.

In order to get a homogenous refractive index over the whole structure, in a second step, the structure is completely polymerized by an UV flash exposure process after fabrication and development. The shell structure prevents the developer to infiltrate the structure, which results in unexposed photoresist within the scaffold structure. By UV exposing the whole structure, it is completely polymerized and builds an optical homogenous structure.

We compare two different shell and scaffold parameter sets with the completely written structure. The two structures differ by shell thickness and wall thickness of the inner scaffold. On the one hand, we fabricate a structure with a *thin shell* with a thickness of 1.5 µm consisting of 10 contour lines and a scaffold structure consisting of 3 lines. The walls of the scaffold are separated by 20 µm. On the other hand, we fabricate a lens with a

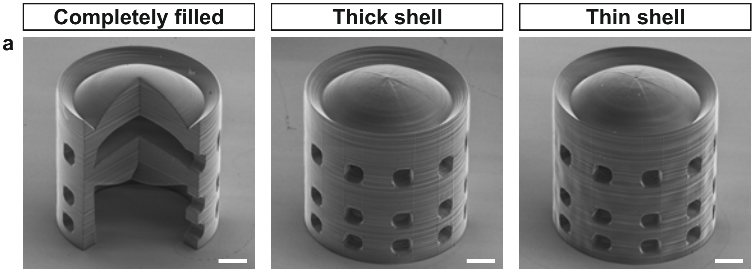

b

Slicing
Slicing mode: fixed
Distance: 0.1 µm

Filling
Hatching
Distance: 0.15 µm
Contour count: 0
Angle: 0°
Angle offset: 330°

Slicing
Slicing mode: fixed
Distance: 0.1 µm

Shell
Hatching
Distance: 0.15 µm
Contour count: 35
Base slice count: 65
Angle: 0°
Angle offset: 330°

Scaffold
Hatching
Distance: 0.15 µm
Type: Triangles
Wall spacing: 20 µm
Floor spacing: 25 µm
Wall line count: 1
Floor slice count: 1

Slicing
Slicing mode: fixed
Distance: 0.1 µm

Shell
Hatching
Distance: 0.15 µm
Contour count: 10
Base slice count: 10
Angle: 0°
Angle offset: 330°

Scaffold
Hatching
Distance: 0.15 µm
Type: Triangles
Wall spacing: 20 µm
Floor spacing: 25 µm
Wall line count: 3
Floor slice count: 3

Figure 8.4. Comparison of doublet lenses which are completely sliced or consists of a thick or a thin shell. After the development, in a post-processing step the unexposed photoresist is exposed by ultraviolet curing. a, Scanning electron microscope images of the doublet lenses. Scale bar: 25 µm. **b,** Parameters for the conversion of the stereolithographic file (stl format) into the Nanoscribe machine code (gwl format).

thick shell, where the shell thickness is 5.25 µm. The walls in the inner scaffold are again separated by 20 µm, but only consist of 1 line. The parameters of the slicing and hatching parameters for the conversion of the lens shape into trajectories are summarized in Fig. 8.4b.

As a lens design we use the doublet lens with four refractive surfaces, which was introduced in Chapter 7.1 and depicted in Fig. 7.8. Fig. 8.4a shows scanning electron microscope images of the fabricated structures.

For the fabrication of all compared lenses we use the same writing parameters (laser power and scan speed).

The *completely filled* structure (left image) shows a smooth surface. The two lenses fabricated by shell and scaffold show inhomogeneities on the surface that are obviously caused by the shells and walls of the scaffold. The measurement results of the lens with the *thick shell* is depicted in the central column and the results of the lens with the *thin shell* is shown in the left column.

The optical performances of the different lenses are shown in Fig. 8.5. In Fig. 8.5a the USAF 1951 resolution test chart is imaged by the lenses. Obviously, the completely filled micro-optic show a better performance than the lenses fabricated out of shell and scaffold. This is as well confirmed by the images of the sharp edge in Fig. 8.5b. Whereas there is only a small transition region in the case of the completely written lens, the other lenses show a broad transition region. The images of Fig. 8.5b are used to determine the edge spread function. In Fig. 8.5c the simulation and measurements of the MTF for the three lenses are shown. Each curve is determined by calculating the average of the two different orientations, depicted in Fig. 8.5b.

As already seen in Fig. 8.5a, there is a tremendous difference in the optical performance of the lenses. The completely filled multi-lens device shows high optical quality with a modulation of 10 % up to a spatial frequency of above 500 lines per millimeter (lp/mm). The two lenses which we manufactured out of shell and scaffold show nearly the same modulation transfer function with a modulation of up to 350 lp/mm at a 10 % threshold. Therefore, the writing mode by itself has an influence on the optical performance, but the shell thickness and wall thickness of the

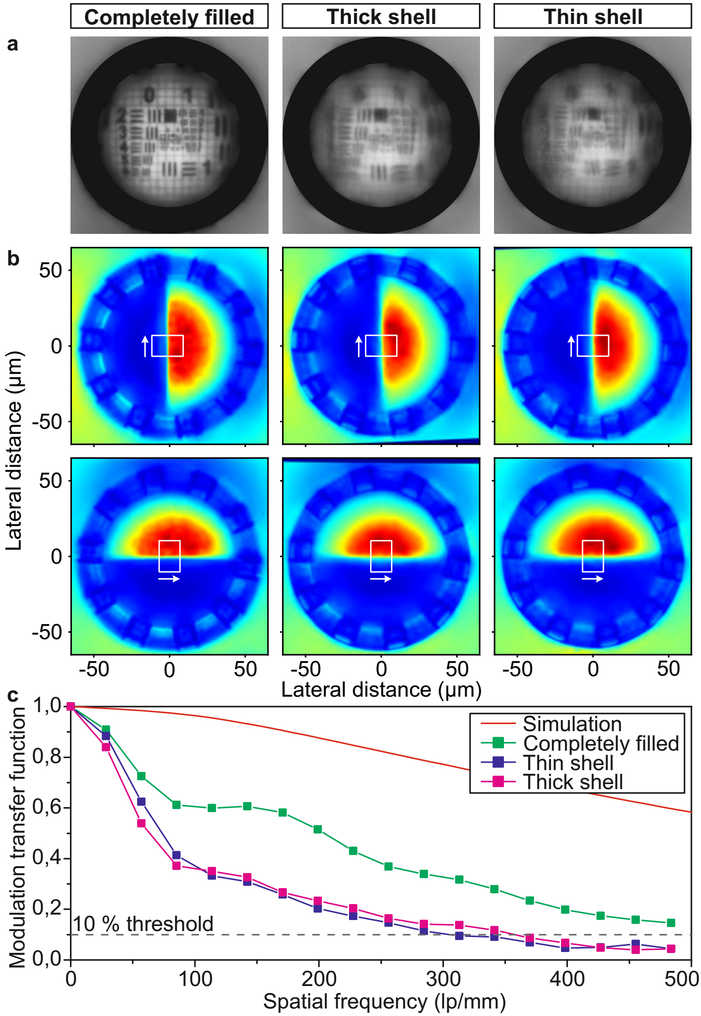

Figure 8.5. Comparison of doublet lenses, which are completely filled and consist of a thick and a thin shell. **a,** Images of the USAF 1951 resolution test chart. **b,** Images of a knife edge for the calculation of the modulation transfer function (MTF). **c,** Simulation and measurement of the modulation transfer function (MTF) for the different lenses.

inner scaffold have nearly no influence - at least for the two parameter sets. In contrast, the imaging quality of the doublet lens with the thick walls analyzed by recording the 1951 USAF resolution test chart (see Fig. 8.5a) shows a slightly better performance.

As seen in the SEM images of the three lenses in Fig. 8.4a the surface contains the substructure of shell scaffold writing, which causes a decline in the optical quality. By adapting the parameters of shell and walls, the inhomogeneities on the surface can be removed and a smooth surface can be created.

In addition, an uncleared issue is, whether there is a difference in the refractive indices of photoresists exposed by two-photon absorption or by UV light. If this is the case, there is an additional reason for the differences in the optical performance.

As the fabrication time of micro-optical devices with heights of $\leqslant 200\,\mu\text{m}$ and diameters of $\leqslant 200\,\mu\text{m}$ cannot be tremendously reduced by writing shell and scaffold, the shell writing mode does not bring any advantages. The fabrication time of the completely filled lens is 1 h 17 min, the lens with the thin shell takes 41 min, and the lens with the thick shell takes 1 h 20 min. The longer fabrication time of the thick shell is caused by computing time of the Nanoscribe system.

8.5 ITERATIVE METHOD FOR IMPROVEMENT OF THE SHAPE FIDELITY

According to our experience, the shrinkage or deformation of ″bulky″ objects consisting of layer-by-layer written photoresists is not uniform, as it depends on too many parameters, such as the photosensitive material, the writing parameters, and the shape by itself. Therefore, a prediction of the deformation is still difficult to make, especially for complex surfaces.

In order to improve the shape fidelity of direct laser written structures, we tried an iterative algorithm.

We calculate the initial surface shape of a circular uniform intensity shaping micro-lens introduced in Chapter 6.5 by numerically solving the Huygens-Fresnel diffraction integral. As a light source a laser diode with a wavelength of 808 nm is coupled into a single mode fiber SM 780HP. The beam waist of the Gaussian beam at the fiber end facet is w_0 = 2.45 µm and is obtained by mode theory. The refractive indices for the calculation are 1.4598 and 1.4537 for core and cladding material of the fiber. The core diameter of the SM 780HP is 4.4 µm. The intensity distribution is calculated on an observation screen at 20 cm distance.

The micro-optical beam shapers are fabricated using dip-in laser lithography with the photoresist Nanoscribe IP-S. The lenses have a height of 300 µm and a diameter of 120 µm. In order to save fabrication time the lens are separated into two parts. The lower part is fabricated with high laser power and a layer distance of 400 nm, the upper part, which mainly causes the shaping of the intensity distribution, is fabricated with a layer distance of 50 nm. The small layer distance is in order to get a smooth and accurate surface.

Figure 8.6 illustrates the iterative algorithm. In a first step the surface of the top hat intensity shaper is calculated by an iterative algorithm, which numerically solves the Huygens-Fresnel integral. After fabrication the intensity distribution is measured at a distance of 20 cm using a CCD camera. The measured intensity profile is used in a second step as a target distribution for the iterative Huygens-Fresnel algorithm in order to get the real surface. The deviation between designed and backward calculated surface is added to the lens design and again manufactured. In further steps, the measured intensity profiles can be used as target intensity distributions in our Huygens-Fresnel diffraction calculations in order to calculate the fabricated structure. The designed structure can be adapted and again, the improved surface shape can be fabricated.

Figure 8.6 shows the improvement of the intensity distribution and the surface shapes for the first three iterations. The improvement is clearly visible, however, there are more steps necessary in order to create a uniform intensity distribution.
Additionally, one has to consider that imperfections in the fabrication extend the process, as shown in the measured intensity profile of "Step 3" in Fig. 8.6.

As the non-uniform deformation is dependent on the surface shape by itself, the photoresist, and writing parameters, the iterative process only leads to the adaption of one single design.

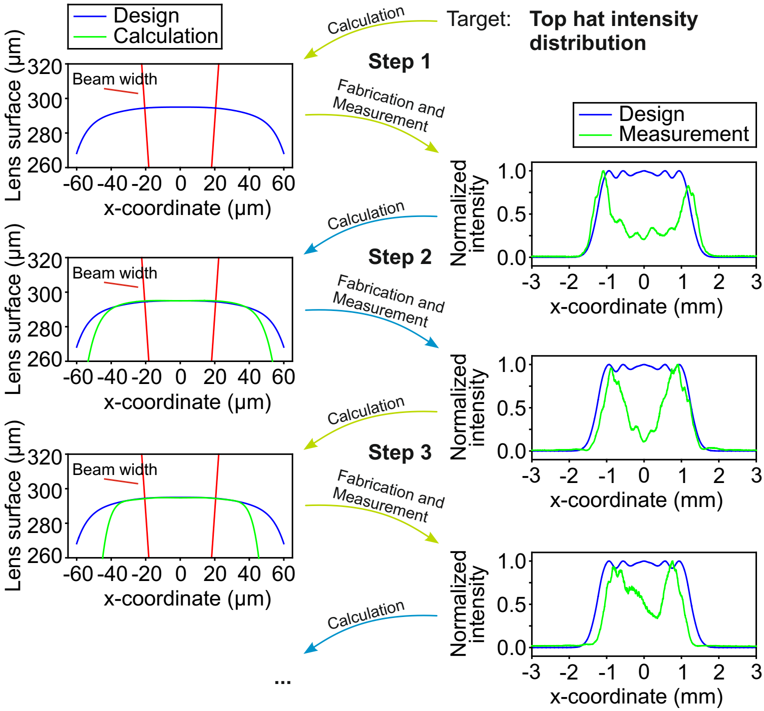

Figure 8.6. Iterative method for improvement of the shape fidelity. In a first step, the designed surface is determined by an iterative optimization algorithm using the Huygens-Fresnel principle. A circular top hat intensity distribution is used as a target. After fabrication the intensity profile is measured and compared to the target distribution. The measured intensity distribution is used as a target in a second step in order to get the fabricated surface shape and thus the deviation. By adding the deviation to designed surface shape the obtained intensity distribution is improved. Using this procedure in an iterative algorithm the surface and therefore the intensity distribution is improved.

Therefore, this approach is not convenient for the fabrication of prototypes and demonstrators.

As this process needs many steps in order to fabricate the designed structure, we decided to use another approach in Chapter 6.5. There, we check the influence of different simulation parameters on the shaped intensity profile. As the beam waist influences the intensity profile most, we changed the beam waist from the calculated value of 2.45 µm to 3.0 µm, which results in a fabricated surface shape that creates a uniform intensity distribution over a circular area. The simulation results as well as the measurement have been already shown in Chapter 6.5.

CONCLUSION

We have demonstrated a diversity of optical elements with submicrometer accuracy, enabling intensity distribution shaping, high quality imaging, and polarization control.

We have shown, that femtosecond direct laser writing allows for the fabrication of ultra-compact optics with numerous features, which makes unprecedented performance and incredible design freedom possible. Our optics have diameters from a few micrometer up to 120 µm and heights between a few nanometers and 300 µm with sub-micrometer resolution.

We have introduced a novel fabrication platform for numerous optical elements based on diffraction, reflection, and refraction in the micrometer region. Our novel concept which overcomes many existing difficulties of micro-optical fabrication opens the new field of 3D printed micro- and nano-optics with complex free-form lens designs. Our method gives sub-micrometer accuracy and excellent reproducibility. It allows for the fast and reliable transfer from design and simulations to high-performance 3D printed optics. Our approach creates a completely new approach for the fabrication of optical lens systems on the micrometer scale with a plethora of applications in numerous fields, which were previously unthinkable.

We have proved that the capabilities of additive manufacturing can be used for the fabrication of high quality micro- and nanooptical elements. Consequently, our method allows for complex free-form optics with numerous surfaces and features, which show high optical performance and tremendous compactness by at least one order of magnitude smaller than current approaches.

We have fabricated refractive optics for beam collimation and beam shaping applications. 3D printed diffractive optical elements exhibit sub-micrometer feature sizes and enable spatial intensity shaping. Additionally, chiral photonic crystals for polarization control have been manufactured. All elements are perfectly centered on the cores of optical fibers. Three-dimensional

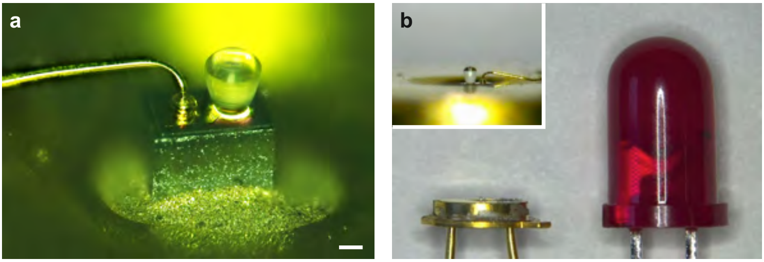

Figure 8.7. Refractive free-form micro-optic fabricated on a light emitting diode (LED). a, Microscope image of a compound parabolic concentrator on a point source LED. Scale bar, 50 µm. **b,** Comparison between our free-form micro-optic fabricated by dip-in two-photon direct laser writing and a conventional LED.

direct laser writing is as well an excellent tool for the fabrication of complex multi-lens optical systems that show high quality imaging.

We have determined the fabrication accuracy of our optics by analyzing imaging quality and intensity shaping behavior, as well as characterizing the surfaces by atomic force microscope and interferometric measurements. Manufacturing of imaging, ultra-compact micro-optics with a root mean square surface roughness of less than 15 nm is feasible, as we use photoresists with high proximity effects. Our 3D printed multi-lens systems feature resolving powers of up to 500 lp/mm and thus the printed micro-optical elements can achieve sufficient performance to enable compound lenses for high quality imaging.

We have verified our manufacturing method by varying different fabrication parameters and analyzing the influences on the optical performance.

As we have shown our approach of using three-dimensional dip-in laser lithography is not limited to any kind of special optic. Our concept is suitable for fiber technology, but at the same time it is as well applicable for the combination with other substrates such as light-emitting diodes (LEDs), vertical-external-cavity surface-emitting-lasers (VECSELs) and other light emitting structures in the sub-micrometer range.

Figure 8.7 shows a compound parabolic concentrator directly fabricated on a point source LED. Such micro-optical elements will supersede current optical systems that are restricted in size, shape, and dimensions by limitations of manufacturing.

Our method extends the realm of additive optical manufacturing into micro- and nanooptics and opens a new field for integrated fiber optical or complex lab-on-a-chip devices. Also, specific spatial modes and higher orbital angular momentum states in multimode fibers can easily be generated. Our unprecedented flexibility paves the road towards printed optical miniature instruments.

Therefore, our 3D printed optical elements allow for a completely new generation of ultra-compact optical elements in numerous fields of applications such as endoscopic instruments, miniaturized microscopes, novel illumination concepts, miniature optical fiber traps, and ultra-compact optical elements for high-quality imaging directly on image sensors.

OUTLOOK

Our novel concept opens the field of complex 3D printed micro- and nano-optics and thus provides a basis for a plethora of improvements, applications, and adaptions.

As we have shown the simulations of our structures promise even better optical performance than the ones we have shown. In order to achieve these, the well known concepts for the improvement of conventional objective lenses can be adapted. Functional structures such as optically opaque housings and apertures can bring tremendous improvements to our ultra-compact imaging systems.

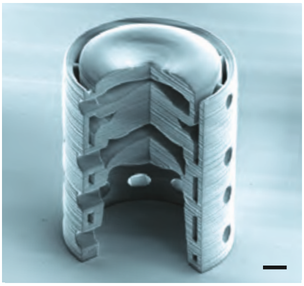

Figure 8.8. Triplet lens with aperture and optically opaque housing. Using dip-in two-photon direct laser writing we fabricate triplet lenses with micro-channels, which can be subsequently filled by ink to generate apertures and housing. Scale bar, 20 µm.

Figure 8.8 shows a triplet lens with micro-channels, which can be filled with an optically opaque ink after the development process creating apertures and housing. As stray light is suppressed, the optical performance can be improved. Inked photosensitive materials might as well allow for the fabrication of apertures in order to increase the contrast and focus depth of the imaging system.

An additional antireflection coating generated by atomic layer deposition (ALD), moth-eye based structures [42], or other surface treatments will further enhance the optical performance. In order to remove back reflections at the interfaces of conventional optics anti reflection coatings are used. Moth-eye based structures can be directly fabricated on optical surfaces by two-photon direct laser writing [111]. Fig. 8.9 shows such a moth-eye subwavelength structure with a periodicity of 550 nm.

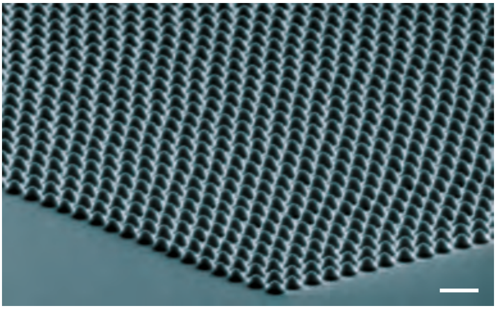

Figure 8.9. Moth-eye based structure as anti reflexion coating. Using dip-in two-photon direct laser writing we fabricated a moth-eye based structure, which can serve as an antireflection coating in order to improve the imaging quality of multi-lens micro-optical system even further. Scale bar, 1 µm.

Optical hybrid systems consisting of a combination of refractive, diffractive, and reflective elements can be easily manufactured by femtosecond direct laser writing and might allow for a new kind of ultra-compact hybrid systems.

Combining different optical materials will prospectively compensate chromatic and spherical aberrations in achromatic lens designs. They are fabricated out of materials with different dispersion behavior by 3D printing and thus allow for optimization of the designed lens systems for different wavelengths. In this case, the direct laser writing process will be performed by using different photosensitive materials in separate fabrication steps. Alternatively, achromatic correction can be achieved by combining refractive and diffractive surfaces.

Additional improvements of the surface of direct laser written refractive micro-optics can be obtained by surface treatments for smoothing via chemical or reactive ion beam etching.

Our approach of using dip-in laser lithography is not limited to any size. Therefore, the up- as well as down-scaling of our multi-lens systems is easily feasible. In future, direct laser written complex compound optics may replace current micro-optical singlet lenses with diameters up to 1 mm. Further expanding the scope of our optics, catadioptrical system designs can take the advantage of reducing chromatic aberrations and at the same time reduce the size of the optical system even more.

As application in Chapter 7.1, we introduced miniaturized endoscopes on the base of optical imaging fibers, which scale present endoscopes down by a factor of at least 3 (see Fig. 7.16 in Chapter 7.1). However, among this application our approach can be used for numerous other applications in different fields.

For example, our multi-lens devices can be used for the improvement of the collection efficiency of single photon sources. To this end, our lenses can be directly fabricated on structures such as nitrogen-vacancy centers (NV centers) [112, 113] or quantum dots in the respective host material [114]. We have already fabricated our lenses onto a semiconductor substrate with embedded quantum emitters. The spectrally integrated intensity of the exciton emission was increased by 25 % by adding doublet or triplet lenses to quantum dots.

Using active materials such as switchable materials [115, 116], pressure [117] or fluids [118, 119, 120] in micro channels, static multi-lens systems can be converted into flexible zoom lenses and thus adjustable focii would become possible.

In future, free-moving mini-cameras might be used for the three-dimensional imaging of the interior of a hollow organ or cavity of the body or as imaging systems carried by the wind for monitoring. Figure 8.10 illustrates the application of clusters of cameras with sizes not bigger than a grain of salt. Image sensors with included memory or transmission unit and power supply will be manufactured with sizes well below 1 mm. These mini camera systems can be attached to chutes, as known from "blow-

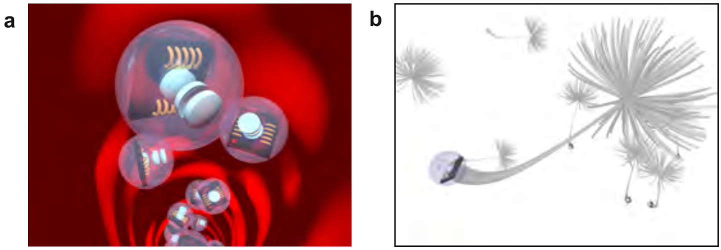

Figure 8.10. Examples for applications of free-moving mini-cameras with sizes well below 1 mm. a, The mini camera systems can be used for monitoring the human body. All images taken during traveling through the body can be assembled to one three-dimensional image of the interior. **b,** Attached to chutes, as known from ″blowballs″ the multi-lens camera devices can be carried by the wind and observe the surrounding.

balls″, carried by the wind and thus autonomically monitor the surrounding.

In addition, our approach of manufacturing multi-lens systems can be applied to the fabrication of optical tweezers and optical traps, directly attached to optical fibers, adding completely new degrees of freedom. As our systems only have diameters smaller than 200 µm trapped particles can be easily positioned and arranged with respect to one other. High numerical aperture objectives might be used on the end facet of optical fibers for trapping and positioning of the particles. The definition of the spatial intensity distribution shaped by diffractive or refractive optical elements can control and adjust the holding force of the particle.

Our technique is not limited to optical beam shaping and imaging system, it as well allows for manufacturing of deflection prisms or spectrometers, directly attached to image sensors.

Consequently, all-in-one sensors for the detection of multiple measurement parameters can be manufactured. Various multi-lens devices with different focal lengths, each with a specific polarization filter beneath and different field of view in combination with spectrometers, all printed onto an imaging sensor will allow for fast and intelligent optical sensors. Combined with light emitting diodes equipped with beam-shaping micro-optics these sensors can be assembled on a few square millimeter size and heights below 1 mm.

Two-photon direct laser writing of complex micro-optical devices represents a paradigm shift for the fabrication of nano-, micro-, and even larger optics. It allows for the development processes, from lens design, to production, testing, and the final working optical device in a few hours. Therefore, our concept pushes the on-going trend of miniaturization and fast development cycles forward and allows for a multitude of further adaptations, improvements and applications in various fields of applications.

A

REFRACTIVE INDEX MEASUREMENT

The dispersion of optical materials is an essential information for the design of high quality lens systems. For the used photosensitive materials of our work, we used a constant refractive index value. However, in order to improve the optical performance dispersion effects have to take into account.

As dispersion data of photosensitive materials are extremely rare we measure the refractive indices at different wavelength and determine the functional dependency. For this purpose, we measure the critical angle of total internal reflection of the used photoresists. In particular, Ormocomp (micro resist), IP-S (nanoscribe), and IP-Dip (Nanoscribe) are analyzed.

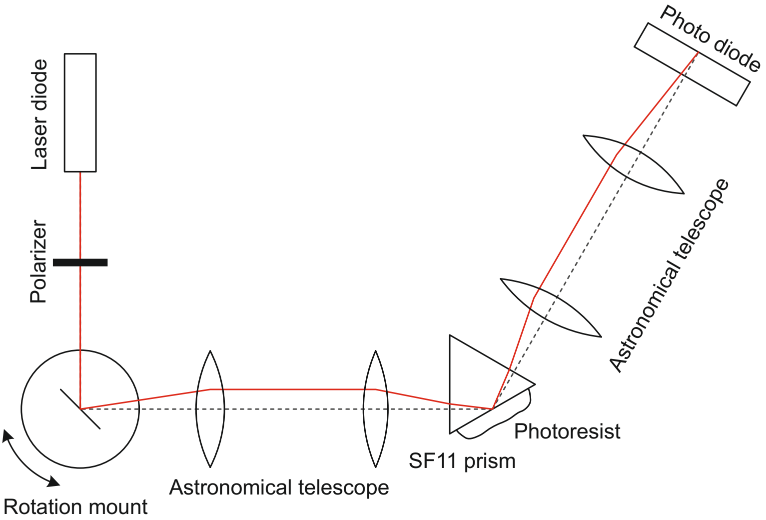

Figure A.1. Setup for measuring the critical angle of the total internal reflection. The refractive index values are obtained by measuring the critical angle of different photoresists at different wavelengths.

The critical angle of total internal reflection is measured in the setup depicted in Fig. A.1. Linear polarized light of a laser diode is led through an astronomical telescope on the back of a prism. The angle of the incident beam onto the back of the prism is controlled by a rotation mount. The astronomical telescope ensures that there is nearly no beam walk on the back of the prism. The reflection is guided through another astronomical telescope on a photo diode.

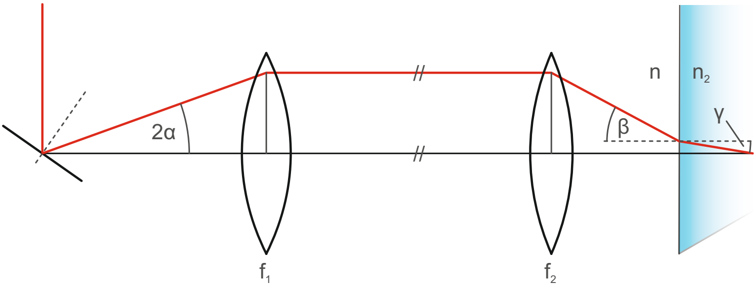

Figure A.2. Dependency of the angles in the setup for the refractive index measurement.

Using trigonometric functions and Snell's law the angle γ (see Fig. A.2 for the definition) can be calculated from the rotation angle α of the rotation mount by

$$\begin{aligned}\gamma(\alpha) &= \arcsin\left(\frac{n}{n_2}\sin\left(\arctan\left(\frac{f_1}{f_2}\tan(2\alpha)\right)\right)\right) \\ &\approx \frac{n}{n_2}\frac{f_1}{f_2}2\alpha, \qquad \text{for small rotation angles } \alpha,\end{aligned} \tag{A.1}$$

where n is the refractive index of the surrounding medium (air) and n_2 is the refractive index of the prism material. The astronomical telescope consists of two lenses with focal lengths of $f_1 = 10\,\text{cm}$ and $f_2 = 6\,\text{cm}$. The distance between the two lenses is equal to the the sum of the two focal lengths $(f_1 + f_2)$.

As a 60° SF-11 prism is used the incident angle on the back of the prism can be calculated as

$$\theta(\alpha) = 60^\circ + \gamma(\alpha). \tag{A.2}$$

The critical angle θ_c is given by

$$\theta_c = \arcsin\left(\frac{n_2}{n_1}\right), \tag{A.3}$$

where n_1 and n_2 are the refractive indices of the two materials. For total internal reflection it is $n_1 > n_2$. Light, which hits the interface under an angle θ larger than the critical angle θ_c is completely internally reflected.

A highly refractive prism is needed in order to get total internal reflection. We use a SF11 prism. By changing the angle θ of the incident beam the critical angle can be accurately determined. The critical angle is measured for different photoresists at different wavelength in order to calculate Chauchy's dispersion curves.

For each wavelength we determine the point of the critical angle of the prism/photoresist interface as well as for a prism/BK7 glass transition in order to calibrate the scale of the incident angle. For this purpose, the lower part of the prism is coated with photoresist and subsequently, exposed by UV-light for 5 min (Dymax BlueWave 50), on the upper part we mount a BK7 glass plate with immersion oil beneath.

As only a thin oil layer beneath the BK7 glass plate is used we neglect the influence of the immersion medium in the calculation of critical angle. However, for a more precise evaluation the multi-layer system has to be considered. As immersion oil we use Zeiss Immersol 518 F with a refractive index of $n_{\mathrm{Oil}} = 1.518$ (23 °C).

It is our present experience that the refractive index is strongly dependent on the exposure dose this means exposure time and intensity. Additionally, there is a time-dependent behavior of the refractive index directly after the exposure process, which reaches a plateau after a few hours. The exposure mode (UV exposure process or direct laser writing) influences the refractive index of the exposed photoresist, as well. These issues should be considered in a more precise evaluation, too.

Figure A.3 shows the measurement for Ormocomp and BK7 glass at a wavelength of 650 nm. We fit the functional relation of reflectance obtained by Fresnel's equations to the measurement data in order to determine the critical angle. The value of the crit-

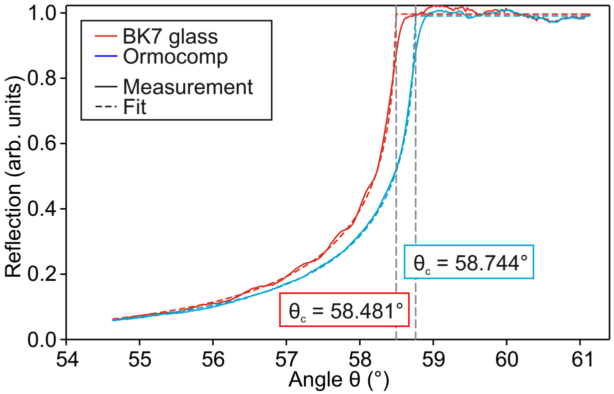

Figure A.3. Measurement of the critical angle of the total internal reflection for OrmoComp and BK7 glass at a wavelength of 650 nm. The refractive index values are obtained from the critical angles using Equation (A.3).

ical angle of BK7 is used in order to calibrate the angle scale. The red curves represent the measurement of the BK7 glass, where the critical angle of θ_c is calculated by the literature values of 1.7766 and 1.5145 at a wavelength of 650 nm for SF11 and BK7, respectively (Schott optical glass data sheet). The axis is accordingly adjusted with respect to the calculated value. Therefore, the critical angle of the photoresist can be accurately determined. The reflection curves are in good agreement with the theoretically expected reflectance behavior (Fresnel's equation) of the transition from a high to a low refractive index material.

Table A.1 shows the measured refractive indices of the photoresists IP-S (Nanoscribe), Ormocomp (micro resist), and IP-Dip (Nanoscribe). The refractive index value of 1.513, which we use for the simulations fits to the measured values.

Figure A.4 shows the measurement results. In addition, we plotted two refractive index values of Ormocomp given by the datasheet of the manufacturer in the figure. Measurements with a historic Pulfrich refractometer confirm the measured refractive index values of IP-S (Nanoscribe) at different wavelength.

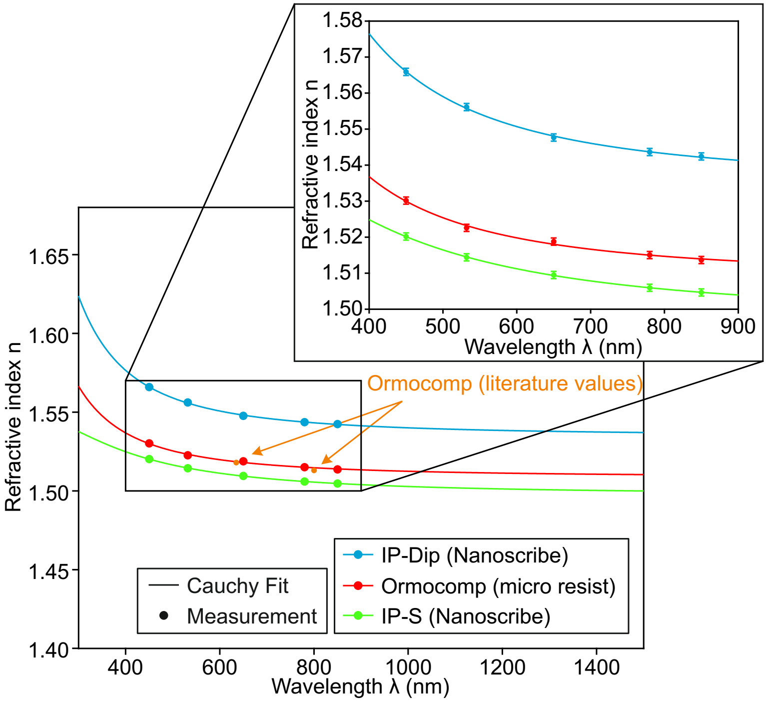

Figure A.4. Dispersion measurement of the photoresists Nanoscribe IP-Dip, Nanoscribe IP-S, and micro resist Ormocomp. The refractive index values are obtained by measuring the critical angle of the total internal reflection at different wavelengths. Subsequently, the refractive index characteristics is fitted by using Cauchy's equations.

Refractive indexes	IP-S	Ormocomp	IP-Dip
$n_{450\,\mathrm{nm}}$	1.5202	1.5302	1.5659
$n_{532\,\mathrm{nm}}$	1.5144	1.5226	1.5561
$n_{650\,\mathrm{nm}}$	1.5095	1.5188	1.5477
$n_{780\,\mathrm{nm}}$	1.5059	1.5150	1.5436
$n_{850\,\mathrm{nm}}$	1.5046	1.5137	1.5424

Table A.1. Refractive index measurement of the photoresists IP-Dip, IP-S, and Ormocomp. The refractive index values are obtained by measuring the critical angle of the total internal reflection for the used photoresists at different wavelengths.

We fit Cauchy's equation to the measured values. The relationship between refractive index and wavelength is give by

$$n(\lambda) = A + \frac{B}{\lambda^2} + \frac{C}{\lambda^4} \qquad \lambda \text{ in } \mu\mathrm{m}. \tag{A.4}$$

The fit parameters A, B, and C are summarized in Table A.2. Cauchy's equation well describes the measured values of the refractive indices.

Cauchy parameters	A	B	C
IP-S	1.4976	$5.3347 \cdot 10^{-3}$	$-1.5572 \cdot 10^{-4}$
Ormocomp	1.5087	$3.5891 \cdot 10^{-3}$	$1.4516 \cdot 10^{-4}$
IP-Dip	1.5348	$4.9664 \cdot 10^{-3}$	$2.7342 \cdot 10^{-4}$

Table A.2. Cauchy parameters of the photoresists IP-Dip, IP-S, and Ormocomp. The values are obtained by fitting the Cauchy's equation (A.4) to the refractive index measurements.

We use Cauchy's equation to calculate the Abbe number, which is a characteristic number for the dispersion of materials in optics. The Abbe number is defined as

$$\nu_d = \frac{n_d - 1}{n_F - n_C}, \tag{A.5}$$

where n_d, n_F, and n_C are the refractive indices of the material at Fraunhofer lines d, F, and C. The Fraunhofer lines are asso-

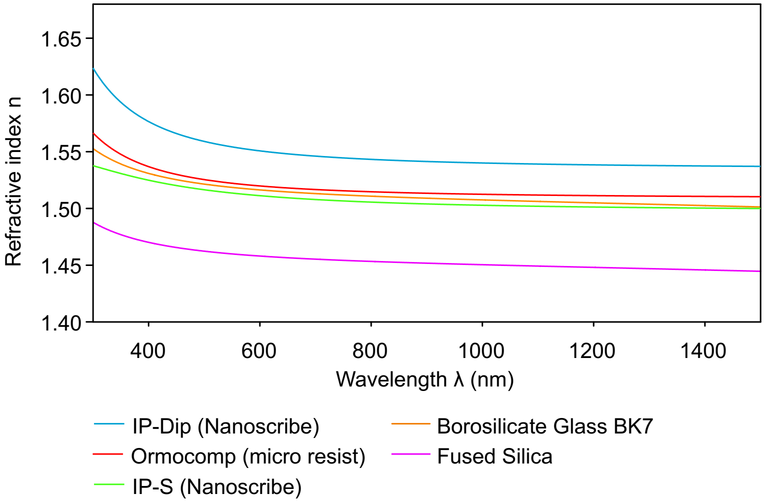

Figure A.5. Refractive index of the used photoresists in comparison with other optical materials.

ciated with the absorption lines in the spectrum of the sun. d corresponds to a wavelength of 587.6 nm, F corresponds to a wavelength of 486.1 nm, and C corresponds to a wavelength of 656.3 nm.

The Abbe number of Nanoscribe IP-S is $\nu_d = 62.09$ and thus behaves like crown glasses, which are typical glasses used in lenses and other optical components. $\nu_d = 59.99$ is the Abbe number of micro resist Ormocomp, which is as well in the region of the crown glasses. Glasses which corresponds to the dispersion of IP-S and Ormocomp are for example K7 and N-K5.

As the refractive indices of Nanoscribe IP-Dip are above the ones of IP-S and Ormocomp the Abbe number of IP-Dip is $\nu_d = 42.71$. Corresponding glasses are very light flint glasses. A typical glass which exhibits the same Abbe number just as IP-Dip is LLF1.

Figure A.5 shows the functional dependence for Cauchy's equation for the measured photoresists in comparison to other optical materials. The curve shapes are in good agreement with the curve shapes of other optical materials.

B

RESOLUTION TARGETS

We use different test patterns in order to determine the optical performance of our imaging optics. The 1951 USAF resolution test chart shown in Fig. B.1 is used to measure the resolving power at different distances. All patterns in this chapter are printed in real size.

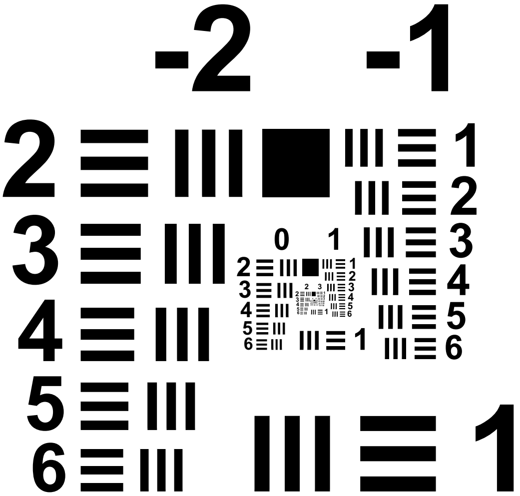

Figure B.1. 1951 USAF resolution test chart in real size. Resolution test pattern standardized by the US Air Force. Each group consists of six elements.

The scales and dimensions of the bars are given in Table B.1 and B.2. Additionally, the resolution in lines per millimeter can be calculated by

$$\text{Resolution (lp/mm)} = 2^{\left[\text{group} + \frac{(\text{element}-1)}{6}\right]} \text{lp/mm}. \qquad (\text{B.1})$$

	Group							
	0	**1**	**2**	**3**	**4**	**5**	**6**	**7**
1	1.00	2.00	4.00	8.00	16.00	32.00	64.00	128.00
2	1.12	2.24	4.49	8.98	17.96	35.90	71.80	143.70
3	1.26	2.52	5.04	10.08	20.16	40.30	80.60	161.30
4	1.41	2.83	5.66	11.31	22.63	45.30	90.50	181.00
5	1.59	3.17	6.35	12.70	25.40	50.80	101.60	203.20
6	1.78	3.56	7.13	14.25	28.51	57.00	114.00	228.10

Table B.1. Number of line pairs per millimeter in 1951 USAF resolving power test target.

	Group							
	0	**1**	**2**	**3**	**4**	**5**	**6**	**7**
1	500.00	250.00	125.00	62.50	31.25	15.63	7.81	3.91
2	445.45	222.72	111.36	55.68	27.84	13.92	6.96	3.48
3	396.85	198.43	99.21	49.61	24.80	12.40	6.20	3.10
4	353.55	176.78	88.39	44.19	22.10	11.05	5.52	2.76
5	314.98	157.49	78.75	39.37	19.69	9.84	4.92	2.46
6	280.62	140.31	70.15	35.08	17.54	8.77	4.38	2.19

Table B.2. Width of 1 line in micrometers in 1951 USAF resolving power test target.

Figure B.2 shows a test pattern for the evaluation of contrast, distortion, and field of view. The test pattern consists of a grid and concentric rings, which correspond to azimuthal angles of 10° field of view. It is designed for a distance of 5.0 mm.

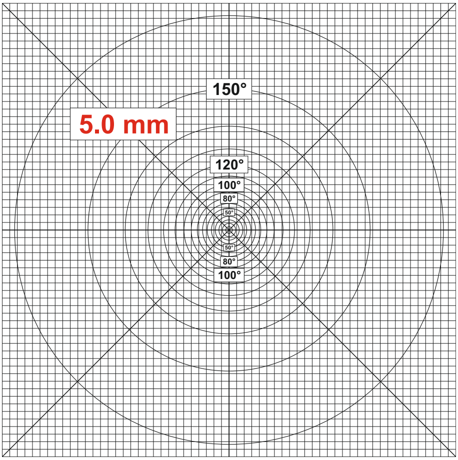

Figure B.2. Test pattern for the measurement of the field of view as well as the detection of distortions. It is designed for a distance of 5 mm between observation plane and target.

In Fig. B.3 the Telefunken FuBK test card is shown. It is used for the evaluation of image quality and color fidelity.

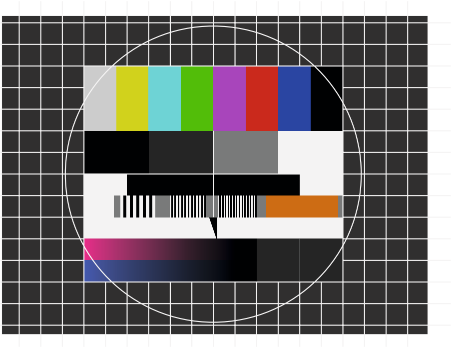

Figure B.3. Telefunken FuBK test card. It allows for the adjustment of color, brightness, and contrast.

C

SINGLE MODE FIBER SM 780HP

For comparison, we measured the beam propagation after a pure single mode fiber SM 780HP. The fiber is used as substrate for refractive and diffractive beam shaping elements presented in Chapter 4 and 6.

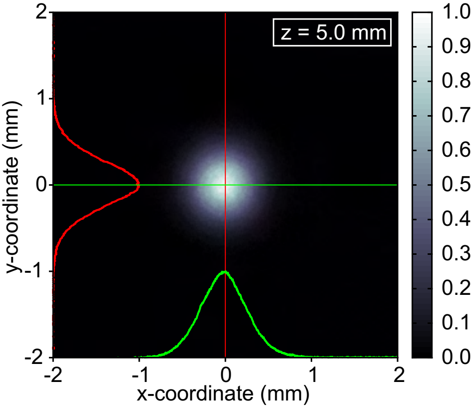

Figure C.1. Intensity profile of a single mode fiber SM 780HP at a distance of 5 mm. The mode image is obtained by taking a picture with a CCD camera at a distance of 5 mm behind the fiber end facet. Additionally, the cross sections in x- and y-direction are plotted.

Figure C.1 shows the measured intensity distribution emerging from an optical single mode fiber SM 780HP (Thorlabs). The mode image is obtained by taking a picture at a distance of 5 mm behind the fiber end facet. In addition, we plotted the cross section in x- and y-direction. The beam profile can be nicely described by a Gaussian curve.

We determine a beam width (radius of intensity at $1/e^2$) at a distance of 5 mm of $w = 0.54$ mm, which corresponds to a numerical aperture of NA = 0.1073. Gaussian beam propagation shows that the beam divergence is given by

$$\theta_{\text{div}} = \arctan\left(\frac{\lambda}{\pi w_0}\right), \tag{C.1}$$

where λ is the wavelength and w_0 is the beam waist. The beam waist of the single mode optical fiber is 2.45 µm, which is obtained by mode theory with refractive indices of 1.4598 and 1.4537 for core and cladding material, respectively [71]. For the mode theory calculation a core diameter of the optical fiber of 4.4 µm is used. The wavelength is 808 nm.

A divergence angle of $\theta_{\text{div}} = 5.99°$ is obtained. This corresponds to a numerical aperture of 0.1044 at a wavelength of 808 nm, which is in good agreement with the measurements. Figure C.2 shows the measured and simulated beam profiles at different distances. The simulation data are obtained by using the Huygens-Fresnel diffraction approach introduced in Chapter 3.2. At each position the measured intensity distribution is determined by taking an image with a CCD camera. The normalized intensity profile is calculated by taking the average of the cross section in x- and y-direction. At propagation distances of 2 mm, 6 mm, and 10 mm behind the end facet of the optical fiber the intensity profiles are compared to the simulations in detail. The positions are labeled with A, B, and C. Measurement and simulation are in good agreement.

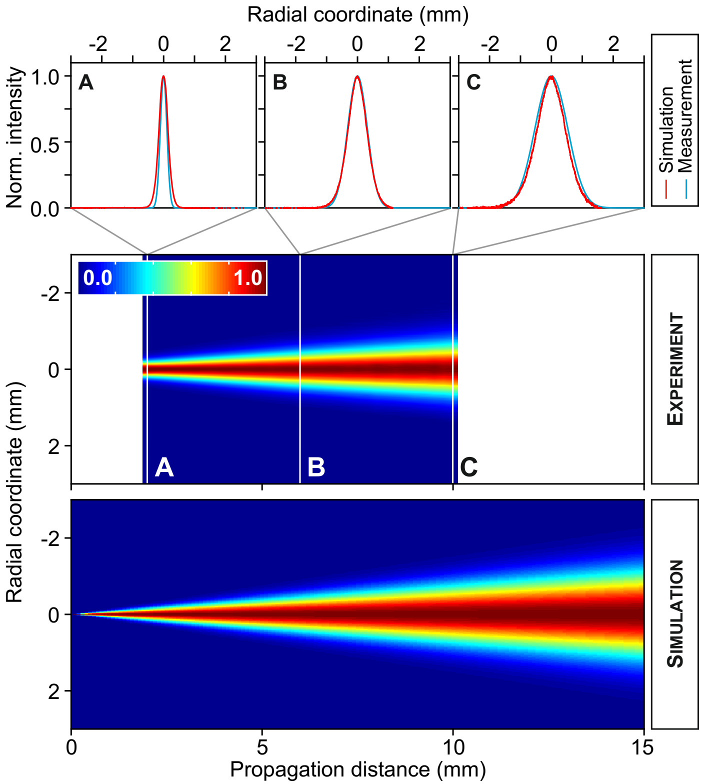

Figure C.2. Measurement of the intensity distribution at different distances behind the fiber end for a pure single mode fiber SM 780HP. At each distance pictures of the mode are taken using a CCD camera. The cross section is obtained by taking the average of the cross section in x- and y-direction. At several positions the measurement is compared to the simulation. In red the measurements are plotted, the blue lines corresponds to the simulations. The positions 2 mm, 6 mm, and 10 mm are labeled with A, B, and C.

D

FABRICATION PARAMETERS

In this chapter we specify fabrication parameters used for different structures manufactured by a commercially available femtosecond laser lithography system from Nanoscribe GmbH (Photonic Professional GT, Nanoscribe GmbH, Germany). The given values are typical values, which could be adapted for other applications. The values can vary due to different laser alignment and different charge of photoresist.

In order to fabricate three-dimensional structures different configurations and fabrication methods can be used. These are explained in detail in Section 2.2.

In dip-in configuration the photoresist is directly placed onto the objective lens. In conventional configuration the photoresist is separated by a substrate or cover glass from the immersion oil. More details to the configurations and writing modes can be found in Chapter 2. In order to get structures with high resolution and excellent accuracy high numerical aperture objectives (high-NA objectives) are necessary. These objective need an immersion medium, which is in the case of dip-in laser lithography the photosensitive medium by itself, and in the case of conventional configuration an immersion oil.

We use a 100x NA1.3 and a 63x NA1.4 objective for direct laser writing. The 100x NA 1.3 objective is not recommended for galvo scan mode, as it is not designed for this application, which results in a very small writing area.

In dip-in configuration nearly every kind of substrate can be used. We successfully fabricated three-dimensional structures on the following substrates:

- CMOS sensors,
- Diamond substrates,
- Indium tin oxide (ITO) covered substrates,

- Light emitting diodes (LEDs),
- GaAs substrates,
- Gold covered substrates [58, 62],
- Glass substrates, and
- Optical fibers.

In conventional configuration it is recommended to use cover glasses as substrates, as immersion objective are usually corrected for 170 µm thick cover glasses. In addition, the working distance or the structure height is reduced by the glass thickness of the substrate.

The fabrication parameters are defined in the header of the job file. Important values are laser power (command: *LaserPower*) and writing speed (commands: *ScanSpeed* or *UpdateRate* and *PointDistance*).

The laser power is given in % between 1 and 100 %. For the maximum laser power (100 %) the lithography system is calibrated in the way that 50 mW enter the aperture of the standard objective (63x NA1.4), which has a diameter of 7.3 mm. In order to use higher laser powers there is the possibility to increase the *PowerScaling* value. The default value is 1. The *PowerScaling* value is dependent on the power, which the laser can deliver and can be seen in the AOM calibration curve, when die laser power is calibrated.

In order to expose photoresists a certain dose is necessary. Among the laser power the time, for which the laser stays at the same position plays a significant role. This time is defined either by the exposure time or the speed, with which the laser is moved through the photoresist.

For the piezo scan mode the parameter *UpdateRate* and *PointDistance* define the speed. In order to expose the photoresist homogenous along a given trajectory, the line segment between two programmed points is automatically interpolated. The interpolated points are sent to the piezo actuators at a specific update rate. These points have a distance, which is defined by the command *PointDistance*. Therefore, the writing speed is given by

UpdateRate × *PointDistance*.
For the galvo scan mode the writing speed can be directly defined in µm/s by the command: *ScanSpeed*.
For the piezo scan mode, speeds between 25 and 300 µm/s are typical, for the galvo scan mode speeds between 1000 and 20 000 µm/s are useful.

In order to write three-dimensional structures a solid object has to be converted into lines or trajectories, along which the structure is exposed. For this purpose, slicing and hatching distances define layer-by-layer fabricated structures. Fig. D.1 depicts the definition of slicing distance, hatching distance and hatching angle. Slicing distance is the distance between two neighboring layers. For our refractive optical elements we choose a fixed layer-by-layer distance in order to create a homogenous refractive index over the whole structure. The diffractive optical elements are fabricated with different slicing distances in order to reach the desired surface profile. The hatching distance is the distance between two neighboring lines/trajectories in one layer. The hatching angle is the angle between the hatching direction of two neighboring layers. Usually, we choose a value of ±30° for our optical lenses.

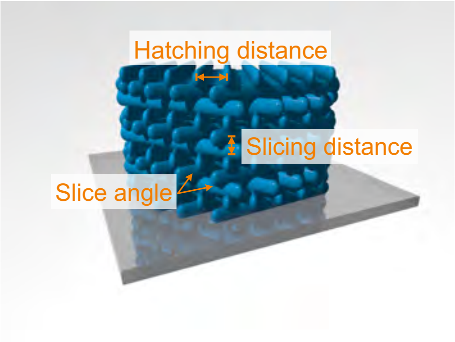

Figure D.1. Schematic illustration of the slicing parameters.

The conversion of solid objects into lines is not limited to the here presented possibility. As shown in Section 8.4 there is the possibility to write solid models in shells and scaffolds in order to safe fabrication time.

In the following we specify typical parameters used for the fabrication of one- to three-dimensional structures by femtosecond direct laser writing.

Parameters	
Configuration	Dip-in configuration
Writing Mode	Piezo scan mode
Objective	100x NA 1.3
Substrate	Glass substrate, optical fiber
Photoresist	Ormocomp
Base	
Laser power	56 %
Point distance	100 nm
Update rate	1000 /s
Slice parameter	Slicing distance: 0.80 µm Hatching distance: 0.35 µm
Refractive surface	
Laser power	26.5 %
Point distance	100 nm
Update rate	1000 /s
Slice parameter	Slicing distance: 0.2 µm Hatching distance: 0.2 µm

Table D.1. Parameters for the fabrication of refractive lenses in piezo writing mode with Ormocomp.

Parameters	
Configuration	Dip-in configuration
Writing Mode	Galvo scan mode
Objective	63x NA 1.4
Substrate	Glass substrate, optical fiber
Photoresist	OrmoComp
Base	
Laser power	100 %
Scan speed	10 000 µm/s
Slice parameter	Slicing distance: 0.40 µm Hatching distance: 0.25 µm
Refractive surface	
Laser power	75 %
Scan speed	25 000 µm/s
Slice parameter	Slicing distance: 0.10 µm Hatching distance: 0.15 µm

Table D.2. Parameters for the fabrication of refractive lenses in galvo scan mode with Ormocomp.

Parameters	
Configuration	Dip-in configuration
Writing Mode	Galvo scan mode
Objective	63x NA 1.4
Substrate	Cover glass (170 µm), diamond substrate, GaAs substrate, optical fiber
Photoresist	IP-S
Laser power	42.5 %
Scan speed	25 000 µm/s
Slice parameter	Slicing distance: 0.1 µm Hatching distance: 0.15 µm

Table D.3. Parameters for the fabrication of refractive lenses in galvo scan mode with IP-S.

Parameters	
Configuration	Dip-in configuration
Writing Mode	Galvo scan mode
Objective	63x NA 1.4
Substrate	Cover glass (170 µm)
Photoresist	IP-S
Laser power	34.5 %
Scan speed	25 000 µm/s
Slice parameter	Slicing distance: 0.1 µm Hatching distance: 0.15 µm

Table D.4. Parameters for the fabrication of refractive lenses on CMOS sensors in galvo scan mode with IP-S.

Parameters	
Configuration	Dip-in configuration
Writing Mode	Galvo scan mode
Objective	63x NA 1.4
Substrate	Glass/CaF substrate + 5 nm Cr or Pt + 50 nm to 100 nm Au
Photoresist	IP-Dip
Laser power	10.5 - 14.5 %
Scan speed	12 000 µm/s

Table D.5. Parameters for the fabrication of nanoantenna array on 100 nm gold covered substrate in galvo scan mode with IP-Dip.

Parameters	
Configuration	Dip-in configuration
Writing Mode	Galvo scan mode
Objective	63x NA 1.4
Substrate	DiLL substrate, optical fiber
Photoresist	IP-Dip
Laser power	21 %
Scan speed	15 000 µm/s
Slice parameter	Slicing distance: 50 nm Hatching distance: 85 - 90 nm

Table D.6. Parameters for the fabrication of diffractive elements on optical fibers in galvo scan mode with IP-Dip.

Parameters	
Configuration	Dip-in configuration
Writing Mode	Galvo scan mode
Objective	63x NA 1.4
Substrate	DiLL substrate, optical fiber
Photoresist	IP-Dip
Laser power	27.5 %
Scan speed	10 000 µm/s
Structure parameter	see Chapter 5

Table D.7. Parameters for the fabrication of photonic crystals in galvo scan mode with IP-Dip.

Parameters	
Configuration	Dip-in configuration
Writing Mode	Galvo scan mode
Objective	63x NA 1.4
Substrate	DiLL substrate
Photoresist	IP-Dip
Laser power	25 %
Scan speed	15 000 µm/s
Slice parameter	Slicing distance: 0.4 µm Hatching distance: 0.25 µm

Table D.8. Parameters for the fabrication of phase masks in galvo scan mode with IP-Dip.

E

IMAGES

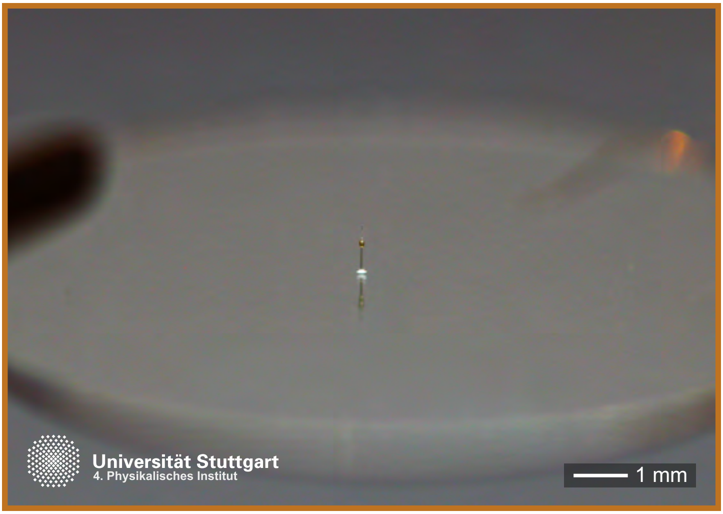

Figure E.1. Image of the TV-Tower of Stuttgart with a height of 1 mm.

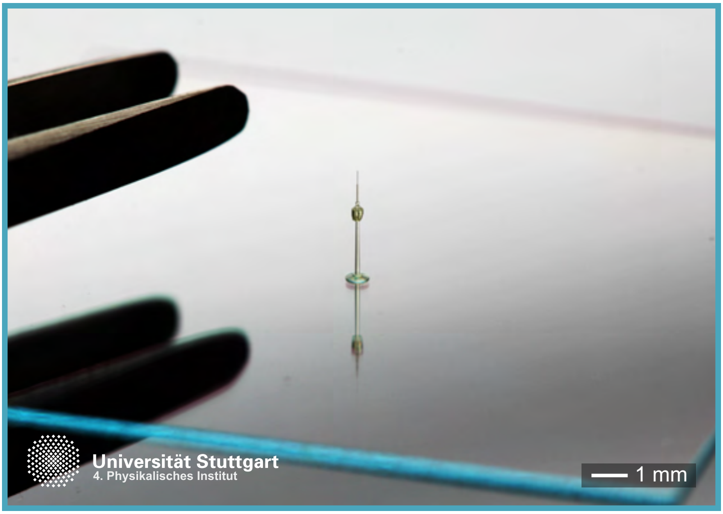

Figure E.2. Image of the TV-Tower of Stuttgart with a height of 3 mm.

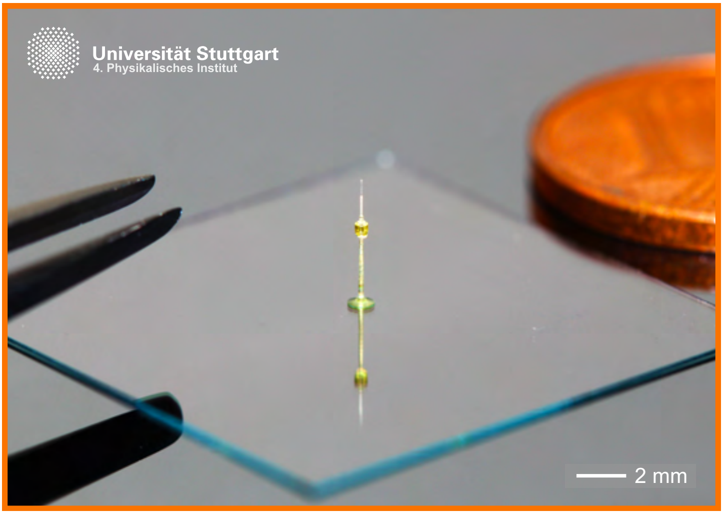

Figure E.3. Image of the TV-Tower of Stuttgart with a height of 5 mm.

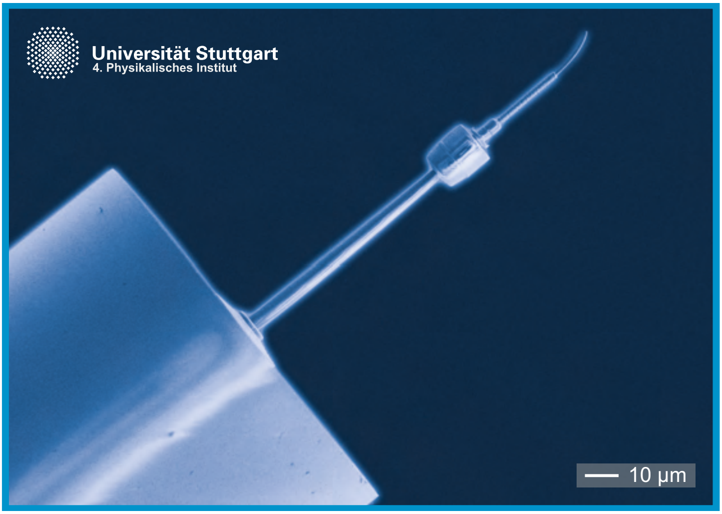

Figure E.4. Colored SEM-image of the TV-Tower of Stuttgart.

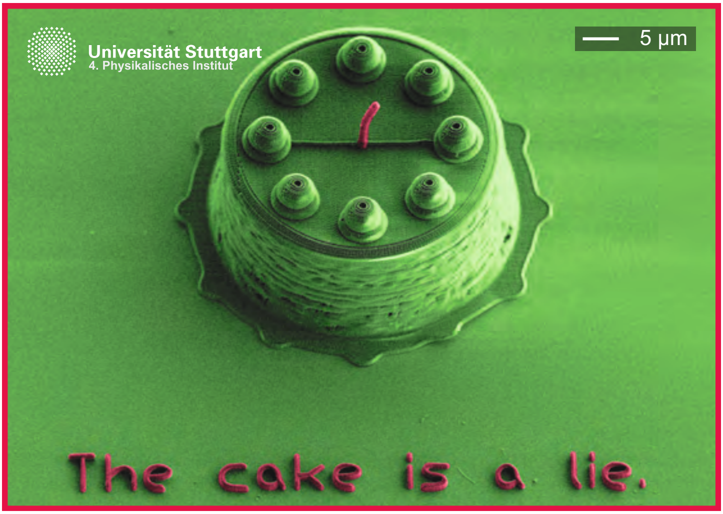

Figure E.5. The cake is a lie.

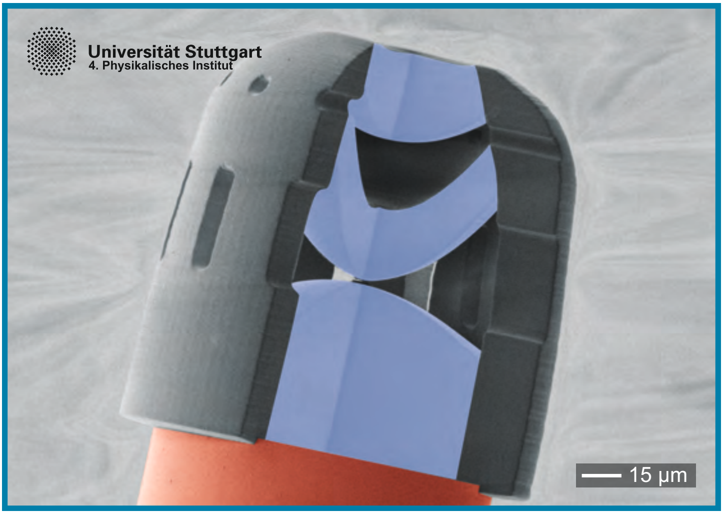

Figure E.6. Colored SEM-image of a miniature triplet lens directly fabricated on an optical fiber.

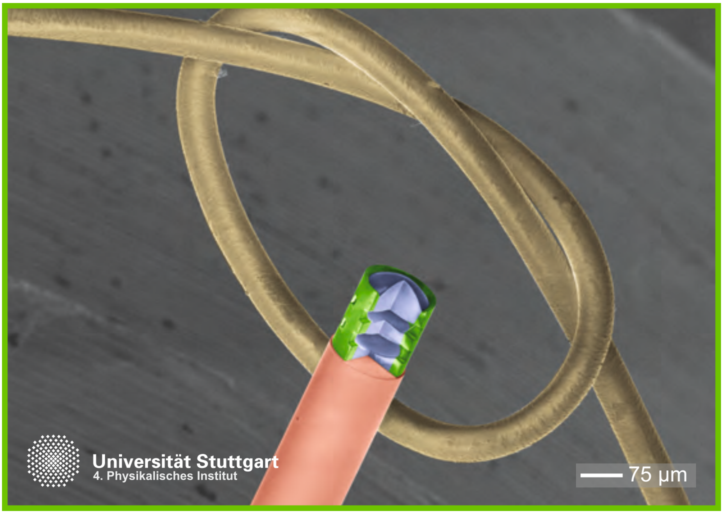

Figure E.7. Colored SEM-image of a miniaturized triplet lens compared to a hair.

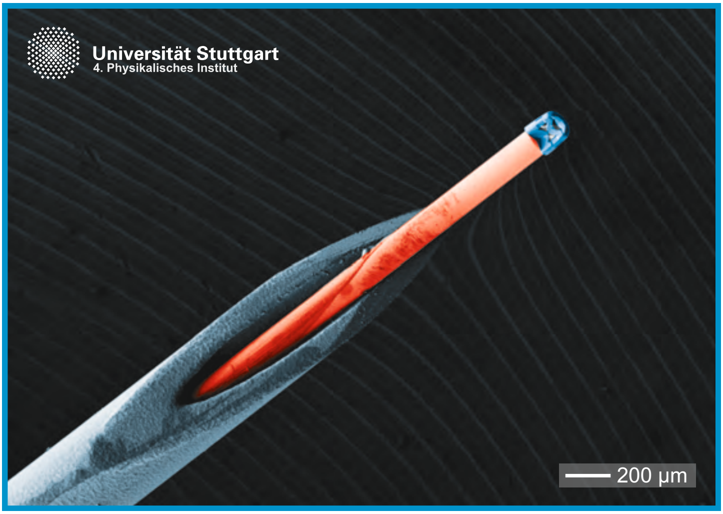

Figure E.8. Colored SEM-image of a miniaturized triplet lens coming out of a cannula.

Figure E.9. Colored SEM-image of a submicrometer triplet lens next to a fly.

Figure E.10. Colored SEM-image of a miniaturized Zeiss Hologon objective.

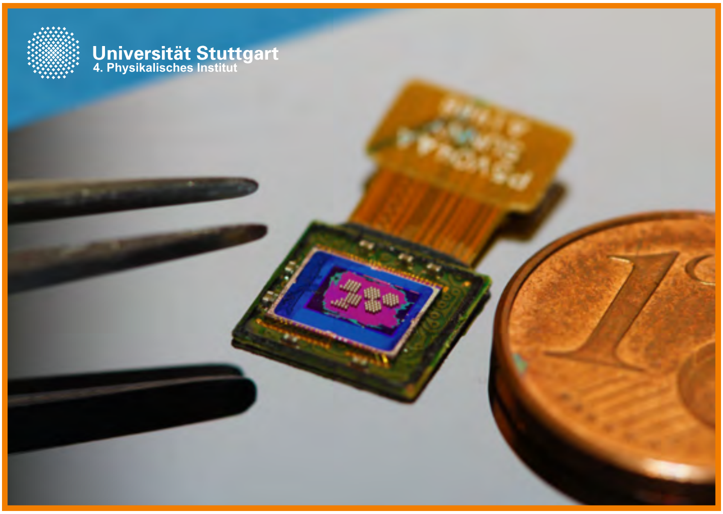

Figure E.11. Regular arrangement of doublet lenses directly fabricated on a CMOS image sensor.

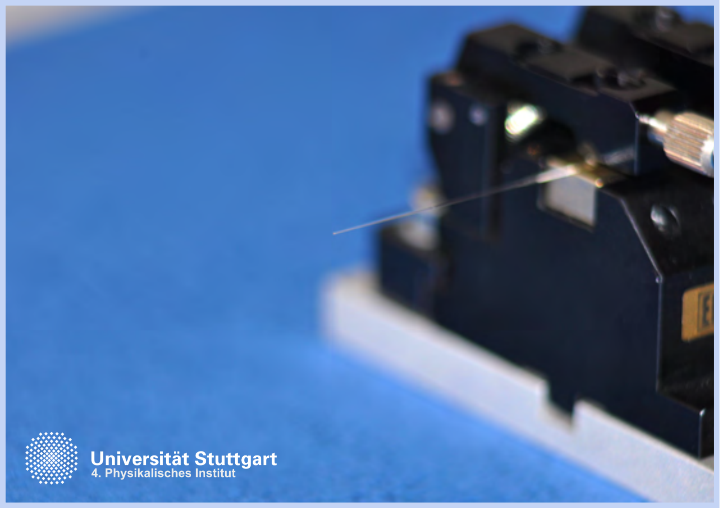

Figure E.12. Photography of miniature optics attached to a single mode optical fiber.

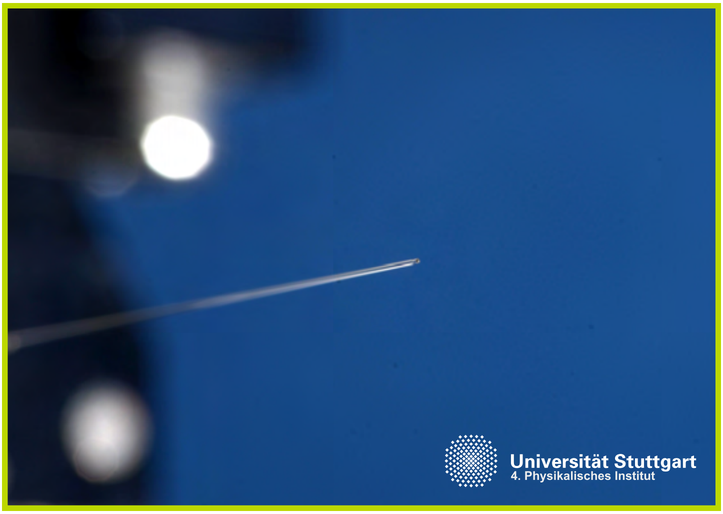

Figure E.13. Photography of miniaturized optics attached to a single mode optical fiber.

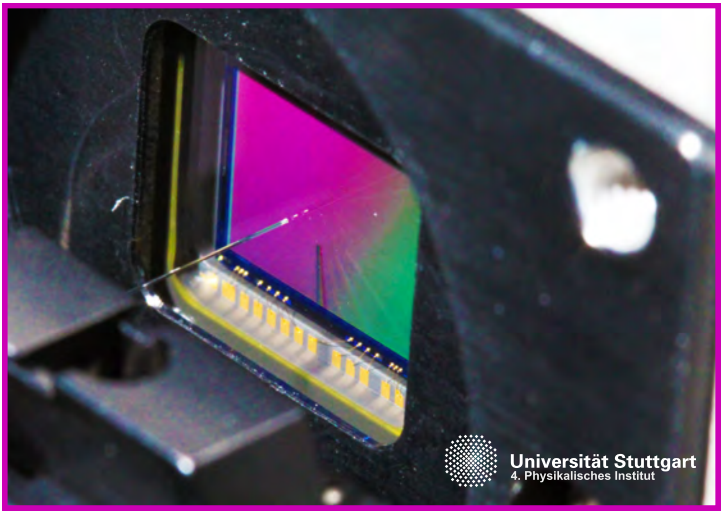

Figure E.14. Photography of micro-optical element attached to a single mode optical fiber.

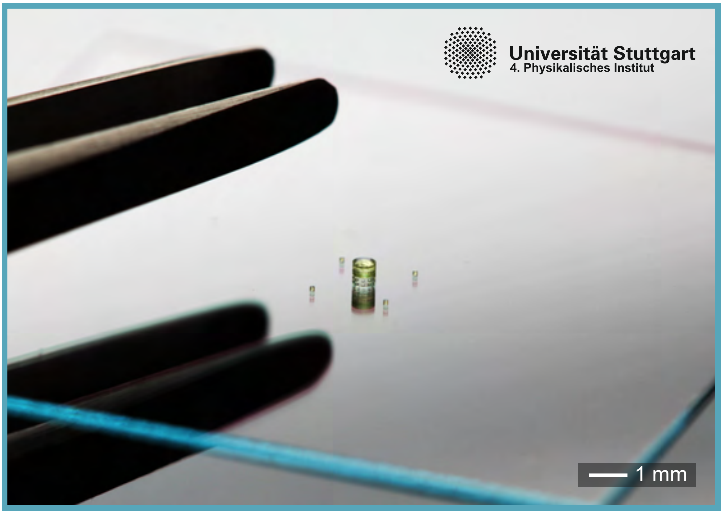

Figure E.15. Image of a multi-lens system with a diameter of 600 µm.

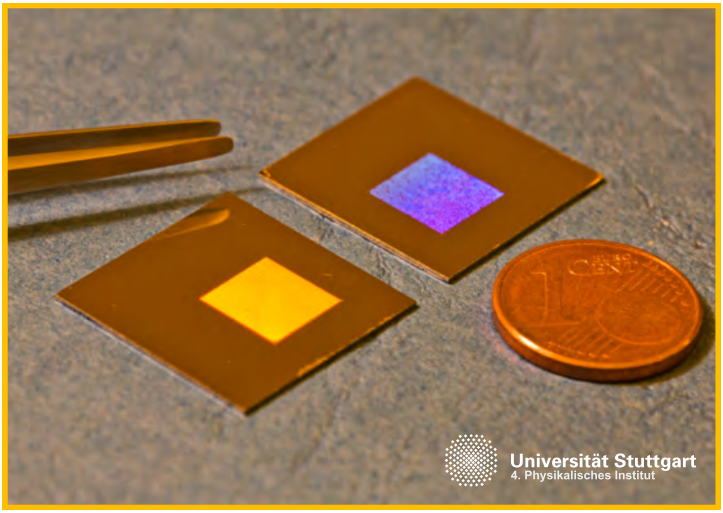

Figure E.16. Photography of samples covered with plasmonic nanoantennas over a large area.

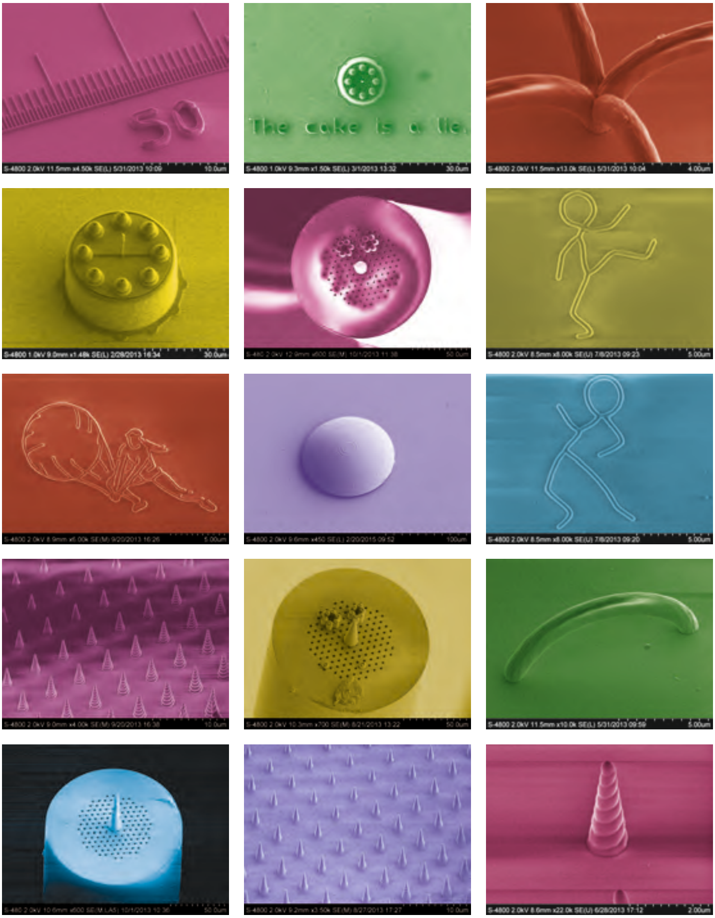

Figure E.17. Various colored SEM images.

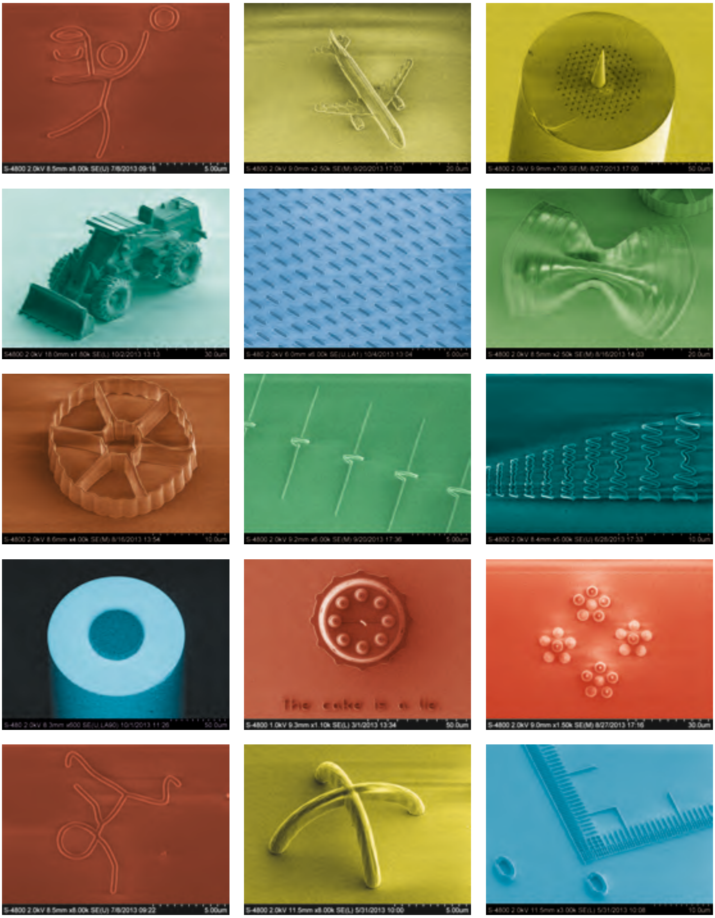

Figure E.18. Various colored SEM images.

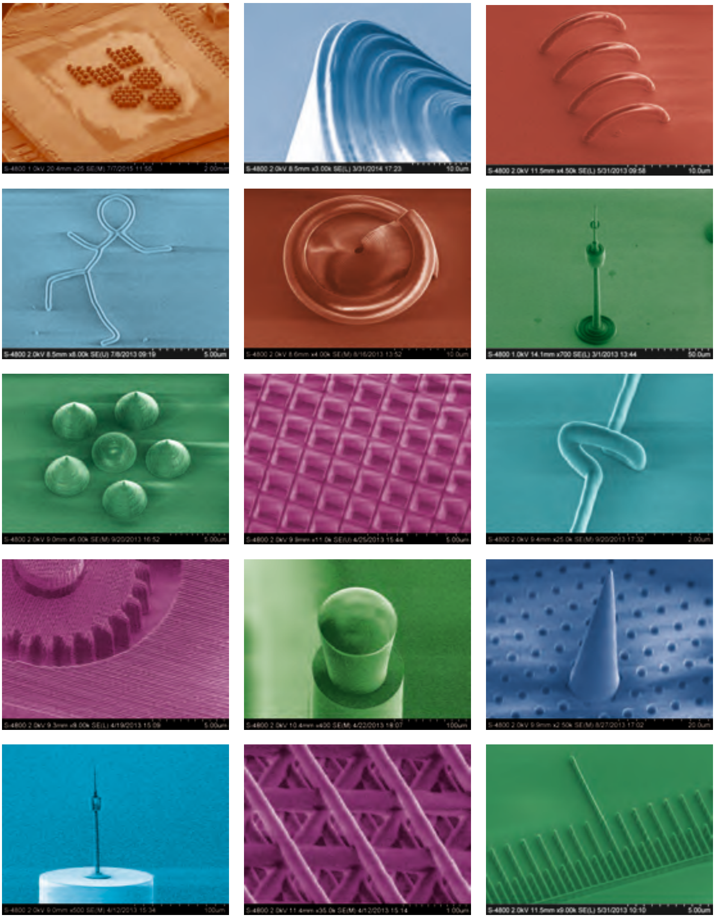

Figure E.19. Various colored SEM images.

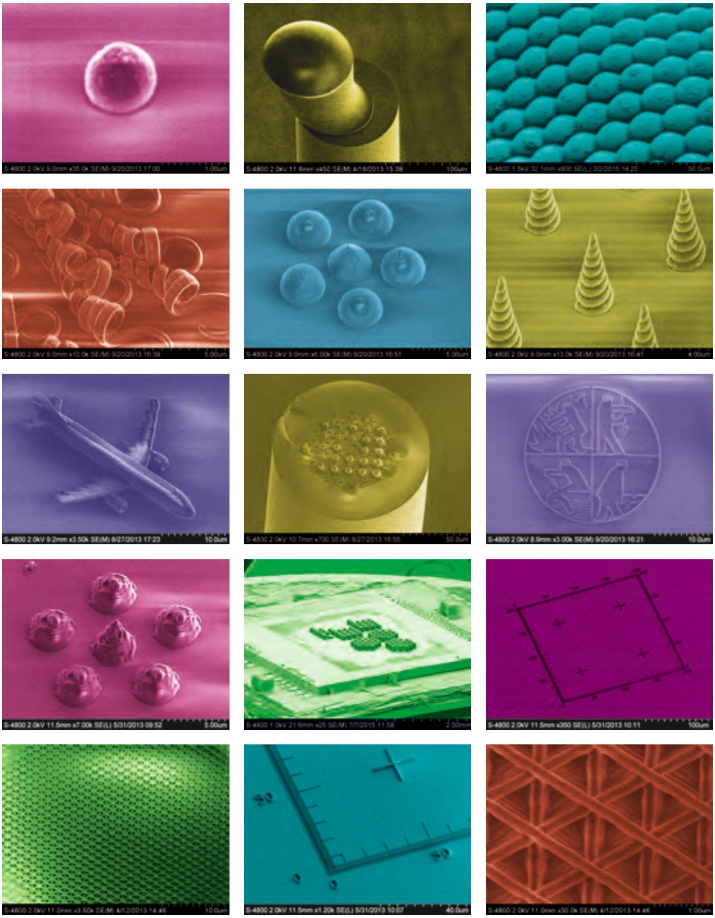

Figure E.20. Various colored SEM images.

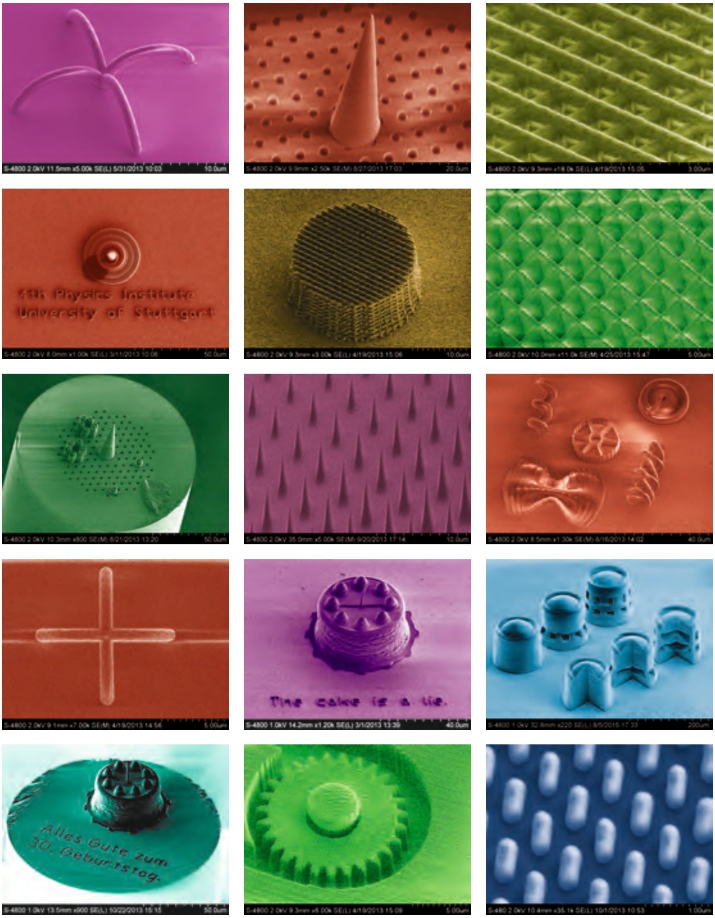

Figure E.21. Various colored SEM images.

Figure E.22. Various colored SEM images.

BIBLIOGRAPHY

BIBLIOGRAPHY

[1] Mohammad Vaezi, Hermann Seitz, and Shoufeng Yang. A review on 3D micro-additive manufacturing technologies. *The International Journal of Advanced Manufacturing Technology*, 67(5-8):1721–1754, 2013.

[2] Brian H. Cumpston, Sundaravel P. Ananthavel, Stephen Barlow, Daniel L. Dyer, Jeffrey E. Ehrlich, Lael L. Erskine, Ahmed A. Heikal, Stephen M. Kuebler, I.-Y. Sandy Lee, Dianne McCord-Maughon, Jinqui Qin, Harald Rockel, Mariacristina Rumi, Xiang-Li Wu, Seth R. Marder, and Joseph W. Perry. Two-photon polymerization initiators for three-dimensional optical data storage and microfabrication. *Nature*, 398(6722):51–54, 1999.

[3] J. Serbin, A. Egbert, A. Ostendorf, Boris N. Chichkov, R. Houbertz, G. Domann, J. Schulz, C. Cronauer, L. Fröhlich, and M. Popall. Femtosecond laser-induced two-photon polymerization of inorganic organic hybrid materials for applications in photonics. *Optics Letters*, 28(5):301, 2003.

[4] Markus Deubel, Georg von Freymann, Martin Wegener, Suresh Pereira, Kurt Busch, and Costas M. Soukoulis. Direct laser writing of three-dimensional photonic-crystal templates for telecommunications. *Nature Materials*, 3(7):444–447, 2004.

[5] Maria Farsari and Boris N. Chichkov. Materials processing: Two-photon fabrication. *Nature Photonics*, 3(8):450–452, 2009.

[6] Mangirdas Malinauskas, Holger Gilbergs, Albertas Žukauskas, Vytautas Purlys, Domas Paipulas, and Roaldas Gadonas. A femtosecond laser-induced two-photon photopolymerization technique for structuring microlenses. *Journal of Optics*, 12(3):035204, 2010.

[7] Mangirdas Malinauskas, Albertas Žukauskas, Vytautas Purlys, Kastytis Belazaras, Andrej Momot, Domas Paipulas, Roaldas Gadonas, Algis Piskarskas, Holger Gilbergs, Arune Gaidukevičiute, Ioanna Sakellari, Maria Farsari, and Saulius Juodkazis. Femtosecond laser polymerization of hybrid/integrated micro-optical elements and their characterization. *Journal of Optics*, 12(12):124010, 2010.

[8] Henry E. Williams, Daniel J. Freppon, Stephen M. Kuebler, Raymond C. Rumpf, and Marco A. Melino. Fabrication of three-dimensional micro-photonic structures on the tip of optical fibers using SU-8. *Optics Express*, 19(23):22910–22922, 2011.

[9] Mangirdas Malinauskas, Maria Farsari, Algis Piskarskas, and Saulis Juodkazis. Ultrafast laser nanostructuring of photopolymers: A decade of advances. *Physics Reports*, 533(1):1–31, 2013.

[10] Zoran D. Popovic, Robert A. Sprague, and G. A. Neville Connell. Technique for monolithic fabrication of microlens arrays. *Applied Optics*, 27(7):1281, 1988.

[11] Sung-Keun Lee, Kwang-Cheol Lee, and Seung S. Lee. A simple method for microlens fabrication by the modified LIGA process. *Journal of Micromechanics and Microengineering*, 12(3):321, 2002.

[12] B.-K Lee, D. S. Kim, and T. H. Kwon. Replication of microlens arrays by injection molding. *Microsystem Technologies*, 10(6-7):531–535, 2004.

[13] Joo Yeon Kim, Nils B. Brauer, Vahid Fakhfouri, Dmitri L. Boiko, Edoardo Charbon, Gabi Grutzner, and Juergen Brugger. Hybrid polymer microlens arrays with high numerical apertures fabricated using simple ink-jet printing technique. *Optical Materials Express*, 1(2):259, jun 2011.

[14] Reinhard Völkel, Martin Eisner, and Kenneth J. Weible. Miniaturized imaging systems. *Microelectronic Engineering*, 67-68:461–472, 2003.

[15] Dengfeng Kuang, Xiaoliang Zhang, Min Gui, and Zhiliang Fang. Hexagonal microlens array fabricated by direct laser writing and inductively coupled plasma etching on organic light emitting devices to enhance the outcoupling efficiency. *Applied Optics*, 48(5):974–978, 2009.

[16] Ren Yang, Wanjun Wang, and Steven A. Soper. Out-of-plane microlens array fabricated using ultraviolet lithography. *Applied Physics Letters*, 86(16):1–3, 2005.

[17] Reinhard Völkel, Jacques Duparre, Frank Wippermann, Peter Dannberg, Andreas Bräuer, Ralph Zoberbier, Markus Gabriel, Michael Hornung, Sven Hansen, and Ralf Suess. Technology Trends of Microlens Imprint Lithography and Wafer Level Cameras (WL). In *MOC'08, Conference on Micro-Optics, Brussels, Belgium*, pages 25–28, 2008.

[18] Saskia Biehl, Rolf Danzebrink, Peter Oliveira, and Michael A. Aegerter. Refractive Microlens Fabrication by Ink-Jet Process. *Journal of Sol-Gel Science and Technology*, 13(1/3):177–182, 1998.

[19] Andreas Brückner, Alexander Oberdörster, Jens Dunkel, Andreas Reimann, Martin Müller, and Frank Wippermann. Ultra-thin wafer-level camera with 720p resolution using micro-optics. In *Proceeding of SPIE: Novel Optical Systems Design and Optimization XVII*, page 91930W, 2014.

[20] Hongtao Han, Moshe Kriman, and Mark Boomgarden. Wafer Level Camera technology - From wafer level packaging to wafer level integration. In *1th International Conference on Electronic Packaging Technology and High Density Packaging*, 2010.

[21] F. Schiappelli, R. Kumar, M. Prasciolu, D. Cojoc, S. Cabrini, M. De Vittorio, G. Visimberga, A. Gerardino, V. Degiorgio, and E. Di Fabrizio. Efficient fiber-to-waveguide coupling by a lens on the end of the optical fiber fabricated by focused ion beam milling. *Microelectronic Engineering*, 73-74:397–404, 2004.

[22] S. Cabrini, C. Liberale, D. Cojoc, A. Carpentiero, M. Prasciolu, S. Mora, V. Degiorgio, F. De Angelis, and E. Di Fabrizio. Axicon lens on optical fiber forming optical tweezers, made by focused ion beam milling. *Microelectronic Engineering*, 83(4-9):804–807, 2006.

[23] Jasbinder Sanghera, Catalin Florea, Lynda Busse, Brandon Shaw, Fritz Miklos, and Ishwar Aggarwal. Reduced Fresnel losses in chalcogenide fibers by using anti-reflective surface structures on fiber end faces. *Optics Express*, 18(25):26760–26768, 2010.

[24] Xuan Yang, Nazar Ileri, Cindy C. Larson, Thomas C. Carlson, Jerald A. Britten, Allan S. P. Chang, Claire Gu, and Tiziana C. Bond. Nanopillar array on a fiber facet for highly sensitive surface-enhanced Raman scattering. *Optics Express*, 20(22):24819–24826, 2012.

[25] S. Choi, K. R. Kim, K. Oh, C. M. Chun, M. J. Kim, S. J. Yoo, and D. Y. Kim. Interferometric inscription of surface relief gratings on optical fiber using azo polymer film. *Applied Physics Letters*, 83(6):1080, 2003.

[26] Gorgi Kostovski, Udayakumar Chinnasamy, Sasani Jayawardhana, Paul R. Stoddart, and Arnan Mitchell. Sub-15nm optical fiber nanoimprint lithography: A parallel, self-aligned and portable approach. *Advanced Materials*, 23(4):531–535, 2011.

[27] Yoshiaki Kanamori, Masaaki Okochi, and Kazuhiro Hane. Fabrication of antireflection subwavelength gratings at the tips of optical fibers using UV nanoimprint lithography. *Optics Express*, 21(1):322–328, 2013.

[28] Eric G. Johnson, Jared Stack, Thomas J. Suleski, Charles Koehler, and William Delaney. Fabrication of micro optics on coreless fiber segments. *Applied Optics*, 42(5):785, 2003.

[29] Thierry Grosjean, Said Sadat Saleh, Miguel Angel Suarez, Idriss Abdoulkader Ibrahim, Vincent Piquerey, Daniel Charraut, and Patrick Sandoz. Fiber microaxicons fabricated by

a polishing technique for the generation of Bessel-like beams. *Applied Optics*, 46(33):8061, 2007.

[30] Renaud Bachelot, Carole Ecoffet, Denis Deloeil, Pascal Royer, and Daniel-Joseph Lougnot. Integration of Micrometer-Sized Polymer Elements at the End of Optical Fibers by Free-Radical Photopolymerization. *Applied Optics*, 40(32):5860, 2001.

[31] Sándor Valkai, László Oroszi, and Pál Ormos. Optical tweezers with tips grown at the end of fibers by photopolymerization. *Applied Optics*, 48(15):2880, 2009.

[32] Kyung Rok Kim, Selee Chang, and K. Oh. Refractive microlens on fiber using UV-curable fluorinated acrylate polymer by surface-tension. *IEEE Photonics Technology Letters*, 15(8):1100–1102, 2003.

[33] J. Kim, M. Han, S. Chang, Jhang W. Lee, and K. Oh. Achievement of large spot size and long collimation length using UV curable self-assembled polymer lens on a beam expanding core-less silica fiber. *IEEE Photonics Technology Letters*, 16(11):2499–2501, 2004.

[34] V. J. Cadarso, J. Perera-Núñez, L. Jacot-Descombes, K. Pfeiffer, U. Ostrzinski, A. Voigt, A. Llobera, G. Grützer, and J. Brugger. Microlenses with defined contour shapes, 2011.

[35] So Eun Kim, Bok Hyeon Kim, Chung Ghiu Lee, Sejin Lee, Kyunghwan Oh, and Chul-Sik Kee. Elliptical defected core photonic crystal fiber with high birefringence and negative flattened dispersion. *Optics Express*, 20(2):1385–91, 2012.

[36] H. M. Presby, A. F. Benner, and C. A. Edwards. Laser micromachining of efficient fiber microlenses. *Applied optics*, 29(18):2692–2695, 1990.

[37] M. Wakaki, Y. Komachi, and G. Kanai. Microlenses and Microlens Arrays Formed on a Glass Plate by Use of a CO(2) Laser. *Applied Optics*, 37(4):627–631, 1998.

[38] G. Cojoc, C. Liberale, P. Candeloro, F. Gentile, G. Das, F. De Angelis, and E. Di Fabrizio. Optical micro-structures fabricated on top of optical fibers by means of two-photon photopolymerization. *Microelectronic Engineering*, 87(5-8):876–879, 2010.

[39] Carlo Liberale, Gheorghe Cojoc, Patrizio Candeloro, Gobind Das, Francesco Gentile, Francesco De Angelis, and Enzo Di Fabrizio. Micro-Optics Fabrication on Top of Optical Fibers Using Two-Photon Lithography. *IEEE Photonics Technology Letters*, 22(7):474–476, apr 2010.

[40] M. Malinauskas, A. Žukauskas, V. Purlys, A. Gaidukevičiute, Z. Balevičius, A. Piskarskas, C. Fotakis, S. Pissadakis, D. Gray, R. Gadonas, M. Vamvakaki, and M. Farsari. 3D microoptical elements formed in a photostructurable germanium silicate by direct laser writing. *Optics and Lasers in Engineering*, 50(12):1785–1788, 2012.

[41] S. Bianchi, V. P. Rajamanickam, L. Ferrara, E. Di Fabrizio, C. Liberale, and R. Di Leonardo. Focusing and imaging with increased numerical apertures through multimode fibers with micro-fabricated optics. *Optics Letters*, 38(23):4935–4938, 2013.

[42] Maciej Kowalczyk, Jakub Haberko, and Piotr Wasylczyk. Microstructured gradient-index antireflective coating fabricated on a fiber tip with direct laser writing. *Optics Express*, 22(10):12545–12550, 2014.

[43] He Huang, Shijie Chen, Hongmei Zou, Qing Li, Jian Fu, Feng Lin, and X Wu. Fabrication of micro-axicons using direct-laser writing. *Optics Express*, 22(9):11035–42, 2014.

[44] Viktor Aleksandrovich Soifer. *Methods for Computer Design of Diffractive Optical Elements*. John Wiley & Sons Ltd., 2002.

[45] Joachim Fischer and Martin Wegener. Three-dimensional optical laser lithography beyond the diffraction limit. *Laser & Photonics Reviews*, 7(1):22–44, 2013.

[46] Zongsong Gan, Yaoyu Cao, Richard a Evans, and Min Gu. Three-dimensional deep sub-diffraction optical beam lithography with 9 nm feature size. *Nature Communications*, 4:2061, jun 2013.

[47] J. Fischer, J. B. Mueller, A. S. Quick, J. Kaschke, C. Barner-Kowollik, and M. Wegener. Exploring the Mechanisms in STED-Enhanced Direct Laser Writing. *Adv. Optical Mater.*, 3(2):221–232, 2014.

[48] Y. R. Shen. *The Principles of Nonlinear Optics*. John Wiley & Sons Ltd., New York, 1984.

[49] E. Wolf. Electromagnetic Diffraction in Optical Systems. I. An Integral Representation of the Image Field. *Proceedings of the Royal Society A: Mathematical, Physical and Engineering Sciences*, 253(1274):349–357, dec 1959.

[50] B. Richards and E. Wolf. Electromagnetic Diffraction in Optical Systems. II. Structure of the Image Field in an Aplanatic System. *Proceedings of the Royal Society A: Mathematical, Physical and Engineering Sciences*, 253(1274):358–379, dec 1959.

[51] Markus Deubel. *Dreidimensionale Photonische Kristalle mittels Direktem Laserschreibens: Herstellung und Charakterisierung*. PhD thesis, Universität Karlsruhe, 2006.

[52] Franziska Klein, Benjamin Richter, Thomas Striebel, Clemens M. Franz, Georg Von Freymann, Martin Wegener, and Martin Bastmeyer. Two-Component Polymer Scaffolds for Controlled Three-Dimensional Cell Culture. *Advanced Materials*, 23(11):1341–1345, 2011.

[53] Andrea C. Scheiwe, Stephanie C. Frank, Tatjana J. Autenrieth, Martin Bastmeyer, and Martin Wegener. Subcellular stretch-induced cytoskeletal response of single fibroblasts within 3D designer scaffolds. *Biomaterials*, 44:186–194, 2015.

[54] Attilio Marino, Andrea Desii, Mario Pellegrino, Monica Pellegrini, Carlo Filippeschi, Barbara Mazzolai, Virgilio Mattoli,

and Gianni Ciofani. Nano-Structured Brownian Surfaces Prepared through Two-Photon Polymerization: Investigation of Stem Cell Response. *ACS Nano*, 8(11):11869–11882, 2014.

[55] Michael Thiel, Georg von Freymann, and Martin Wegener. Layer-by-layer three-dimensional chiral photonic crystals. *Optics Letters*, 32(17):2547, 2007.

[56] André Radke, Timo Gissibl, Thomas Klotzbücher, Paul V. Braun, and Harald Giessen. Three-Dimensional Bichiral Plasmonic Crystals Fabricated by Direct Laser Writing and Electroless Silver Plating. *Advanced Materials*, 23(27):3018–3021, 2011.

[57] Martin Schumann, Tiemo Bückmann, Nico Gruhler, Martin Wegener, and Wolfram Pernice. Hybrid 2D–3D optical devices for integrated optics by direct laser writing. *Light: Science & Applications*, 3(6):175, 2014.

[58] Shahin Bagheri, Ksenia Weber, Timo Gissibl, Thomas Weiss, Frank Neubrech, and Harald Giessen. Fabrication of Square-Centimeter Plasmonic Nanoantenna Arrays by Femtosecond Direct Laser Writing Lithography: Effects of Collective Excitations on SEIRA Enhancement. *ACS Photonics*, 2(6):779–786, 2015.

[59] Soichiro Tottori, Li Zhang, Famin Qiu, Krzysztof K. Krawczyk, Alfredo Franco-Obregón, and Bradley J. Nelson. Magnetic Helical Micromachines: Fabrication, Controlled Swimming, and Cargo Transport. *Advanced Materials*, 24(6):811–816, 2012.

[60] Dongchan Jang, Lucas R. Meza, Frank Greer, and Julia R. Greer. Fabrication and deformation of three-dimensional hollow ceramic nanostructures. *Nature Materials*, 12(10):893–898, 2013.

[61] Tiemo Bückmann, Michael Thiel, Muamer Kadic, R. Schittny, and Martin Wegener. An elasto-mechanical unfeelability cloak made of pentamode metamaterials. *Nature Communications*, 5:4130, 2014.

[62] Shahin Bagheri, Christine M. Zgrabik, Timo Gissibl, Andreas Tittl, Florian Sterl, Ramon Walter, Stefano De Zuani, Audrey Berrier, Thomas Stauden, Gunther Richter, Evelyn L. Hu, and Harald Giessen. Large-area fabrication of TiN nanoantenna arrays for refractory plasmonics in the mid-infrared by femtosecond direct laser writing and interference lithography. *Optical Materials Express*, 5(11):2625, 2015.

[63] Nanoscribe GmbH. Photonic Professional (GT) - User Manual. Technical report, Nanoscribe GmbH, Karlsruhe, Germany, 2015.

[64] Tiemo Bückmann, Nicolas Stenger, Muamer Kadic, Johannes Kaschke, Andreas Frölich, Tobias Kennerknecht, Christoph Eberl, Michael Thiel, and Martin Wegener. Tailored 3D mechanical metamaterials made by dip-in direct-laser-writing optical lithography. *Advanced Materials*, 24(20):2710–2714, 2012.

[65] Patrick Mueller, Michael Thiel, and Martin Wegener. 3D direct laser writing using a 405 nm diode laser. *Optics Letters*, 39(24):6847–50, 2014.

[66] Eugene Hecht. *Optik*. Oldenbourg Wissenschaftsverlag, Oldenbourg, 5th edition, 2009.

[67] Max Wolf and Emil Born. *Principle of Optics*. Pergamon Press, Oxford, 1970.

[68] John E. Greivenkamp. *Field Guide to Geometrical Optics*. SPIE Publications, 2004.

[69] Allan W. Snyder and John D. Love. *Optical Waveguide Theory*. Chapman and Hall Ltd., London, 1983.

[70] Ajoy Ghatak and K. Thyagarajan. *Introduction to fiber optics*. Cambridge University Press, Cambridge, 1998.

[71] John A. Buck. *Fundamentals of Optical Fibers*. John Wiley & Sons, Hoboken, New Jersey, 2nd edition, 2004.

[72] Dieter Meschede. *Optik, Licht und Laser*. Teubner Verlag, Wiesbaden, 2005.

[73] Joseph W. Goodman. *Introduction to Fourier Optics*. McGraw-Hill, Inc., New York, 1996.

[74] Wolfgang Singer, Michael Totzeck, and Herbert Gross. *Handbook of Optical Systems*, volume 2. Wiley-VCH, Weinheim, Germany, 2006.

[75] Hal G. Kraus. Huygens–Fresnel–Kirchhoff wave-front diffraction formulation: paraxial and exact Gaussian laser beams. *Journal of the Optical Society of America A*, 7(1):47, 1990.

[76] Simon Thiele, Andreas Seifert, and Alois M. Herkommer. Wave-optical design of a combined refractive-diffractive varifocal lens. *Optics Express*, 22(11):13343–13350, 2014.

[77] Michael Bass. *Handbook of Optics: Volume II - Design, Fabrication, and Testing; Sources and Detectors; Radiometry and Photometry*. McGraw Hill, third edit edition, 2010.

[78] Joseph M. Geary. *Introduction to Optical Testing*. SPIE - International Society for Optical Engine, Bellingham, Washington, 1993.

[79] Thomas J. Suleski and Donald C. O'Shea. Gray-scale masks for diffractive-optics fabrication: I Commercial slide imagers. *Applied Optics*, 34(32):7507, 1995.

[80] Chunlei Du, Xiaochun Dong, Chuankai Qiu, Qiling Deng, and Chongxi Zhou. Profile control technology for high-performance microlens array. *Optical Engineering*, 43(11):2595, 2004.

[81] Brian Morgan, C.M. Waits, John Krizmanic, and Reza Ghodssi. Development of a Deep Silicon Phase Fresnel Lens Using Gray-Scale Lithography and Deep Reactive Ion Etching. *Journal of Microelectromechanical Systems*, 13(1):113–120, feb 2004.

[82] Mizue Mizoshiri, Hiroaki Nishiyama, Junji Nishii, and Yoshinori Hirata. Three-dimensional SiO2 surface structures fabricated using femtosecond laser lithography. *Applied Physics A*, 98(1):171–177, 2010.

[83] Rebeca Martínez Vázquez, Shane M Eaton, Roberta Ramponi, Giulio Cerullo, and Roberto Osellame. Fabrication of binary Fresnel lenses in PMMA by femtosecond laser surface ablation. *Optics Express*, 19(12):11597–11604, 2011.

[84] Etienne Brasselet, Mangirdas Malinauskas, Albertas Žukauskas, and Saulius Juodkazis. Photopolymerized microscopic vortex beam generators: Precise delivery of optical orbital angular momentum. *Applied Physics Letters*, 97(21):2013–2016, 2010.

[85] S. Tibuleac, D. Wawro, and R. Magnusson. Resonant diffractive structures integrating waveguide-gratings on optical fiber endfaces. *1999 IEEE LEOS Annual Meeting Conference Proceedings. LEOS'99. 12th Annual Meeting. IEEE Lasers and Electro-Optics Society 1999 Annual Meeting (Cat. No.99CH37009)*, 2:99–100, 1999.

[86] Eric G Johnson, Jared Stack, Thomas J Suleski, Charles Koehler, and William Delaney. Fabrication of micro optics on coreless fiber segments. *Applied Opticsptics*, 42(5):785–791, 2003.

[87] M. Prasciolu, D. Cojoc, S. Cabrini, L. Businaro, P. Candeloro, M. Tormen, R. Kumar, C. Liberale, V. Degiorgio, A. Gerardino, G. Gigli, D. Pisignano, E. Di Fabrizio, and R. Cingolani. Design and fabrication of on-fiber diffractive elements for fiber-waveguide coupling by means of e-beam lithography. *Microelectronic Engineering*, 67-68:169–174, 2003.

[88] Jeffrey C. Lagarias, James A. Reeds, Margaret H. Wright, and Paul E. Wright. Convergence Properties of the Nelder–Mead Simplex Method in Low Dimensions. *SIAM Journal on Optimization*, 9(1):112–147, 1998.

[89] V. S. Pavelyev, S. V. Karpeev, A. V. Gavrilov, V. A. Soifer, A. N. Palagushkin, and S. A. Prokopenko. Design of on-fiber diffractive microrelief for efficient graded-index fiber mode excitation. *Optical Memory and Neural Networks*, 16(3):159–166, 2007.

[90] S. V. Karpeev, V. S. Pavelyev, S. N. Khonina, N. L. Kazanskiy, A. V. Gavrilov, and V. A. Eropolov. Fibre sensors based on transverse mode selection. *Journal of Modern Optics*, 54(6):833–844, 2007.

[91] A. V. Karsakov and S. N. Khonina. Investigation of focusing of the fundamental linearly polarized mode using microrelief on the end of an optical fiber. In *Optical Technologies for Telecommunications*, volume 9156, 2014.

[92] A. V. Gavrilov, V. S. Pavelyev, and V. A. Soifer. Integrated fiber pressure sensors based on transverse mode selective excitation. *Computer Optics*, 32(2):175–179, 2008.

[93] Francisco Javier Salgado-Remacha. Laguerre-Gaussian beam shaping by binary phase plates as illumination sources in micro-optics. *Applied Optics*, 53(29):6782–6788, 2014.

[94] Thomas F. Krauss and Richard M. De La Rue. Photonic crystals in the optical regime - past, present and future. *Progress in Quantum Electronics*, 23(2):51–96, 1999.

[95] Kevin A. Arpin, Agustin Mihi, Harley T. Johnson, Alfred J. Baca, John A. Rogers, Jennifer A. Lewis, and Paul V. Braun. Multidimensional architectures for functional optical devices. *Advanced Materials*, 22(10):1084–1101, 2010.

[96] Pierre Gilles de Gennes. *The Physics of Liquid Crystals*. Oxford University Press, Oxford, 1st editio edition, 1979.

[97] Rui Guo, Shizhou Xiao, Xiaomin Zhai, Jiawen Li, Andong Xia, and Wenhao Huang. Micro lens fabrication by means of femtosecond two photon photopolymerization. *Optics Express*, 14(2):810, 2006.

[98] Reinhard Völkel. Wafer-scale micro-optics fabrication. *Advanced Optical Technologies*, 1(3):135–150, 2012.

[99] Joo Yeon Kim, Karl Pfeiffer, Anja Voigt, Gabi Gruetzner, and Jürgen Brugger. Directly fabricated multi-scale microlens arrays on a hydrophobic flat surface by a simple ink-jet printing technique, 2012.

[100] Peter Dannberg, Frank Wippermann, Andreas Brückner, Andre Matthes, Peter Schreiber, and Andreas Bräuer. Wafer-Level Hybrid Integration of Complex Micro-Optical Modules. *Micromachines*, 5(2):325–340, 2014.

[101] Harald Ries and Julius Muschaweck. Tailored freeform optical surfaces. *Journal of the Optical Society of America. A, Optics, image science, and vision*, 19(3):590–5, 2002.

[102] X. Zhang, R. Wang, F. M. Cox, B. T. Kuhlmey, and M. C. J. Large. Selective coating of holes in microstructured optical fiber and its application to in-fiber absorptive polarizers. *Optics express*, 15(24):16270–8, 2007.

[103] Yi Ding, Xu Liu, Zhen-rong Zheng, and Pei-fu Gu. Freeform LED lens for uniform illumination. *Optics express*, 16(17):12958–66, 2008.

[104] Arnaud Dubois, Laurent Vabre, Albert-Claude Boccara, and Emmanuel Beaurepaire. High-Resolution Full-Field Optical Coherence Tomography with a Linnik Microscope. *Applied Optics*, 41(4):805, feb 2002.

[105] Jan Niehues, Peter Lehmann, and Weichang Xie. Low coherent Linnik interferometer optimized for use in Nano Measuring Machines. In *56th International Scientific Colloquium*, 2013.

[106] Optikos Corporation. How to Measure MTF and other Properties of Lenses. Technical report, Optikos Corporation, 1999.

[107] Magali Estribeau and Pierre Magnan. Fast MTF measurement of CMOS imagers using ISO 12233 slanted-edge

methodology. In Jean-Pierre Chatard and Peter N. J. Dennis, editors, *Proceedings of SPIE - Sensors, Systems, and Next Generation Satellites*, volume 5251, pages 243–252, feb 2004.

[108] Hubert H. Nasse. How to Read MTF Curves. Technical report, Carl Zeiss - Camera Lens Division, 2008.

[109] Fan Bu, Yuehong Qiu, and Xingtao Yan. Improvement of MTF measurement and analysis using knife-edge method. *Journal of Computational Information Systems*, 9(3):987–994, 2013.

[110] Jens Dunkel, Frank Wippermann, Andreas Brückner, Andreas Reimann, Martin Müller, and Andreas Bräuer. Fabrication of refractive freeform array masters for artificial compound eye cameras. In *Proc. SPIE: Micro-Optics*, volume 9130, page 91300P, 2014.

[111] D. Vandormael, S. Habraken, J. Loicq, C. Lenaerts, and D. Mawet. Antireflective subwavelength patterning of IR optics. In *Proceedings of SPIE*, volume 2, pages 63950L–7, sep 2006.

[112] T. Staudacher, F. Ziem, L. Häussler, R. Stöhr, S. Steinert, F. Reinhard, J. Scharpf, A. Denisenko, and J. Wrachtrup. Enhancing the spin properties of shallow implanted nitrogen vacancy centers in diamond by epitaxial overgrowth. *Applied Physics Letters*, 101(21):212401, 2012.

[113] S. Ali Momenzadeh, Rainer J. Stöhr, Felipe Favaro de Oliveira, Andreas Brunner, Andrej Denisenko, Sen Yang, Friedemann Reinhard, and Jörg Wrachtrup. Nano-engineered Diamond Waveguide as a Robust Bright Platform for Nanomagnetometry Using Shallow Nitrogen Vacancy Centers. *Nano Letters*, 15(1):165–169, aug 2014.

[114] M. Gschrey, A. Thoma, P. Schnauber, M. Seifried, R. Schmidt, B. Wohlfeil, L. Krüger, J.-H. Schulze, T. Heindel, S. Burger, F. Schmidt, A. Strittmatter, S. Rodt, and S. Reitzenstein. Highly indistinguishable photons from deterministic quantum-dot microlenses utilizing three-dimensional

in situ electron-beam lithography. *Nature communications*, 6(May):7662, 2015.

[115] Ann Katrin U. Michel, Dmitry N. Chigrin, Tobias W. W. Maß, Kathrin Schönauer, Martin Salinga, Matthias Wuttig, and Thomas Taubner. Using low-loss phase-change materials for mid-infrared antenna resonance tuning. *Nano Letters*, 13(8):3470–3475, 2013.

[116] Xinghui Yin, Martin Schäferling, Ann-Katrin U. Michel, Andreas Tittl, Matthias Wuttig, Thomas Taubner, and Harald Giessen. Active Chiral Plasmonics. *Nano Letters*, 15(7):4255–4260, jul 2015.

[117] Wei Zhang, Khaled Aljasem, Hans Zappe, and Andreas Seifert. Highly flexible MTF measurement system for tunable micro lenses. *Optics Express*, 18(12):12458, jun 2010.

[118] Armin Werber and Hans Zappe. Tunable microfluidic microlenses. *Applied Optics*, 44(16):3238, 2005.

[119] Christoph Friese, Armin Werber, Florian Krogmann, Wolfgang Mönch, and Hans Zappe. Materials, effects and components for tunable micro-optics. *IEEJ Transactions on Electrical and Electronic Engineering*, 2(3):232–248, may 2007.

[120] Chaolong Song, Nam-Trung Nguyen, Say-Hwa Tan, and Anand Krishna Asundi. Modelling and optimization of micro optofluidic lenses. *Lab on a Chip*, 9(9):1178, 2009.

ACKNOWLEDGMENTS

This thesis would not have been possible without the help of many people. Therefore, I am deeply grateful to those, who supported me during the last years. In particular, I want to thank

- Prof. Dr. Harald Giessen for giving me the opportunity to work in his group, for a lot of good advices, and for innumerable ideas.
- Prof. Dr. Christian Holm and Prof. Dr. Alois M. Herkommer for their support and for kindly agreeing to be my examination committee.
- Dr. Mario Hentschel for many essential advices, for his support and for all the fun we had.
- Martin Mesch for being a great office mate during the last years, for many useful discussions, for all the support in the mechanical workshop, and for all the fun we had.
- Dr. Bernd Metzger for all his support in optical issues and for the fun we had.
- Dr. Christine von Rekowski for the help in all administrative matters.
- Monika Ubl and Michael Kube for the support in the cleanroom and other technical issues.
- André Radke for introducing me to the world of direct laser writing and many useful advices.
- Nanoscribe GmbH, in particular Dr. Michael Thiel, Martin Hermatschweiler, Holger Fischer and his team for the support with the laser lithography system.
- Simon Thiele for his support in performing simulations.

- Ralf Kamella and his team from the mechanical workshop for their support in all kind of mechanical construction issues.
- ZygoLOT GmbH; Jan Niehues and Peter Lehmann from University of Kassel for white light interferometer measurements.
- Timo Mappes and his team from Carl Zeiss AG for the help with the lens characterization.
- Bettina Frank for performing atomic force microscope measurements.
- All current and former members of the 4th Phyiscs Institute for the pleasant working atmosphere. In particular, I want to thank Dr. Ralf Ameling, Dr. Daniel Dregely, Dr. Jessie Qin-Dregely, and Dr. Richard Taubert for the awesome time we had.
- My parents Ulrike and Werner Gissibl and my sisters Nadine and Julia for their constant help and support beyond my studies and research.
- My girlfriend Annabel for her kind support and with whom I could share the ups and downs of my PhD thesis.
- All my friends for their encouragement.

CURRICULUM VITAE

Personal Data

Timo Gissibl
Lichtensteiner Weg 3
71229 Leonberg

Phone: 07152 7645019
Mail: TGissibl@gmx.de

Date of birth: 09.08.1984
Place of birth: Stuttgart

Education

since 04.2010	PhD student in the group of Prof. Dr. Harald Giessen, University of Stuttgart
03.2010	Diploma in physics
2010	Diploma thesis "Femtosecond Two-Photon Structuring of Photonic Crystals and Photonic Crystal Fibers" at the 4th Physics Institute, University of Stuttgart Supervisor: Prof. Dr. Harald Giessen
2004 - 2010	Studies of Physics at the University of Stuttgart, Germany Specialized courses in optics, semiconductor quantum optics, and astrophysics. Subsidiary courses in biophysics, geophysics, and plasma physics.
2004	Abitur, Albert Schweitzer Gymnasium, Leonberg, Germany (German university entrance qualification)

Prices

- 1st place, Competition: Images of the nanoworld, 2013, Baden-Württemberg Stiftung.
- 1st place, Competition: 3D printed objects, 2015, Baden-Württemberg Stiftung.

Teaching

Summer term 2015	Advanced lab course "Mössbauer effect"
Summer term 2014	Advanced lab course "Mössbauer effect"
Summer term 2013	Advanced lab course "Mössbauer effect"
Winter term 2012/2013	Beginners lab course "Franck–Hertz experiment"
Summer term 2012	Advanced lab course "Mössbauer effect"
Winter term 2011/2012	Beginners lab course "Debye-Sears effect"
Summer term 2011	Advanced lab course "Mössbauer effect"
Winter term 2010/2011	Advanced lab course "Mössbauer effect"
Summer term 2010	Advanced lab course "Mössbauer effect"

COLOPHON

This document was typeset using the typographical look-and-feel `classicthesis` developed by André Miede. The style was inspired by Robert Bringhurst's seminal book on typography *"The Elements of Typographic Style"*. `classicthesis` is available for LaTeX via CTAN.